Magnetic Properties of FePt/MnO heterodimer nanoparticles

Masterarbeit

im

Studiengang

"Master of Science"

im Fach Physik

an der Falkultät für Physik und Astronomie

der Ruhr Universität Bochum

von

Xiao Sun

aus

Qingdao

Bochum, 2013

Superviser: PD Dr. rer. nat. Oleg Petracic
Ruhr Universität Bochum
Jülich Centre for Neutron Science JCNS and Peter Grünberg Institut PGI,
JARA-FIT, Forschungszentrum Jülich GmbH

Second referee: Prof. Dr. rer. nat. Ulrich Köhler
Ruhr Universität Bochum

This work was prepared at the Jülich Centre for Neutron Science JCNS and Peter Grünberg Institut PGI, JARA-FIT, Forschungszentrum Jülich GmbH, JCNS-2 (Prof. Th. Brückel).

Affirmation:

I certify that this work was completed entirely by myself. No other literature references and resources beside those cited have been used.

Acknowledgements

I am heartily thankful to Prof. Dr. Thomas Brückel and my supervisor, PD Dr. Oleg Petracic for providing me the opportunity to work on this thesis in the institute JCNS-2 at the Forschungszentrum Jülich. I am grateful for their guidance and advices during the work. I would especially like to thank Oleg Petracic for being my supervisor. This thesis would not have been done without his encouragement, patience and support from the beginning till the end.

I would like to express my sincere thanks to Prof. Dr. Ulrich Köhler, who agreed to be the second referee of my thesis. I would like to thank him for his excellent guidance and patience throughout my work as well as the years of the Master program.

It is my pleasure to thank Alice Klapper and other colleagues in the JCNS at Forschungszentrum Jülich for their support in developing an understanding of this project and the instruments.

I would like to thank Heiko Bauer and the colleagues of Universität Mainz for the beautiful nanoparticles. I would also like to thank Yixi Su, Kirill Nemkovski, Andrew Wildes for their help and support during the experiments.

Last but not least, I offer my regards and blessings to my parents and my friends, who have supported me in any respect during the completion of the project. I would like to thank them for their support, love and understanding.

Abstract

Magnetic nanoparticles have attracted much interest for decades. We have focused on antiferromagnetic MnO nanoparticles as well as the FePt@MnO heterodimer nanoparticles consisting of a ferromagnetic FePt particle in contact to an antiferromagnetic MnO particle. In the magnetometry measurements, both MnO and FePt@MnO nanoparticles show no feature at the N*é*el temperature of MnO at 120 K in the zero field coold (ZFC) magnetization curves. Instead, a broad peak at low temperatures in the ZFC magnetization curves can be observed. To investigate this unexpected behavior magnetometry and neutron scattering experiments have been performed. An exchange bias effect was not only observed in the FePt@MnO nanoparticles but also in single MnO nanoparticles. This hints also toward a ferromagnet-antiferromagnet coupling *inside* each MnO particle in addition to coupling between FePt and MnO particles. The antiferromagnetic order parameter of MnO was measured using polarized neutron scattering. It follows the expected behavior with the N*é*el temperature at approximately 120 K. This finding seems to be in contradiction to the magnetometry results but can be explained in terms of a core-shell spin-model of MnO nanoparticles.

Contents

1 Introduction

Nanoparticles are regarded as building blocks of new artificial materials. With control of the size and shape of the nanoparticles, materials with special properties can be produced. Magnetic nanoparticles are of interest in both science and technology for years. This is due to their potential applications in magnetic data storage and medicine. In fundamental research magnetic nanoparticles are ideal to study finite size and spin canting effects. Magnetic nanoparticles possess attractive properties significantly different from their bulk form. A heterodimer nanoparticle is a fascinating novel type of multifunctional nanomaterial. It is composed of two different nanoparticles in close contact together as a dimer. The FePt@MnO heterodimer nanoparticles from our collaborators of the University of Mainz are studied in this work. Due to the exchange bias effect on the interface between a ferromagnetic FePt nanoparticle and an antiferromagnetic MnO nanoparticle, the spins inside the ferromagnetic FePt nanoparticles can be magnetically stabilized by the antiferromagnetic MnO nanoparticles. This kind of exchange biased heterodimer nanoparticles can be useful in GMR- spin-valve devices.

MnO is a well-known antiferromagnet with a bulk N*é*el temperature of T_N = 120 K [1]. In nanometer size, MnO shows interesting magnetic properties. MnO nanoparticles have recently been successfully studied using polarized neutron diffraction with respect to their antiferromagnetic order [2, 3, 4]. A rounding of the magnetic phase transition in contrast to the first-order transition of bulk MnO has been observed [3, 4].

In this work, the magnetic structure of FePt@MnO nanoparticles and single MnO are measured with magnetometry. Neutron scattering experiments aiming to study the spin structure inside single MnO NPs and inside the MnO subunit of FePt@MnO heterodimer nanoparticles using polarized neutron have been performed. Hereby, the influence of the FePt nanoparticle on the spin structure of the MnO nanoparticles in the FePt@MnO heterodimer nanoparticles is studied. In order to explain the unusual magnetic behaviors of the MnO nanoparticles obtained in the experiments, Monte Carlo simulations of the spin structure in various sizes and shapes of MnO nanoparticles are compared to the experimental findings.

This thesis has the following structure: after this introduction and the theoretical background in section 2 the details of the experiments and the simulations are discussed in section 3 and 4, respectively. In section 5.1, the results obtained from magnetometry and neutron scattering are presented and section 5.2 discusses the

simulation results. In section 6, different models of the MnO nanoparticles are discussed according to the Monte Carlo simulations and the experimental results. Finally, section 7 provides an outlook.

2 Theoretical Background

2.1 Basics of Magnetism

The magnetic moment is the fundamental element of magnetism. In diamagnetic materials, a magnetic moment is induced antiparallel to the external field. Paramagnetic materials have intrinsic magnetic moments due to unpaired electrons. They are oriented randomly in the absence of an external field and are aligned by an applied field. Magnetic moments interact with each other as well as their environment and produce various interesting types of magnetic orders.

2.1.1 Ferromagnetism and Antiferromagnetism

Unlike the paramagnet a ferromagnet (FM) is characterized by spontaneous ordering between the moments even in the absence of an applied magnetic field. This is mostly due to the exchange interaction described by the Heisenberg Hamiltonian:

$$\hat{H} = -\sum J_{ij}\vec{S}_i \cdot \vec{S}_j \tag{2.1.1}$$

where J_{ij} are the exchange constants between two spins $\vec{S}_i$ and $\vec{S}_j$. The exchange interaction results in long range order. For a ferromagnet, the exchange constants are positive for the nearest neighbours, so that a parallel alignment of the moments is energetically favored. Conversely, the exchange constants for the nearest neighbours are negative in an antiferromagnet (AFM) with the result that an antiparallel ordering of the moments is energetically favored.

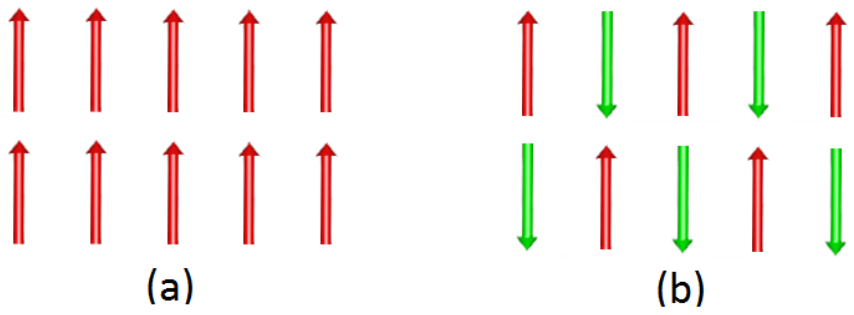

Figure 1: Magnetic spin ordering of (a) a ferromagnet and (b) an antiferromagnet.

A FM can be magnetized to a maximum value referred to as saturation magnetization M_s. At this point, all the magnetic moments lie parallel along a unique direction. As the applied field is removed, part of the magnetization remains, called remanent magnetization M_r. If the magnetic field is reduced to the coercive field

H_c opposite to the magnetization direction, the material can be demagnetized. This overall behavior of magnetization curve is known as hysteresis loop (Figure 2).

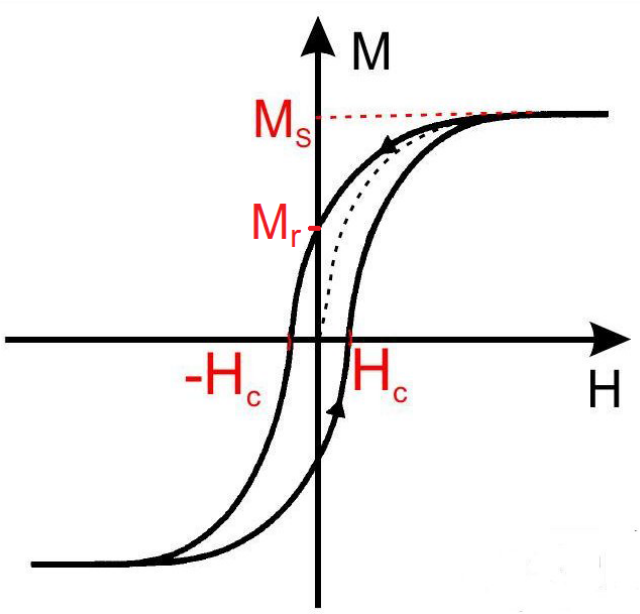

Figure 2: Hysteresis loop of a ferromagnet [5].

The spin structure of an AF can be thought of as composed by two sublattices, which have the identical size of magnetizations but opposite directions. The magnetizations of the both sublattices can be compensated, and result in zero total magnetization in case of zero applied field.

With increasing temperature thermal fluctations lead eventually to a phase transition at a critical temperature above which no long-range order exist. This transition temperature is called Curie temperature T_c for a FM, and N*é*el temperature T_N for an AF.

2.1.2 Anisotropy

Anisotropy means that the properties of a material are direction-dependent. Magnetic anisotropic materials have preferential directions to be magnetized, these directions are called easy axes. Without an external magnetic field, the magnetic moments of an anisotropic material tend to align along the easy axis. In isotropic materials, all directions are energetically equivalent. Non-spherical particles have one or more easy axes, the magnetization costs more energy in other directions than along the easy axes, this is known as shape anisotropy. Crystals possess easy axes due to their crystal structures. The spontaneous magnetizations are not equivalent in all directions. This effect is called magnetocrystalline anisotropy.

Magnetocrystalline anisotropy arises from the symmetry of the lattice, the shape of the electron orbitals and from spin-orbit coupling. In the reference frame of the electron, the nucleus orbits the electron and produces a current which induces an magnetic field. The magnetic field interacts with the spin of the electron and gives a term in the Hamiltonian:

$$H_{so} = -\frac{1}{2}\vec{m} \cdot \vec{B} = \frac{e\hbar^2}{2m_e c^2 r}\frac{dV(r)}{dr}\vec{S} \cdot \vec{L} \tag{2.1.2}$$

where $\hbar\vec{L} = m_e\vec{r} \times \vec{v}$ is the orbital angular momentum, $\vec{m} = (ge\hbar/2m)\vec{S}$ is the magnetic moment, and the factor $\frac{1}{2}$ is the relativistic Thomas factor.

An example for magnetocrystalline anisotropy is the uniaxial anisotropy, which has one single easy axis. The alignment of the magnetization along the two opposite directions of the easy axis cost the same amount of energy, which is the minimum of the anisotropy energy. As the magnetic moment turns perpendicular to the easy axis, it costs most energy. The anisotropy energy can be calculated according to the following equation:

$$E_A = K_1 V sin^2\theta + K_2 V sin^4\theta \tag{2.1.3}$$

where K_1 and K_2 are anisotropy constants, V is the volume, θ is the angle between the magnetization direction and the easy axis. Figure 3 shows the anisotropy energy dependent on the magnetization direction. As seen in figure 3, an energy barrier with magnitude of KV is found between two antiparallel states. The thermal energy has to be higher than ΔE to flip the spin.

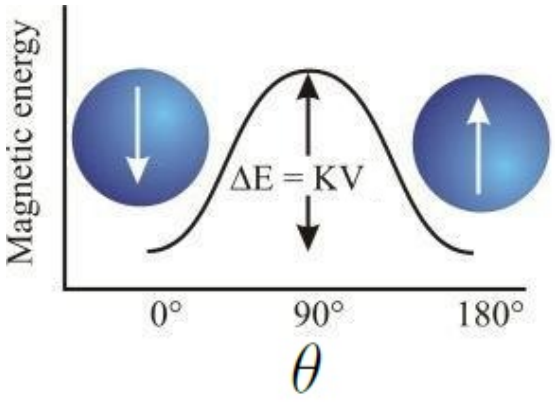

Figure 3: Energy barrier for switching the magnetization of a sample with volume V [6].

2.1.3 Magnetic Domains

Magnetic domains are regions with the same magnetic ordering in a magnetic material. They are separated by domain walls. Magnetic moments within one domain align themselves along the same direction, and produce a net magnetization. In different magnetic domains, net magnetizations can point into different directions.

A single domain structure, as shown in figure 4(a), creates a large magnetic field and possesses much dipolar energy. In order to reduce the magnetic field, it splits into two domains with opposite magnetization directions (figure 4(b)). One particle can split into more domains to reduce the dipolar energy further and closure domain structures can be formed to minimize the dipolar energy (figure 4(c)). Considering the energy costs by the formation of a domain walls, an equilibrium between the dipolar energy and the energy costs by domain walls is reached.

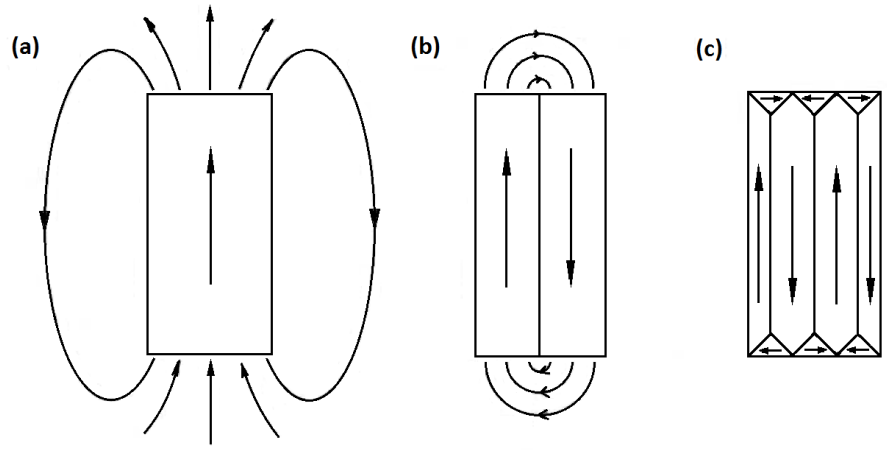

Figure 4: Different domain structures for ferromagnetic samples:(a) single domain state (b) two domains (c) closure domain states [7].

2.2 Basics of Nanomagnetism

Particles of 3 to 30 nm diameter are classified as nanoparticles. In nanoparticles, size-dependent properties can be observed, which are different from their bulk form. Bulk materials exhibit constant physical properties independent of the size. As the particle approaches nanometer size, unique magnetic properties can be obtained. As the size of the nanoparticles is reduced, the surface-to-volume ratio increases. Fundamental physical properties such as surface magnetism can be studied. Nanoparticles bridge the gap between atomic or molecular structures and bulk materials.

2.2.1 Superparamagnetism

Superparamagnetism is a type of magnetism, which appears in nanosized ferromagnetic or ferrimagnetic particles. For nanoparticles smaller than a critical diameter, the reduction of dipolar energy by introducing a domain wall is less than the increase by the domain wall energy. They stay in a single-domain state. Inside single domain nanoparticles, magnetic moments are in ferromagnetic or ferrimagnetic ordering. The overall magnetic moments in the single-domain state can be considered as superspins with a huge magnetic moment. As the nanoparticle size is reduced, the energy barrier $\Delta E = KV$ due to anisotropy becomes smaller compared to the thermal energy $k_B T$. The superspin can then be easily flipped by thermal fluctuations. At high temperatures, the thermal energy is higher than the energy barrier. Therefore, the superspins of an ensemble of nanoparticles can randomly be flipped similar to a paramagnet, which is known as superparamagnetism.

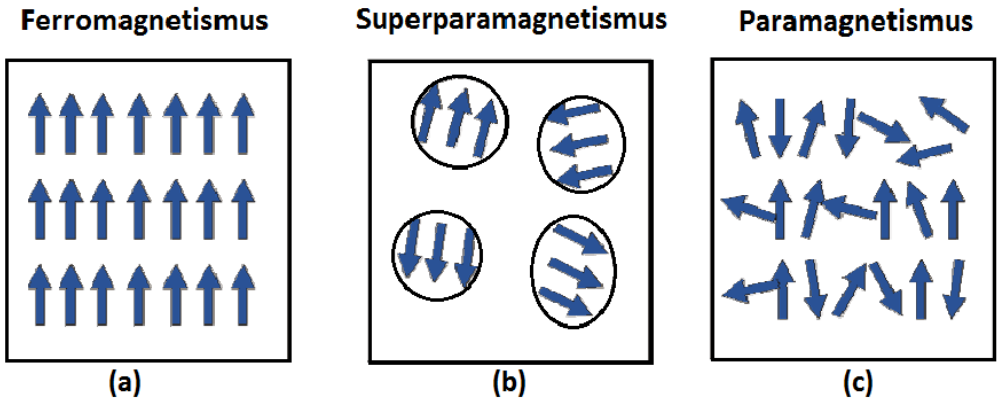

Figure 5: Schematic illustration of magnetic moments in (a) ferromagnet,(b) superparamagnet and (c) paramagnet [8]. Each circle in (b) represents a single domain nanoparticle.

The characteristic switching time of a superparamagnetic nanoparticle is given by the N*é*el-Brown law:

$$\tau_N = \tau_0 \, exp\left(\frac{KV}{k_B T}\right) \tag{2.2.1}$$

It defines the average time between two superspin flips, where τ_0 is the elementary spin flip time with a typical value of 10^{-9} s. If we measure a much longer time than the relaxation time, the magnetization flips several times during the measurement and results in zero magnetization in average. In contrast, when the relaxation time is much longer than the measuring time τ_m, the magnetization stays basically unchanged during the measurement and appears to be in a blocked state.

Bulk ferromagnetic or ferrimagnetic materials transform to paramagnets above

their Curie temperatures. For superparamagnetic nanoparticles a characteristic temperature can be observed in the measurement. This is known as blocking temperature T_B:

$$T_B = KV/k_B ln(\tau_m/\tau_0) \tag{2.2.2}$$

This blocking temperature depends on the measuring time, which is about 10 s for a SQUID measurement, and $10^{-10}-10^{-7}$ s for neutron scattering experiments. Instead of changing the measuring time, the magnetization is usually measured as a function of temperature in the experiment, and the blocking temperature indicates the crossover between isotropic and blocked superparamagnetism [9].

2.2.2 Interacting Nanoparticles

As discussed in 2.2.1, superparamagnetic nanoparticles are by definition isolated, the magnetic interactions between nanoparticles have been neglected. By taking into account different types of magnetic interactions, the spin structures of the nanoparticles can be influenced. Self assembly of the nanoparticles is significantly affected by these magnetic interactions.

Magnetic dipole interactions

Magnetic dipole interaction between two magnetic dipoles $\vec{\mu}_1$ and $\vec{\mu}_2$ separated by a distance $\vec{r}$ is described by:

$$E_d = \frac{\mu_0}{4\pi r^3}\left[\vec{\mu}_1 \cdot \vec{\mu}_2 - \frac{3}{2}(\vec{\mu}_1 \cdot \vec{r})(\vec{\mu}_2 \cdot \vec{r})\right] \tag{2.2.3}$$

In bulk materials, magnetic moments are a few Bohr magnetons, an thus magnetic dipole interactions between atoms are very small and have a negligible influence on the magnetic ordering compared to exchange interactions described in 2.1.1. However, ferromagnetic or ferrimagnetic nanoparticles of 10 nm diameter can have magnetic moments in the order of 10^3-10^4 Bohr magnetons, and therefore the energy E_d produced by dipole interactions between nanoparticles can be significantly high. Below a critical temperature $T_c \approx E_d/k_B$, the magnetic moments of nanoparticles can order themselves even at very high temperature [10]. Figure 6 shows different systems composed by interacting or non-interacting nanoparticles.

Exchange interactions

Exchange interactions play an important role in magnetic long-range order as introduced in 2.1.1. For different nanoparticle systems, different types of exchange interactions have to be considered: (a) tunneling exchange interaction when nanoparti-

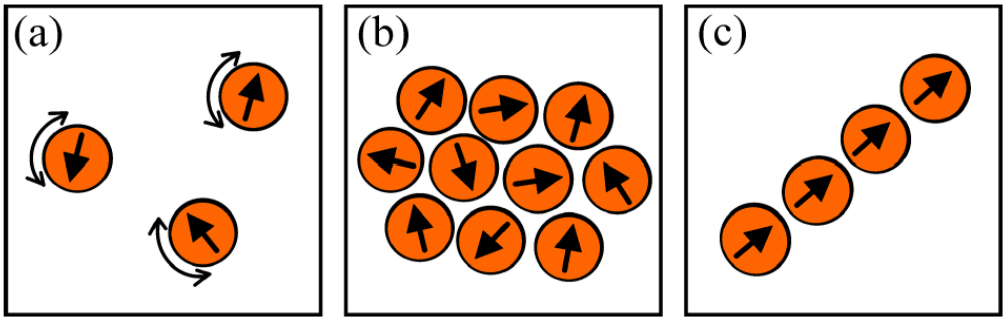

Figure 6: (a) Isolated nanoparticles (superparamagnetic state) (b) Interacting nanoparticles forming a superspin glass[11, 12] (c) Nanoparticles forming a chain with aligned dipole moments [10]. A ferromagnetic ordering of the magnetic moments is favored to be magnetized along the chain direction without applied field. In dense nanoparticle arrays also a superferromagnetic state can be found[11, 12].

cles are in a few nanometers distance [11], (b) direct exchange interaction through the surface spins of neighouring particles in close contact [7], (c) RKKY (Rudermann-Kittel-Kasuya- and Yosida) and interaction via polarization for metal particles in metal matrix [13].

Spin glass and super-spin glass

In some lattices, for example as shown in figure 7, it is not possible to find a ground state for the third spin entirely satisfying all the interactions in the system. Instead, the system is frustrated in several metastable low energy states. A spin glass is a both disordered and frustrated magnetic system. Unlike normal random systems, a spin glass exhibits a phase transition at a particular temperature called spin glass temperature T_g, below which a metastable frozen state clearly different from high temperature disordered state is observed. Below the spin glass temperature T_g, the magnetic moments in spin glasses are collectively ordered in a spin glass phase with peculiar and interesting properties [14].

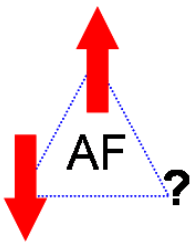

Figure 7: Frustrated antiferromagnetic triangular lattice. The third spin cannot entirely satisfy both neighboring spins to form antiferromagnetic order. The system is frustrated.

Instead of magnetic atoms, if we distribute nanoparticles randomly in a non-

magnetic lattice and have a random orientation of the easy axes, this system will have similarities to spin glasses in the magnetic properties. This kind of interacting nanoparticle system in known as super-spin glass.

2.2.3 Antiferromagnetic Nanoparticles

Antiferromagnetic nanoparticles have received much attention because of their interesting fundamental magnetic properties, e.g. surface and finite-size effects. A perfect antiferromagnetic material shows zero net magnetization at zero field, because the sublattice magnetizations have same size but opposite directions. In nanoparticles uncompensated spins due to the breaking of sublattice pairing on the surface of nanoparticle have been proposed by Néel [15]. These uncompensated spins lead to a small net magnetic moment, which is responsible for the unique magnetic properties exhibited in antiferromagnetic nanoparticle systems.

An interesting interaction between the surface spins in an antiferromagnetic nanoparticle and a ferromagnet in close contact is known as exchange bias. A shift of the hysteresis loop can be observed below the Néel temperature T_N of the antiferromagnet. This effect will be discussed later (in 2.2.4) in detail . The magnetic behavior of antiferromagnetic nanoparticles such as CoO, Co_3O_4, NiO, MnO has been studied for decades. In this thesis, we focus on antiferromagnetic MnO nanoparticles.

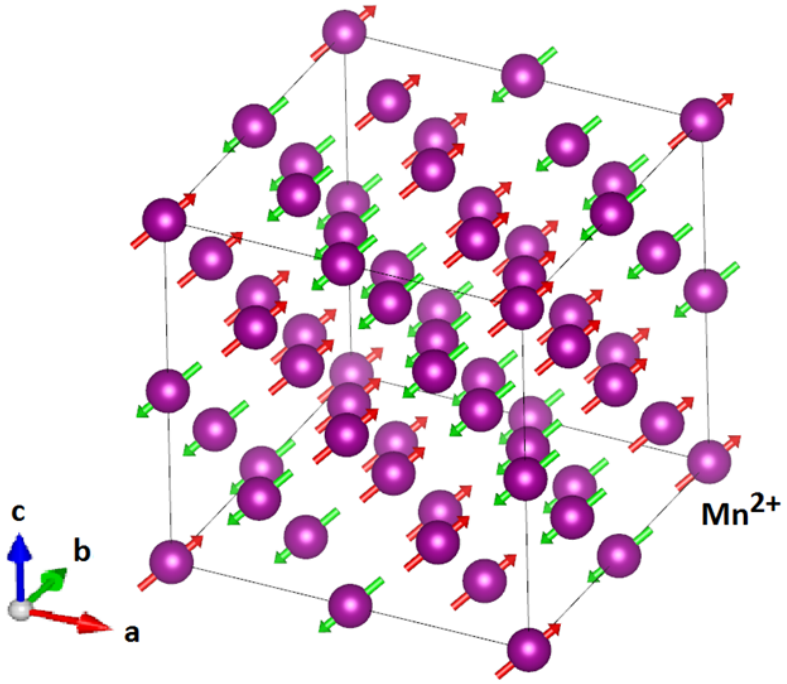

Figure 8: Magnetic spin structure of MnO.

Mangenese oxide (MnO) is a well-known cubic antiferromagnet with a N*é*el temperature of 120K in bulk [1]. As shown in figure 8, spins in MnO lie parallel or antiparallel along the [111] direction. Magnetic moments in neighboring (111) planes are antiparallel. Mn^{2+} has a total angular momentum $|\vec{J}| = |\vec{S}| = \frac{5}{2}$, which means for the orbital momentum $|\vec{L}| = 0$. As mentioned in section 2.1.2, magnetocrystalline anisotropy results from the spin-orbit coupling. Mn^{2+} does not have an orbital momentum, so the MnO does not have magnetocrystalline anisotropy.

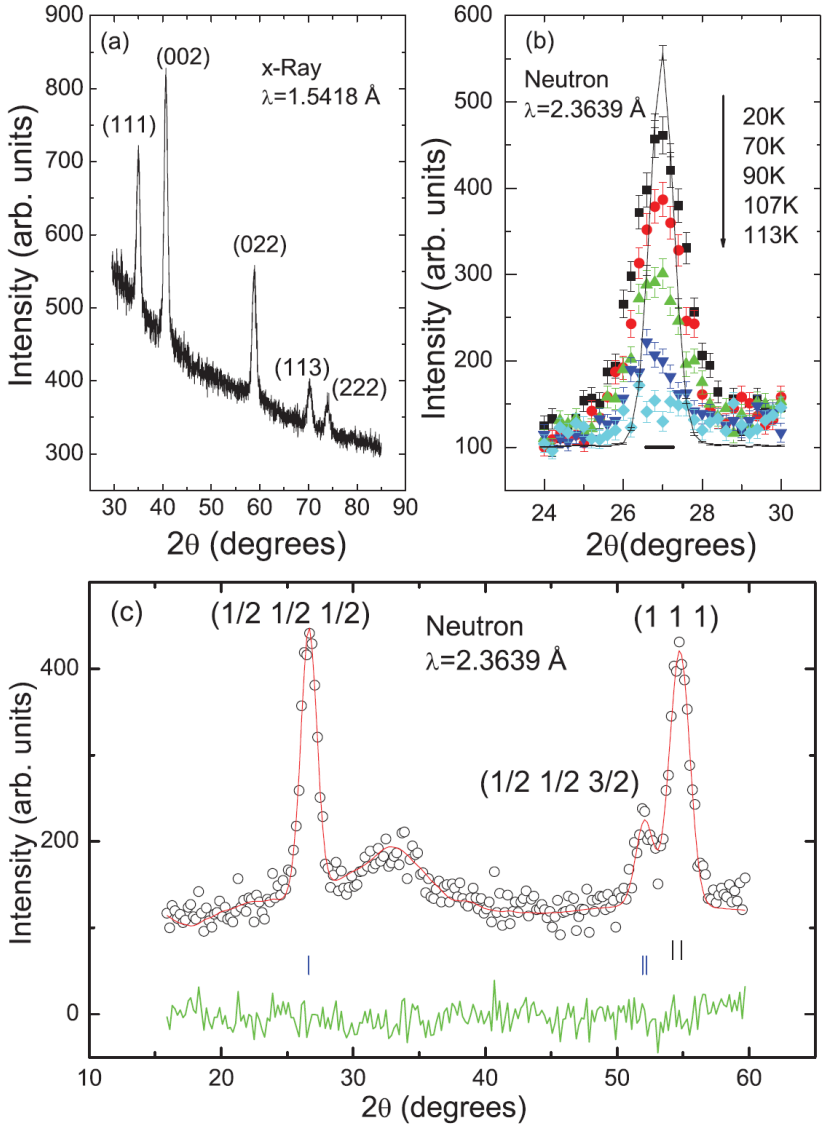

Figure 9: Experimental results of spherical MnO nanoparticles of 8 nm diameter using (a) X-ray diffraction. (b) The temperature dependence of the (1/2, 1/2, 1/2) Bragg peak. The solid line is the scaled data for the bulk material and the horizontal bar indicates the full width at half maximum (FWHM) of the instrumental resolution. (c) Neutron diffraction data at 20 K. The short vertical lines indicate the nuclear Bragg peak (111) and magnetic Bragg peak (1/2 1/2 1/2) [4].

Antiferromagnetic MnO nanoparticles have been studied previously [2, 3, 4]. X-ray diffraction, neutron diffraction as well as magnetometry experiments have been performed on different sizes of monodispersed MnO nanoparticles. As shown in figure 9(a) the Bragg peaks of 8 nm MnO nanoparticles measured by X-ray diffraction are at slightly lager 2θ angles relative to the MnO bulk data, and the lattice parameter of the nanoparticles are calculated to be smaller than that of the bulk. The magnetic Bragg peak and the nuclear (111) peak obtained from the neutron scattering can be well described by the bulk MnO magnetic structure. It can be clearly seen from figure 9(b) that the magnetic Bragg peaks are broadened compared to the bulk.

According to the neutron scattering data, about 80% of Mn ions are estimated to be magnetically ordered. This result is explained by a model that the nanoparticles have a antiferromagnetic core like bulk MnO with disordered spins on the surface [4]. The antiferromagnetic order and structural transition of MnO have be measured not only in bulk MnO but also in MnO nanoparticles. Figure 10 shows that both the magnetic moment and the antiferromagnetic transition temperature are reduced in the nanoparticle sample compared to the bulk. A rounding of the magnetic phase transition of MnO nanoparticles is observed in contrast to the well-known first order phase transition in bulk MnO [3].The continuous character of the phase transition and the unusual temperature dependence suggests that disordered surface spins are present.

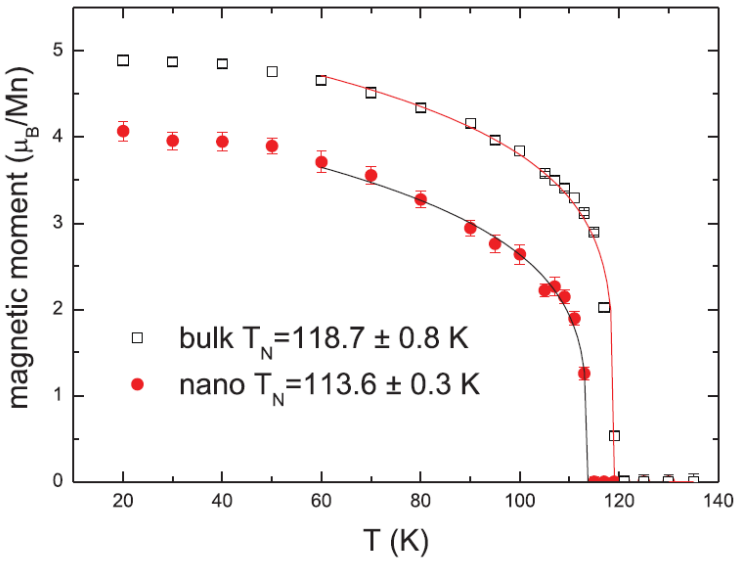

Figure 10: The temperature-dependent magnetic moment of the MnO bulk and 8 nm MnO nanoparticles [4].

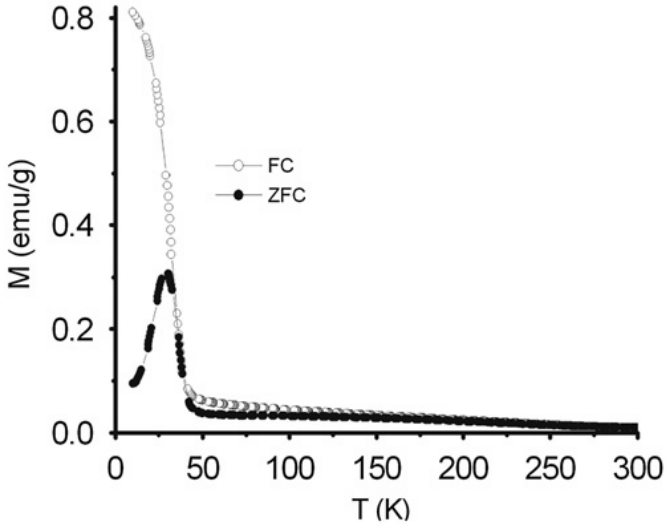

Figure 11: Zero field cooled (ZFC) and field cooled (FC) magnetization of MnO nanoparticles as a function of temperature in 100Oe [2].

Figure 11 shows the zero field cooled (ZFC) and field cooled (FC) magnetization curves measured by magnetometry [2]. The ZFC curve shows a peak at about 30K. However, at the N*é*el-Temperature $\approx$ 120K, surprisingly no feature is visible. Due to the surface magnetism, the peak temperature in the zero-field cooled magnetization of MnO nanoparticles shift towards higher temperatures with decreasing particle size [16]. This behavior of temperature dependence is opposite to other antiferromagnetic nanoparticles such as NiO.

2.2.4 Exchange Bias

Exchange bias or exchange anisotropy results from the interaction on the interface between an antiferromagnet (AFM) and a ferromagnet (FM). It is a unidirectional anisotropy [17]. The Curie temperature T_C of ferromagnet is usually much higher than the N*é*el temperature T_N of the antiferromagnet. It is characterized by a displacement of the hysteresis loop along the field axis after cooling the system in a magnetic field from a temperature T with $T_N < T < T_C$ below the N*é*el temperature T_N of the antiferromagnet. This anisotropy was discovered in 1956 by Meiklejohn and Bean while studying Co particles covered by their native antiferromagnetic oxide [18].

Below the Curie temperature T_C, spins in ferromagnet align parallel with the applied field, while spins in antiferromagnet remains random in the temperature range $T_N < T < T_C$ as shown in figure 12a(i). When the system is cooled below T_N in a magnetic field, due to exchange interaction at the interface, the antiferromagnetic

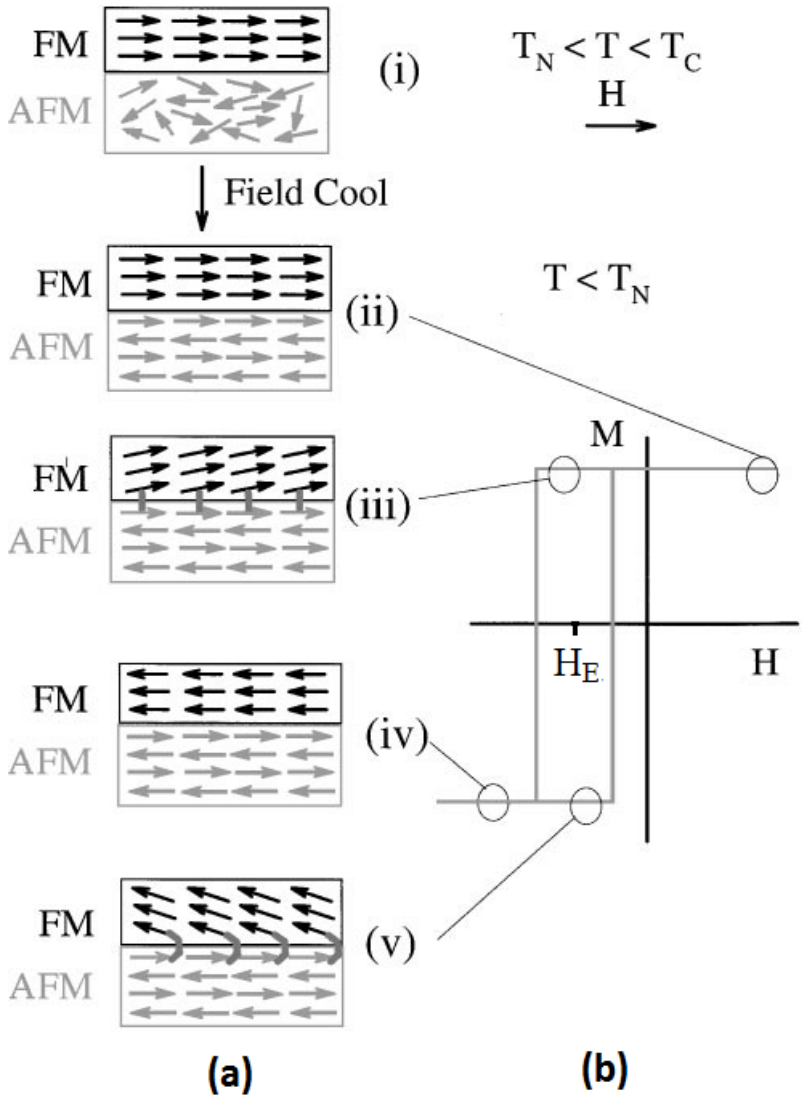

Figure 12: (a) Spin structures of an FM/AFM interface at different stages (i)-(v) of an exchange biased hysteresis loop [17]. The center of magnetic hysteresis loop (b) is shifted from its regular position at H = 0 to $H_E \neq 0$.

spins next to the ferromagnet align ferromagnetically or antiferromagnetically to the ferromagnetic spins. In few systems, spins at the interface between the ferromagnet and antiferromagnet exhibit a perpendicular coupling [17]. The other spins in the antiferromagnet follow the antiferromagnetic order and produce a zero net magnetization (figure 12a(ii)). For sufficient antiferromagnetic anisotropy, antiferromagnetic spins stay unchanged as the magnetic field is reversed. Via the interface coupling, the antiferromagnetic surface spins try to prevent the rotation of ferromagnetic spins, and keep them in the original alignment. The ferromagnetic spins can be thought as being biased in a single direction by a field produced by the antiferromagnetic spins, which result a unidirectional anisotropy. An extra field has

to be applied to overcome the anisotropy. Therefore, the coercive field and the field needed to flip all ferromagnetic spins becomes larger (figure 12a(iii) - (iv)). For the same reason, ferromagnetic spins need a smaller field to flip back to the original direction. The ferromagnet appears to be favourably magnetized in the direction in which it was cooled rather than the other, and exhibits a shift of the hysteresis loop [17]. Exchange bias disappear near the antiferromagnetic N*é*el temperature confirming that it is the presence of the antiferromagnetic material which causes this anisotropy.

Exchange bias is not only interesting in thin layers, but also in nanoparticles, for example, ferromagnetic nanoparticles with an antiferromagnetic shell, or dimer nanoparticles, which contain a antiferromagnetic nanoparticle in close contact to a ferromagnetic nanoparticle. Exchange bias has attracted much attention because of their applications in permanent magnets, magnetic sensors and providing a reference direction in read heads of hard disk drives [19, 17]. Spin valve GMR (giant magnetoresistance) devices developed in recent years are based on exchange bias. They consist of two ferromagnetic layers separated by a non-magnetic layer, where one of the magnetic layer is exchange biased by an antiferromagnetic layer. The resistance across the device is sensitive to the relative orientation of the two ferromagnetic layers. These magnetic layers can be replaced by nanoparticles to reduce the device volume.

2.3 Monte Carlo Simulations

The Monte Carlo method was introduced in the middle 1940s. It contains a class of numerical computations based on repeated random sampling. Interactions between two atoms can be easily described and solved by equations. To understand complex systems containing a large amount of atoms, it is not feasible to solve these equations analytically. Large systems with random orientated particles can be simulated using the Monte Carlo method. In each simulation, the uncertain parameters are sampled and the results of the simulation represent the performance of the system. Each simulation has equal possibility, it represent a possible outcome from a real experiment.

The Metropolis algorithm is the most often employed physical sampling routine, which minimizes the free energy of a system. Here it is used to simulate the spin structure of nanoparticles. To simulate the magnetic behavior, the spin is usually used as the elementary unit. Before starting the simulations, a Hamiltonian has to be chosen. It describes the interactions between magnetic spins in nanopartices.

Random numbers are used to realize statistical fluctuations in order to generate the correct thermodynamical probability. In the simulation, the Metropolis algorithm picks a random spin, and calculates the total energy E_p of the system. A test rotation is then performed using the ansatz of a Heisenberg model (i.e. 3d vector spins). The total energy of the new system E_n is calculated and compared with the previous system. With a Metropolis acceptance ratio given by [20]

$$A = \begin{cases} e^{-\Delta E/k_B T} & \text{if } E_n > E_p \\ 1 & \text{if } E_n \leq E_p \end{cases} \tag{2.3.1}$$

the new system will be accepted, otherwise the previous system will stay [21, 22]. According to the Metropolis algorithm, the system accepts the configuration with a lower free energy just as in a real system. The Metropolis algorithm provides the possibility to study the temperature and field dependence of the spin structure in nanoscale. In this thesis, the spin structure and magnetic properties of MnO nanoparticles have been simulated using the Monte Carlo method and the Metropolis algorithm. It will be discussed in sections 4 and 5.

3 Experimental

In order to study the spin structure inside single MnO nanoparticles and FePt@MnO heterodimer nanoparticles, as well as the influence of exchange bias inside FePt@MnO dimers onto the spin structure in MnO nanoparticles, experimental investigations have been performed using magnetometry and neutron scattering. The magnetic properties of MnO nanoparticles are probed and compared with previous results. The magnetic behavior of the FePt@MnO heterodimer nanoparticles are studied.

3.1 Synthesis of Nanoparticles

The nanoparticles used in this work are synthesized by Heiko Bauer, Anna Schilmann and Oskar Köhler from the collaboration group of Professor Dr. Wolfgang Tremel of the Institut für Anorganische Chemie und Analytische Chemie of Johannes-Gutenberg-Universität Mainz. Spherical MnO nanoparticles and FePt@MnO heterodimers with different sizes are produced for the investigation of their magnetic properties.

3.1.1 MnO Nanoparticles

MnO nanoparticles were synthesized by thermal decomposition of a manganese oleate precursor [23, 24]. Under argon atmosphere, 7.94 g of manganese chloride tetrahydrate and 22.60 g oleic acid were dissolved in 200 mL of methanol. The solution was stirred while 3.2 g of sodium hydroxide in 200 mL of methanol was added drop by drop to precipitate manganese oleate. After washing with water, ethanol and acetone, the red oily Mn-oleate product was dried in vacuum at 100-150°C for 2 h to produce a deep red waxy solid. Then 1.24 g of the manganese oleate were dissolved in 10 g of 1-octadecene. The solution was degassed with argon to remove moisture and oxygen. The reaction mixture was rapidly heated to 200 °C with 5 °C/min, then the heating rate reduced to 1.5 °C/min before the solution reached 318 °C and held at reflux for 1 h. After this specific heating procedure, MnO nanoparticles were produced. The nanoparticles were washed three times and collected by centrifugation. For storage, the nanoparticles were dissolved in hexane or toluene. With the control of the solvent, reaction time, temperature, and heating rate, MnO nanoparticles of different sizes and shapes can be synthesized.

Figure 13 shows the TEM image of 12nm diameter MnO nanoparticles. The nanoparticles are almost monodisperse and have spherical shape. This sample is used in the magnetometry measurements and neutron scattering experiments at the DNS instrument, the experimental process and results will be discussed later.

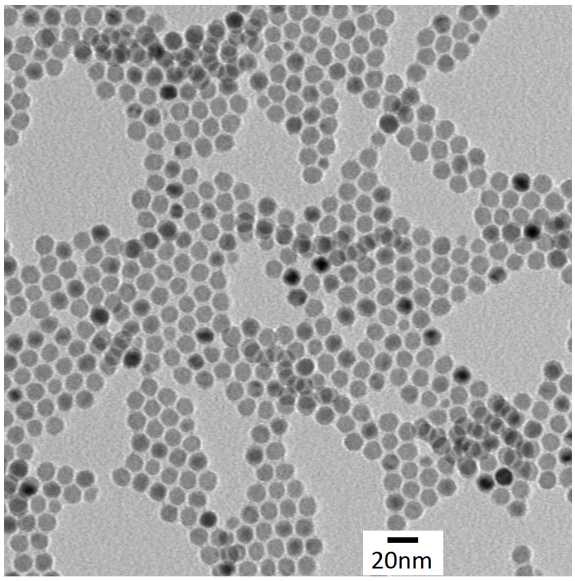

Figure 13: TEM image of 12nm MnO nanoparticles.

3.1.2 FePt/MnO Heterodimer Nanoparticles

Heterodimer nanoparticles composed of an antiferromagnetic nanoparticle in close contact with a ferromagnetic nanoparticles are a novel type of a hybrid nanomagnet. They are multifunctional materials with potential applications in tunable electronics, magnetism or optics. The exchange bias effect takes place at the interface between the ferromagnetic and the antiferromagnetic nanoparticles.

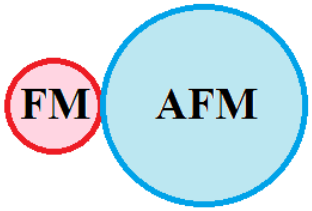

Figure 14: Schematic illustration of a heterodimer nanoparticle composed of a ferromagnetic nanoparticle in close contact with an antiferromagnetic nanoparticle.

In order to synthesize FePt@MnO nanodimers, FePt nanoparticles were first produced. The MnO nanoparticles grew epitaxially on the fcc FePt seeds. Monodisperse FePt nanoparticles were prepared according to the following procedure [23]. Under argon atmosphere, platinum acetylacetonate ($Pt(acac)_2$), 1,2- hexadecanediol, oleic acid, and oleylamine were mixed with dioctyl ether. After the solution was held at 70°C for 1h to remove oxygen and moisture, it was heated to 120°C and iron pentacarbonyl ($Fe(CO)_5$) was added. The temperature was rapidly increased to 298°C, FePt nanoparticles were synthesized during 30 min of reaction. After the

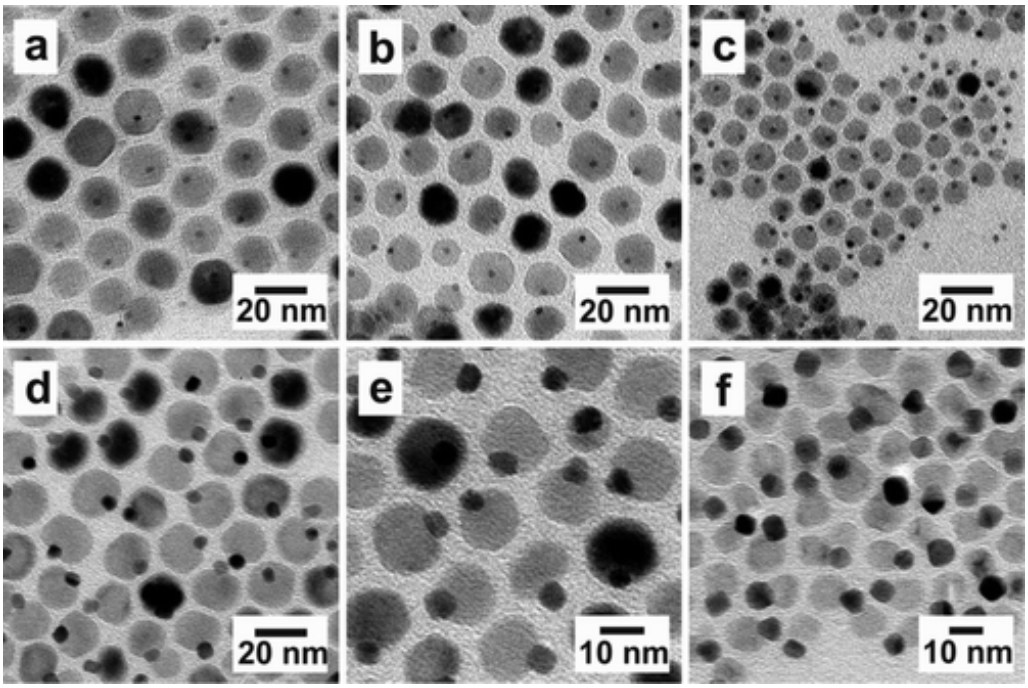

Figure 15: FePt@MnO nanoparticles with different sizes. (a) 3nm@17nm, (b) 3nm@15nm, (c) 3nm@9nm, (d) 6nm@17nm, (e) 6nm@12nm, (f) 6nm@9nm [23].

mixture was cooled to room temperature, FePt nanoparticles were washed. In order to stabilize the nanoparticles, oleic acid and oleylamine were added in the solution, they adhered on the surface of single nanoparticles and avoid them to agglomerate. The precipitation was stored in hexane at low temperature. To prepare the heterodimer, FePt nanoparticles with desired size were selected, and dissolved in 1-octadecene with small amount of oleic acid and oleylamine, the solution was mixed with manganese oleate, oleic acid, oleylamine, and 1-octadecene. The size of the MnO nanoparticle can be achieved by controlling the amount of Mn oleate added to the reaction mixture. The solution was degassed and heated to 315 °C. After the substance reacted for 30 min, the solution was cooled to room temperature. The final product was washed, collected by centrifugation and stored in hexane. Figure 15 and 16 show several examples of dimer nanoparticles with different sizes. The smaller black points indicate the FePt nanoparticles, the bigger brighter ones represent the MnO nanoparticles. The FePt@MnO nanodimers are monodisperse and both FePt and MnO nanoparticles are produced in spherical form.

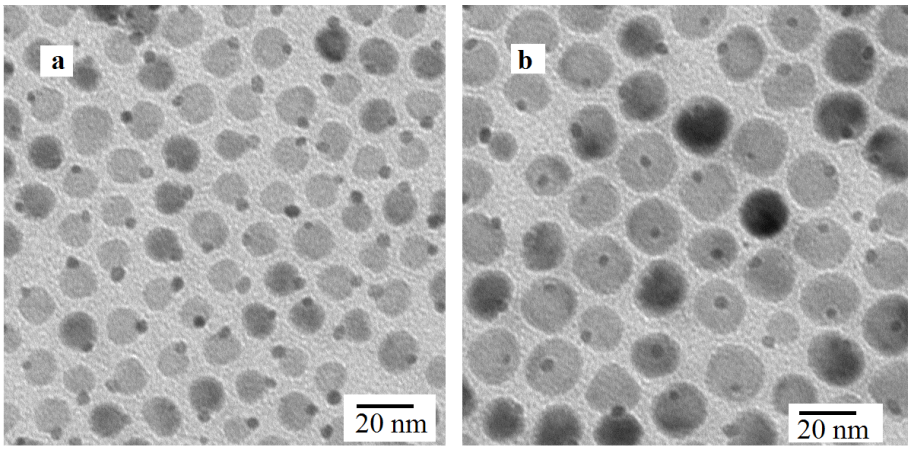

Figure 16: Two samples of FePt@MnO dimer nanoparticles used for neutron scattering at the D7 instrument. (a) 6nm@11nm and (b) 6nm@16nm.

3.2 Magnetometry

A magnetometer measures the magnitude and direction of a magnetic field. Magnetic moments of nanoparticle systems can therefore be measured by sensitive magnetometers. Temperature and field dependence of the magnetic moments, for example zero field cooled (ZFC), field cooled (FC) magnetization curves and hysteresis loops, can be obtained by a magnetometer to characterize different magnetic systems.

3.2.1 SQUID-Magnetometer

SQUID (superconducting quantum interference device) magnetometry is a highly sensitive method to measure the magnetic moment of a sample. The magnetic property measurement systems (MPMS) from Quantum Design is a magnetometer based on a RF-SQUID to study the magnetic properties of small samples over a broad range of temperatures and magnetic fields. MPMS provides rapid and precise measurements from 1.9 to 400 K and an external magnetic field until 7 T. Using an additional sample space oven option the temperature range from 300K to 800K can be reached.

An MPMS system is comprised of two cabinets and a computer. These components are shown in figure 17. The liquid helium dewar for cooling and the probe assembly including the Temperature Control Module (TCM) with the MPMS superconducting magnet and the SQUID detection system are mounted in the right cabinet. The sample transport mechanism is mounted on the top of the TCM. The left cabinet combined with a computer compose the associated control system of the MPMS. The MPMS control console provides automatic control and data collec-

Figure 17: MPMS from Quantum Design [25].

tion. The software MPMS MultiVu can be used to control the measurements. For a complex and long measurement procedure, a sequence of commands can be programmed to make sure that the system condition is stable during the measurements.

The temperature control system of the MPMS magnetometer is installed inside the liquid helium dewar as shown in figure 18. It contains basically two temperature sensors. Samples fixed in a drinking straw are inserted in the sample space with the help of a sample rod. Two thermometers are used to control the sample temperature. The primary thermometer is located at the zero position of the SQUID pickup coils, and the secondary thermometer is located under the bottom of the sample tube. In order to cool the sample down to low temperature, liquid helium in the dewar is allowed continuously entering in the bottom of the cooling annulus. The liquid helium absorbs heat from the sample space and turns into gas. The gas helium is pumped out of the cooling annulus. The heating power of the sample space is provided by a chamber heater, which heats directly the sample tube, and a gas heater, which heats the helium gas surrounding the sample space and transfers the thermal energy to the sample tube.

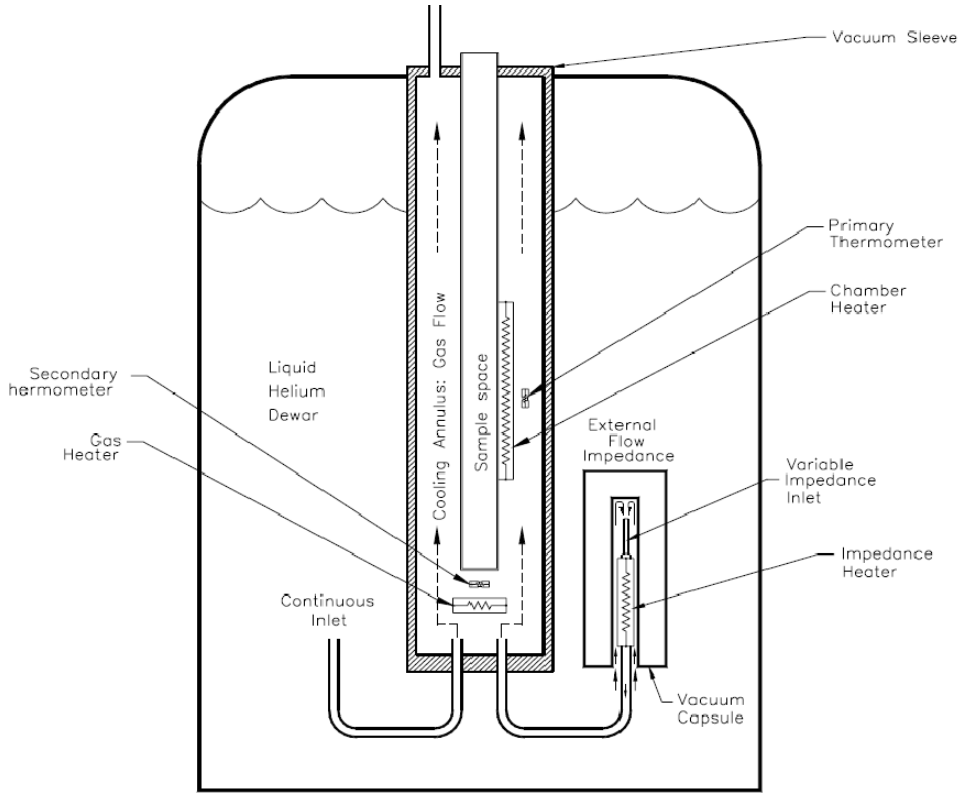

Figure 18: Temperature control system of the MPMS magnetometer [25].

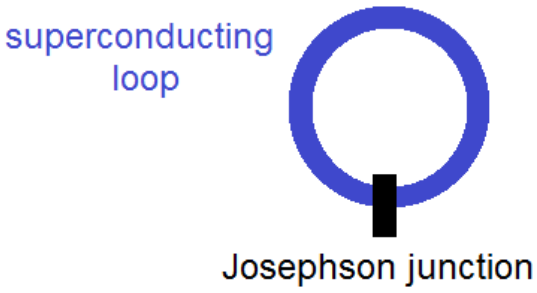

Figure 19: Schematic structure of a SQUID-ring.

A SQUID-ring is basically composed of a superconducting loop interrupted at one point by a weak link as shown in figure 19. For RF-SQUID technique the superconducting loop produces an inductance, and the Josephson junction produces a capacity. The SQUID is coupled with an oscillating LC circuit with a resonant frequency of $f_{res} = \sqrt{1/LC}$. The magnetic flux Φ penetrating the superconducting ring is quantized $\Phi = n\Phi_0$, in which $\Phi_0 = h/2e$ is the magnetic flux quantum and n is an integer. Between two sides of the Josephson junction, a phase difference in the superconducting wavefunction is given by $\varphi = \psi_2 - \psi_1$. When the external magnetic flux is increased in the SQUID, the supercurrent depends on the flux penetrating

the ring. According to the Josephson relation, the supercurrent flowing through the junction is given by

$$I_s = I_{sc} \cdot sin(\varphi) \tag{3.2.1}$$

$$\text{with } I_{sc} = I_0 \frac{sin(\frac{\pi\Phi}{\Phi_0})}{\pi\frac{\Phi}{\Phi_0}} \tag{3.2.2}$$

This flux dependence of the Josephson effect could be exploited for very sensitive magnetometry. In practice one employs RF-SQUID technique, where the SQUID-ring constitutes a non-linear element in an oscillator circuit (figure 20).

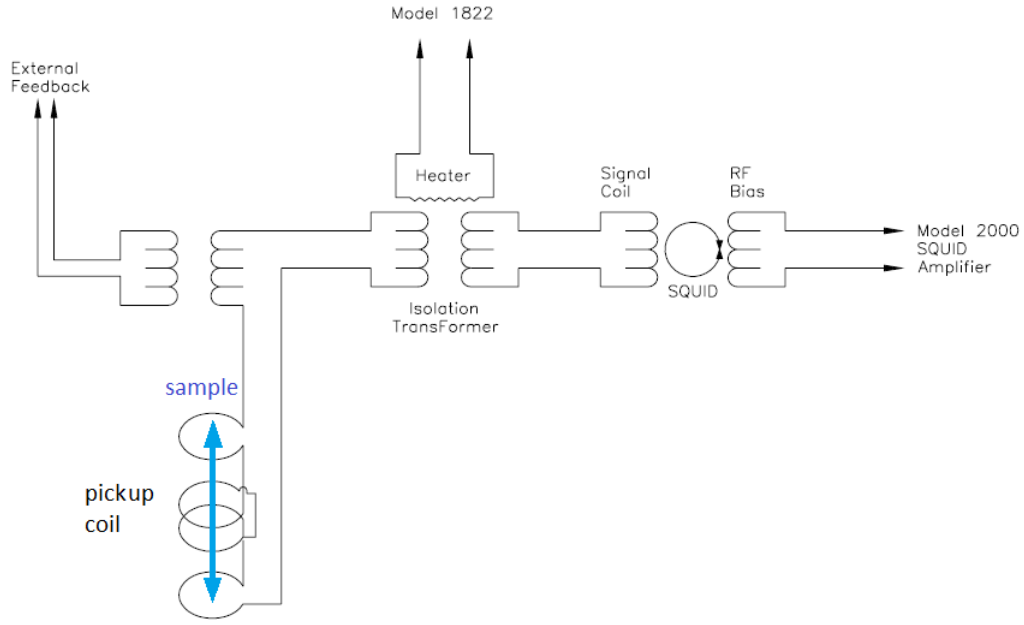

Figure 20: Detection system of a RF-SQUID magnetometer [25].

The Reciprocating Sample Option (RSO) of the MPMS measures the magnetic moment of a sample by moving it sinusoidally through the SQUID pickup coils (figure 20). The pickup coils are designed to reject the constant magnetic field produced by the superconducting magnet. When a sample is passed through the pickup coils, a current is induced proportional to the magnetic moment of the sample. The detected signal in the pickup coils is coupled to a SQUID sensor using a superconducting isolation transformer. The isolation transformer contains a superconducting heater winding to prevent the persistent current induced by the field change of the superconducting magnet. RSO measurements have a sensitivity of approximately 5×10^{-9} emu.

3.2.2 PPMS-Magnetometer

The Physical Property Measurement System (PPMS) is a multi-propose measurement platform from Quantum Design. With the VSM-option it can also used as a magnetometer. Compared to the MPMS, it provides a larger temperature range from 1.9K to 400K and with an oven option from 300K to 1000K. The sample can be measured in an external magnetic field from - 9T to 9T. The PPMS has a sensitivity of 10^{-6}emu. Using a VSM linear motor transport, the sample is oscillated near a pickup coil. A voltage is induced in the pickup coil and detected by the electronics. The measurements can be automatically controlled by the MultiVu software.

Figure 21: PPMS magnetometer with VSM option from Quantum Design [26].

The control console of the PPMS is connected to a computer shown in the left of figure 21. The probe assembly of the PPMS is installed in the liquid helium drawer and the VSM option is mounted on the top of the helium drawer. The sample is sticked on the sample holder using non-magnetic glue and attached to the end of a sample rod. The sample is placed at the center of the pickup coil and vibrated to induce a voltage V_{coil} given by:

$$V_{coil} = \frac{d\Phi}{dt} = \left(\frac{d\Phi}{dz}\right)\left(\frac{dz}{dt}\right) \tag{3.2.3}$$

where Φ is the magnetic flux in the pickup coil, z is the vertical position of the sample, t is the time. For a sinusoidally oscillation, the induced voltage V_{coil} can be

described by:

$$V_{coil} = 2\pi CmAsin(2\pi ft) \tag{3.2.4}$$

with C is a coupling constant, m is the DC magnetic moment of the sample, A is the amplitude of oscillation, and f is the frequency of oscillation.

3.3 Neutron Scattering

Neutron scattering is a useful method to study the magnetism in condensed matter. Neutrons are electrically neutral and have spin $\frac{1}{2}$. Neutrons can interact with atomic nuclei and magnetic spins of electrons. They are ideal to study the microscopic magnetic structure of a sample. Cold and thermal neutrons have a similar wavelengths as atomic spacings. The atomic structure of a sample can be determined in the range from picometer to the 100 μm using neutron scattering. In this work, the antiferromagnetic order parameter of MnO nanoparticles as well as the influence of the FePt nanoparticles on the order parameter of MnO nanoparticles are measured at the DNS instrument at MLZ in Garching, Germany and at the D7 instrument at ILL, Grenoble, France.

3.3.1 DNS - Instrument

The Diffuse Neutron Scattering (DNS) instrument is a high-flux time-of-flight spectrometer with xyz- polarization analysis. It is located in the Heinz Maier-Leibnitz Zentrum in Munich (FRMII reactor), which has a thermal effective power of 20MW. DNS is suitable to study magnetic and lattice correlations in condensed matter such as highly frustrated magnets and correlated electron systems. The polarization analysis allows to separate the magnetic, nuclear coherent, nuclear spin-incoherent scattering. The small magnetic moments of powder samples can be separated from the background. DNS proves to be a powerful instrument to perform polarized powder diffraction measurements and to study the magnetic properties of single-crystal samples and soft matters. The schematic illustration of DNS is shown in figure 22. The neutrons from the source in ① are guided and focused through a monochromator ② and slits ③ to the DNS instrument. The neutrons can be polarized to a desired direction by polarizers ⑤ and xyz coils around the sample ⑦. A flipper before the sample space controls the spin flip (SF) and non-spin flip (NSF) processes. After the neutrons impinge onto the sample, the polarized scatterings are collected in the 24 detector banks with polarization analysis ⑧, and the non-polarized neutrons are detected in the position sensitive ^{3}He detector banks ⑨. DNS provides neutrons with a wavelength in the range from 2.4 Å to 6 Å. A cryostat can be installed be-

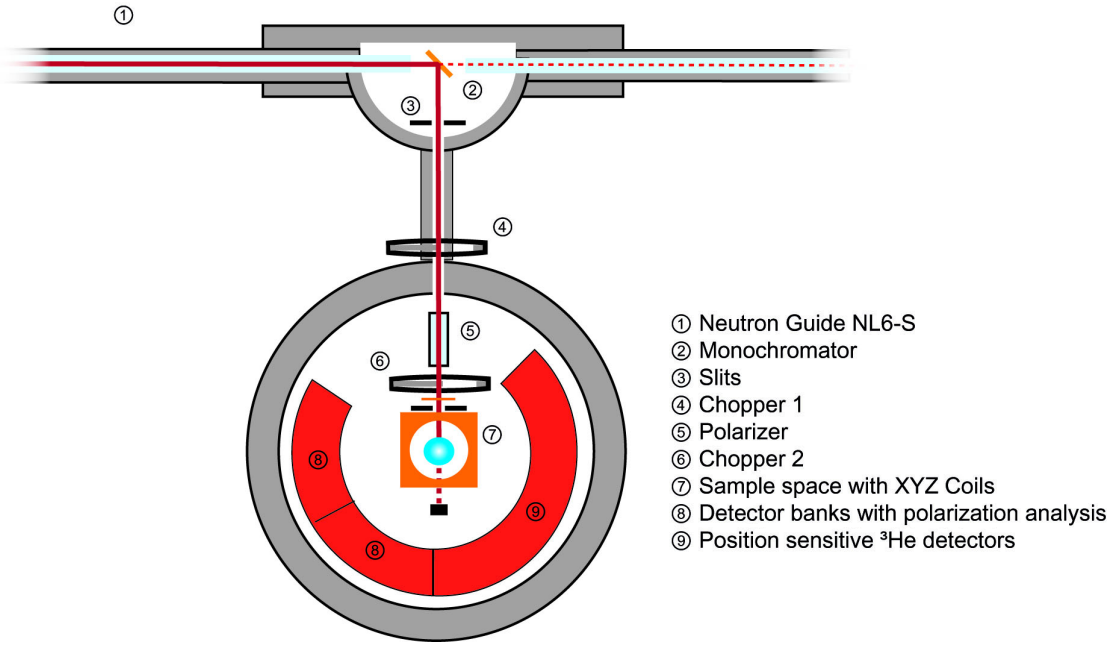

Figure 22: Components of the DNS spectrometer [27].

tween the xyz-coils to reach low temperatures of 20 mK. A vertical magnetic field up to 5 T can be provided by a cryomagnet.

In the experiment, polarized neutron scattering are performed in 6 channels: the neutrons are polarized in x, y, or z- direction measured with SF and NSF. The magnetic, spin incoherent and the nuclear coherent components of the neutron scattering can be separated with the polarization analysis. The separation of the DNS experimental data is based on the following equations [28]:

$$\vec{P} \parallel \vec{Q}:$$

$$I_x^{SF} = \frac{2}{3} I_{inc}^{spin} + 0 + 0 + I_y^{magn} + I_z^{magn} \tag{3.3.1}$$

$$I_x^{NSF} = \frac{1}{3} I_{inc}^{spin} + I_{inc}^{isot} + I_{coh} + 0 \tag{3.3.2}$$

$$\vec{P} \perp \vec{Q}:$$

$$I_y^{SF} = \frac{2}{3} I_{inc}^{spin} + 0 + 0 + I_z^{magn} \tag{3.3.3}$$

$$I_y^{NSF} = \frac{1}{3} I_{inc}^{spin} + I_{inc}^{isot} + I_{coh} + I_y^{magn} \tag{3.3.4}$$

$$I_z^{SF} = \frac{2}{3} I_{inc}^{spin} + 0 + 0 + I_y^{magn} \tag{3.3.5}$$

$$I_z^{NSF} = \frac{1}{3} I_{inc}^{spin} + I_{inc}^{isot} + I_{coh} + I_z^{magn} \tag{3.3.6}$$

$\vec{P}$ and $\vec{Q}$ are the incident neutron polarization and the scattering vector direction, I_{inc}^{spin} is the intensity of the nuclear spin incoherent scattering, I_{inc}^{isot} is the intensity of the nuclear isotope incoherent scattering, *coh* refers to the nuclear coherent scattering, *magn* refers to the magnetic scattering along x, y, z- axis. The x, y-axes are located in the Q-plane, and the z-axis is perpendicular to the x, y-plane. By comparing the equations, different components of the neutron scattering can be separated. The magnetic scattering in y-direction can be obtained by subtracting equation (3.3.1) by (3.3.3).

In the same way, the z-component of the magnetic scattering can be obtained by subtracting equation (3.3.1) by (3.3.5). Then the I_{inc}^{spin} can be calculated with the help of the I_z^{magn} or I_y^{magn}. However, it is not possible to separate the nuclear isotope incoherent scattering from the nuclear coherent scattering. The analysis of the experimental data is achieved by software "dnsplot", which is part of the plot.py software developed by Artur Glavic.

A reference measurements of a NiCr alloy was made for the flipping ratio correction, in which pure isotropic incoherent scattering is expected. The background correction is performed by measuring the empty aluminum sample holder and subtracted from the raw data. The experimental data can be converted to the absolute unit. Vanadium standard measurements are made under the same experimental conditions. The data are normalized to the incoherent scattering of the vanadium standard. The intesity per Mn atom in absolute units can be expressed by

$$\frac{d\sigma_s}{d\Omega} = \frac{I_s N_v}{4\pi n I_v N_s}\sigma_v \tag{3.3.7}$$

where I_s and I_v are the intensities scattered by the sample and the vanadium, n is the number of Mn atoms per molecule and equals to 1, N_s and N_v are the amount of sample and vanadium atoms in the beam, σ_v is the total scattering cross section of vanadium.

3.3.2 D7 - Instrument

The diffuse scattering spectrometer D7 is a time-of-flight spectrometer with full polarization analysis. It is designed to study nuclear and magnetic short range order in frustrated magnets and spin-glasses and magnetic defects in antiferromagnetic materials. Neutrons used for D7 are produced by the reactor at the ILL in Grenoble. This reactor provides a neutron flux of 1.5x10^{15} neutrons per second per cm^2 with a thermal power of 58.3 MW. Neutrons of wavelength 3.1 Å, 4.8 Å or 5.8 Å can

be selected by a vertically and horizontally focusing pyrolytic graphite monochromator. D7 has large solid-angle detectors and high polarized flux, which allows the weak magnetic moments in powder samples and single crystals to be measured in a reasonable time. Figure 23 shows the main components of D7.

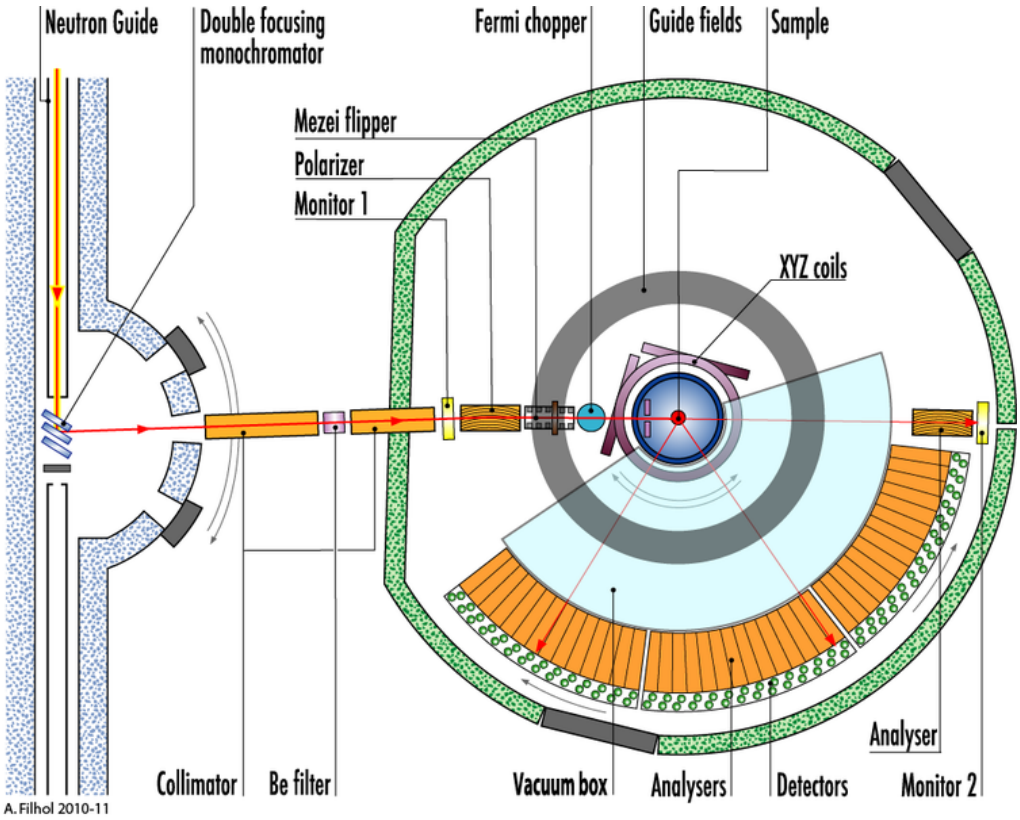

Figure 23: Schematic structure of the D7 spectrometer. The focused and polarized neutrons scatter with the sample and are detected by the wide angle detectors [29].

The xyz- polarization analysis provides full and unambiguous separation of the magnetic, nuclear and spin-incoherent cross sections on a multi-detector neutron spectrometer. This technique requires neutron scattering data collected over a wide range of scattering angles. The polariztion of neutrons in the longitudinal direction P can be expressed as

$$P = \frac{N_+ - N_-}{N_+ + N_-} \tag{3.3.8}$$

where N_+ and N_- are the numbers of neutrons in the + and - Zeeman states. For unpolarized neutrons, $N_+ = N_-$ and $P = 0$. For fully polarized neutrons, $N_+ = 0$ and $N_- = 1$ or $N_+ = 1$ and $N_- = 0$, so $P = \pm 1$. A partially polarized neutron beam has $0 < \mid P \mid < 1$. For a three-dimensional polarization analysis, the scattering

cross sections of a magnetic sample are measured in the following channels [30],

$$\left(\frac{d\sigma}{d\Omega}\right)_x^{NSF} = \frac{1}{2}sin^2\alpha\left(\frac{d\sigma}{d\Omega}\right)_{mag} + \frac{1}{3}\left(\frac{d\sigma}{d\Omega}\right)_{si} + \left(\frac{d\sigma}{d\Omega}\right)_{nuc} \quad (3.3.9)$$

$$\left(\frac{d\sigma}{d\Omega}\right)_x^{SF} = \frac{1}{2}(cos^2\alpha + 1)\left(\frac{d\sigma}{d\Omega}\right)_{mag} + \frac{2}{3}\left(\frac{d\sigma}{d\Omega}\right)_{si} \quad (3.3.10)$$

$$\left(\frac{d\sigma}{d\Omega}\right)_y^{NSF} = \frac{1}{2}cos^2\alpha\left(\frac{d\sigma}{d\Omega}\right)_{mag} + \frac{1}{3}\left(\frac{d\sigma}{d\Omega}\right)_{si} + \left(\frac{d\sigma}{d\Omega}\right)_{nuc} \quad (3.3.11)$$

$$\left(\frac{d\sigma}{d\Omega}\right)_y^{SF} = \frac{1}{2}(sin^2\alpha + 1)\left(\frac{d\sigma}{d\Omega}\right)_{mag} + \frac{2}{3}\left(\frac{d\sigma}{d\Omega}\right)_{si} \quad (3.3.12)$$

$$\left(\frac{d\sigma}{d\Omega}\right)_z^{NSF} = \frac{1}{2}\left(\frac{d\sigma}{d\Omega}\right)_{mag} + \frac{1}{3}\left(\frac{d\sigma}{d\Omega}\right)_{si} + \left(\frac{d\sigma}{d\Omega}\right)_{nuc} \quad (3.3.13)$$

$$\left(\frac{d\sigma}{d\Omega}\right)_z^{SF} = \frac{1}{2}\left(\frac{d\sigma}{d\Omega}\right)_{mag} + \frac{2}{3}\left(\frac{d\sigma}{d\Omega}\right)_{si} \quad (3.3.14)$$

where the x, y and z refer to the incident polarization direction, the NSF and SF indicate the non-spin-flip and the spin-flip measurements, *nuc* represents the nuclear and isotope incoherent scattering, *mag* represents the magnetic scattering and *si* represents the spin-incoherent scattering, respectively. The geometry of the xyz-coordinates is shown in figure 24.

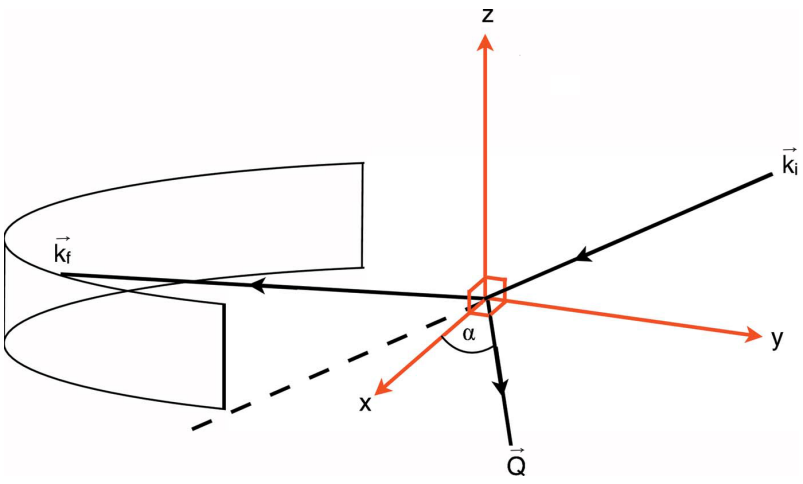

Figure 24: The geometry of an xyz-polarization analysis experiment. The incident neutrons are polarized along the orthogonal x, y or z directions. The incident and scattered neutron wavevectors $\vec{k_i}$ and $\vec{k_f}$ and the scattering vector $\vec{Q}$ lie in the xy-plane. α is the Schärpf angle between the scattering vector $\vec{Q}$ and the arbitrarily positioned x axis [30].

The NSF scattering measures the magnetization components parallel to the neutron spin. The SF scattering measures the magnetization components perpendicular to the neutron spin. The nuclear, spin-incoherent and magnetic scattering cross sections can be separated via linear combinations of the xyz-equations. The magnetic scattering depends on the neutron polarization direction with respect to the scattering vector as well as the orientation of the magnetic moments in the sample. The magnetic cross section can be separated from the nuclear and spin-incoherent scattering by comparing the SF cross sections measured with $\vec{P} \parallel \vec{Q}$ and $\vec{P} \perp \vec{Q}$.

There are two methods to calculate the magnetic cross section [30]:

$$\left(\frac{d\sigma}{d\Omega}\right)_{mag} = 4\left(\frac{d\sigma}{d\Omega}\right)_{z}^{NSF} - 2\left(\frac{d\sigma}{d\Omega}\right)_{x}^{NSF}\left(\frac{d\sigma}{d\Omega}\right)_{y}^{NSF} \tag{3.3.15}$$

$$\left(\frac{d\sigma}{d\Omega}\right)_{mag} = 2\left(\frac{d\sigma}{d\Omega}\right)_{x}^{SF} + 2\left(\frac{d\sigma}{d\Omega}\right)_{y}^{SF} - 4\left(\frac{d\sigma}{d\Omega}\right)_{z}^{SF} \tag{3.3.16}$$

According to the equations above, twice the cross section measured with the incident polarization in z direction as in x or y directions are used to calculate the magnetic cross section. The ratio of the neutron scattering performed with the incident polarization in $x : y : z$ directions is 1:1:2 for a convenient calculation. The nuclear and the spin-incoherent cross sections can be obtained by [30]

$$\left(\frac{d\sigma}{d\Omega}\right)_{nuc} = \frac{1}{6}\left[2\left(\frac{d\sigma}{d\Omega}\right)_{TNSF} - \left(\frac{d\sigma}{d\Omega}\right)_{TSF}\right] \tag{3.3.17}$$

$$\left(\frac{d\sigma}{d\Omega}\right)_{si} = \frac{1}{2}\left(\frac{d\sigma}{d\Omega}\right)_{TSF} - \left(\frac{d\sigma}{d\Omega}\right)_{mag} \tag{3.3.18}$$

where TNSF and TSF refer to the total non-spinflip and total spin-flip cross sections.

To achieve the correct results, the collected data have to be corrected for the background scattering, detector efficiency and solid-angle corrections. Measurements of an empty sample holder, an empty sample holder filled with the same amount of aluminum foil, vanadium and cadmium are performed for the background corrections. For the xyz-polarization analysis, extra corrections for the finite polarization of the incident beam and the analyzing power of the analyzers in the scattered beam have to be undertaken. An amorphous silica (quartz) rod is optimal for this correction. Quartz is a material, which provides good scattering intensity over the whole detector banks. It yields only nuclear scattering. No sf scattering is expected for perfectly polarized neutrons and perfect analyzers. Quartz gives a flipping ratio of the detector, implying the ratio of the correct nsf scattering to the wrongly

attributed sf scattering:

$$F = N_+/N_- \tag{3.3.19}$$

The SF and NSF neutron scattering can be corrected by

$$\left(\frac{d\sigma}{d\Omega}\right)^{corr}_{NSF} = \left(\frac{d\sigma}{d\Omega}\right)_{NSF} + \frac{1}{F-1}\left[\left(\frac{d\sigma}{d\Omega}\right)_{NSF} - \left(\frac{d\sigma}{d\Omega}\right)_{SF}\right] \tag{3.3.20}$$

$$\left(\frac{d\sigma}{d\Omega}\right)^{corr}_{SF} = \left(\frac{d\sigma}{d\Omega}\right)_{SF} - \frac{1}{F-1}\left[\left(\frac{d\sigma}{d\Omega}\right)_{NSF} - \left(\frac{d\sigma}{d\Omega}\right)_{SF}\right] \tag{3.3.21}$$

where $(d\sigma/d\Omega)^{corr}_{NSF}$ and $(d\sigma/d\Omega)^{corr}_{NSF}$ are the corrected differential cross sections. Another error can be caused by multiple scattering of the neutrons in the sample. For example, the polarized neutron spin-flipped twice may be considered as a non-spin-flipped neutron in the analysis. The multiple scattering can be reduced to a minimum by reasonably choice of the sample size and geometry [31, 32] or corrected after data collection by numerical computational methods [33, 34].

4 Simulations

In this thesis, the spin structure and magnetic properties of MnO nanoparticles have been simulated and compared with the experimental results. In this section, the specific realization of the simulation will be explained.

4.1 MnO

To specify the crystal and magnetic structure of antiferromagnetic Manganese oxide, the nearest neighbours and next nearest neighbours have been implemented in the simulations. Two nanoparticle sizes formed by 10×10×10 or 20×20×20 MnO atoms have been simulated in cubic and spherical shape. Simulation of a bulk MnO has also been performed. The Hamiltonian of the system is chosen to be [35]

$$H = J_1^- \sum_{nn}^{p} \vec{S}_i \cdot \vec{S}_j + J_1^+ \sum_{nn}^{a} \vec{S}_i \cdot \vec{S}_j + J_2 \sum_{nnn} \vec{S}_i \cdot \vec{S}_j + D \sum_{nn} {S_{ix}}^2 + g\mu_B \sum \vec{S}_i \cdot \vec{B} \quad (4.1.1)$$

where the J_1^-, J_1^+ are the exchange constants for the nearest neighbours, J_2 is the exchange constant for the next nearest neighbours, $\vec{S}_i, \vec{S}_j$ are neighbouring spins, D is anisotropy constant, S_{ix} is the magnetic spin component in x-direction, B is the magnetic field. At the beginning of the simulation, all the N spins are set in random orientation corresponding to the paramagnetic state of a real system. In each Monte Carlo step a spin $\vec{S}_i$ is randomly selected from the system. Each spin has the same probability of $p = \frac{1}{N}$ to be chosen using a specific random number generator [21]. An attempt orientation $\vec{S}_i{}'$ of the spin is generated. Then the energy difference $\Delta E = E_{attempt} - E_{present}$ between the attempted and the present orientation is calculated. Using the Monte Carlo Metropolis algorithm described in section 2.3, if $\Delta E \leq 0$ the new orientation is accepted. If $\Delta E > 0$, a random number q generated in the interval [0,1] is compared with the Metropolis acceptance ratio $A = exp(-\Delta E/k_B T)$. If q<A the new orientation is accepted, otherwise the system keeps its present state.

The Monte-Carlo simulation analyzes the time dependence of the free energy of a system represented by the Hamiltonian H. The 12 nearest neighbours and 6 next nearest neighbours of a Mn^{2+} is shown in figure 25. In order to avoid the system blocked in a magnetized state, the simulations start at a high temperature (150K) above the critical temperature of the MnO (120K), where all spins are in random orientation. The temperature is reduced at a constant rate to 2K without applied field. At 2K a magnetic field is set and the temperature is increased to 150K to

realize the Zero-field-cooled (ZFC) magnetization procedure. Later the temperature is again reduced with the same magnetic field to reproduce the Field-cooled (FC) magnetization process.

Hysteresis loops at different temperatures are calculated. Before the calculation of the hysteresis, a field cooling procedure is performed to reach the desired temperature. The hysteresis loop starts from its positive saturation, and the magnetic field is decreased in small constant steps. At each field step, 10000 Monte Carlo steps are executed. The total magnetization of the system is calculated and the magnetic field changes to the next value. The field is reduced until the negative saturation state of the system is achieved. The field is later increased, so that the system reaches its positive saturation again. In this way a complete hysteresis loop is simulated.

Information about the coercive field and the remanent magnetization can be obtained from the hysteresis loop. For the magnetic field in the hysteresis loops and the temperature in the ZFC/FC magnetization calculation, 10000 Monte Carlo steps are performed.

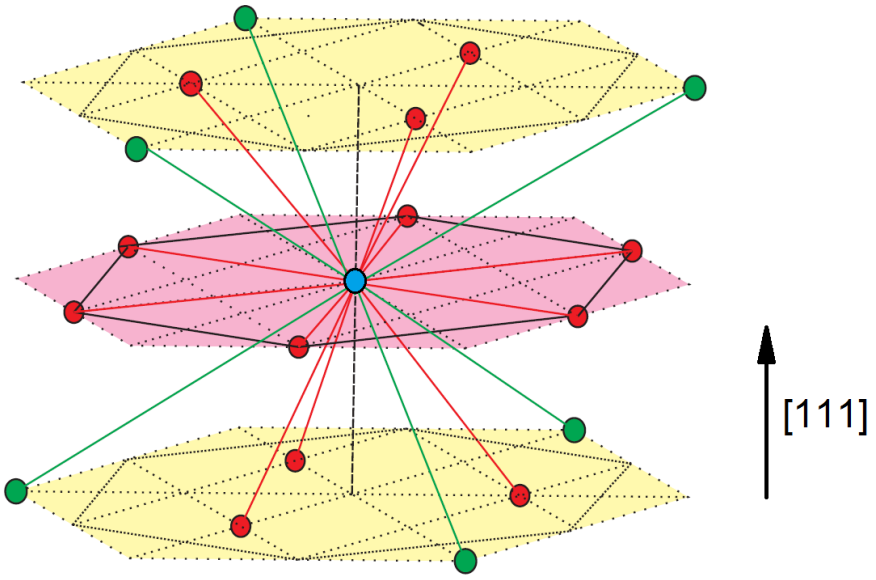

Figure 25: The 12 nearest neighbours (red) and 6 next-nearest neighbours (green) of a Mn^{2+} (blue) in MnO.

5 Results

As discussed in section 3, magnetometry and neutron scattering measurements have been performed to study the magnetic properties of MnO nanoparticles as well as of FePt@MnO heterodimer nanoparticles. Using Monte Carlo methods, the magnetic structures of bulk MnO and MnO nanoparticles with different sizes are simulated. In this chapter, the results of the experiments and the Monte Carlo simulations are presented.

5.1 Experimental Results

MnO nanoparticles and FePt@MnO dimer nanoparticles of different sizes have been studied using a MPMS and PPMS magnetometer from Quantum Design. Zero Field Cooled (ZFC)/ Field Cooled (FC) magnetization curves and the field dependence of the magnetization (hysteresis loops) have been obtained. In order to explain the unusual properties observed in MnO as well as the FePt@MnO nanoparticles, memory effect measurements are performed and TRM/IRM curves are compared with various systems from literature.

In the neutron scattering experiments, the antiferromagnetic order parameter of the MnO nanoparticles are measured as function of temperature. The influence of the exchange bias inside FePt@MnO dimers onto the order parameter of MnO nanoparticles is studied.

5.1.1 Magnetometry

Using both the MPMS and PPMS magnetometer, single MnO and FePt@MnO dimer nanoparticles are characterized by various magnetization measurements. The samples are drop-casted on silicon substrate. Temperature dependences of the magnetization are measured via the ZFC and FC procedure. For a ZFC magnetization measurement, the sample is cooled without an external magnetic field from high temperatures above the N*é*el temperature of MnO to a low temperature (5K), the magnetization is measured during heating the sample in different magnetic fields. A FC magnetization is achieved by measuring the magnetization while cooling the system in the presence of a magnetic field. A broad peak can be observed at low temperature in the ZFC magnetizations of MnO nanoparticles as well as the FePt@MnO dimer nanoparticles. The peak temperatures T_p for various sizes of nanoparticles and in different magnetic field are compared.

Single MnO nanoparticles are probed with diameters of 6 nm, 12 nm, and 19

nm. The temperature dependent (ZFC/FC) magnetization curves of 12 nm MnO nanoparticles are shown in figure 26. In both ZFC and FC curves, no feature at the Néel temperature (120 K) of MnO is observed. Instead, a broad peak is found at low temperature (ca. 24 K) in the ZFC curve.

This phenomenon in the ZFC magnetization is often observed in a superparamagnetic system. The peak temperature in the superparamagnetic system is known as blocking temperature. However, the field dependence of the peak temperature measured by MnO nanoparticles is in conflict with that of superparamagnetic systems. This will be discussed later. The ZFC and FC curves of 12 nm MnO nanoparticles split at ca. 40 K. Such splitting is often seen in a superparamagnetic system or a spin glass due to the freezing of magnetic moments.

Due to the field dependence of the peak temperature, the MnO nanoparticles cannot be superparamagnetic. For an antiferromagnetic MnO, the peak is expected to be measured at the Néel temperature of 120 K. The splitting between the ZFC and FC curves in an antiferromagnetic system is probably due to domain walls. The various spin models for the understanding of MnO nanoparticles will be discussed in section 6.

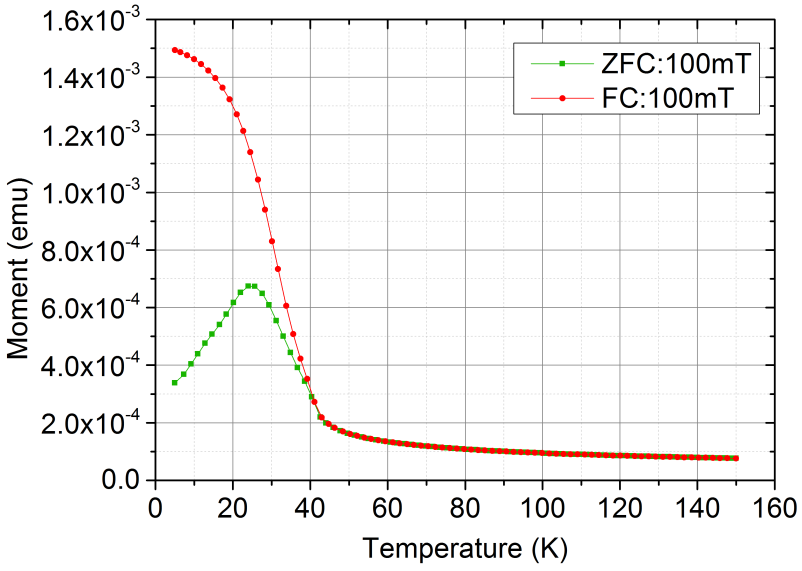

Figure 26: ZFC and FC magnetization of 12nm MnO nanoparticles at 100mT.

Figure 27 exhibits the ZFC magnetization curves of various sizes of MnO nanoparticles measured at different fields. For all these MnO samples, no feature is found near the Néel temperature of MnO. The antiferromagnetic ordering of MnO is pos-

sibly too weak to be measured or destroyed in nanometer size. As the magnetic field is increased, the peak temperatures for the same sample show a weak decrease. Such a weak field dependence is very different from the behavior found in superparamagnetic systems. There, the blocking temperature decreases rapidly with the increase of the magnetic field. This high stability of the peak temperature against the magnetic field is often measured for an antiferromagnetic system.

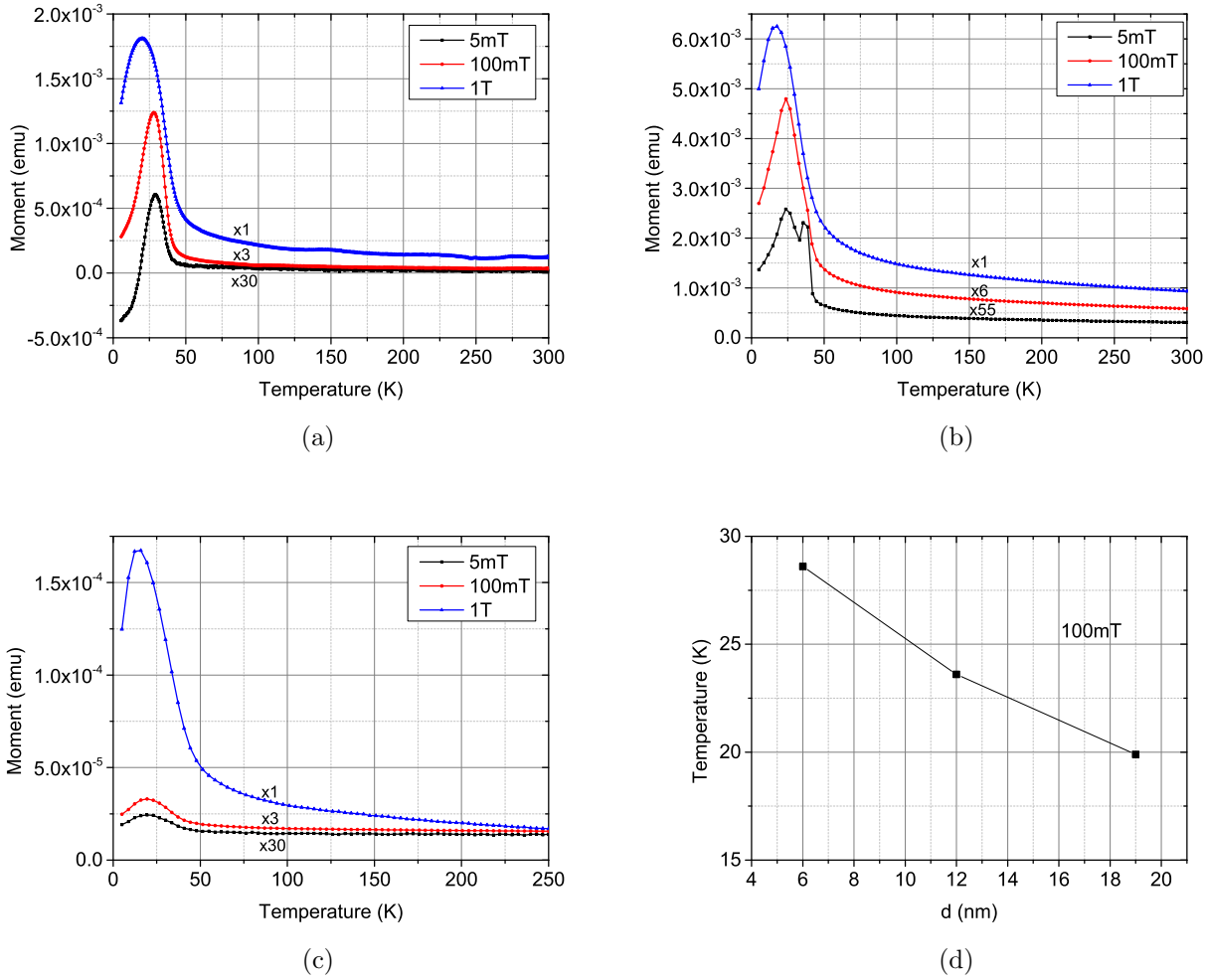

Figure 27: ZFC curves of MnO nanoparticles of (a) 6nm, (b) 12nm, and (c) 19nm diameter. Panel (d) shows the peak temperatures in the ZFC curves as a function of the nanoparticle sizes at 100mT.

However, the peak temperature in the ZFC magnetization shifts towards higher temperatures with the decrease in the nanoparticle size. This behavior is opposite to most of the antiferromagnetic nanoparticles. These discrepancies will be discussed in section 6, where all possible models are presented.

The peak temperatures of various sizes of MnO nanoparticles measured at different fields are listed in table 1. As can be seen, the peak temperatures for MnO nanoparticles with a diameter smaller than 20 nm are measured at ca. 20 K. These peak temperatures are lower than the N*é*el temperature of MnO. An unusual second peak appears in the ZFC magnetization of the 12nm diameter MnO nanoparticles at 5mT. It is a narrow peak with a sharp slope. At the same temperature of this unexpected peak, a deviation can be observed in the ZFC magnetization curve at 100mT. The unusual peak is probably due to the partial oxidation of the MnO nanoparticles [36, 37].

Magnetic field / Size of MnO nanoparticles	5mT	100mT	1T
6 nm	29.6K	28.6K	20.0K
12 nm	23.8K/36.8 K	23.6K	16.6K
19 nm	19.9K	19.9K	16.2K

Table 1: List of the peak temperatures in the ZFC magnetization curves for various sizes of MnO nanoparticles measured at different magnetic fields.

By measuring the magnetization as function of magnetic field, different magnetic structures can be distinguished. Diamagnetic materials exhibit a straight line with a negative slope. The magnetization curve of a paramagnet can be described by the Langevin function. Ferromagnetic materials show an opening in the magnetization hysteresis curve. The field dependence of the magnetization measured at different temperatures provide a good method to study the exchange bias effect on the interface between the antiferromagnetic and ferromagnetic materials. The exchange bias can be measured in a AF-FM core-shell system or a dimer nanoparticle composed by a AF nanoparticle and a FM nanoparticle.

The field dependent magnetization curves are measured on MnO nanoparticles of 6 nm, 12 nm, 19 nm diameter. The nanoparticles are initially cooled in a magnetic field of 100 mT to provide a reference direction. As can be seen in figure 28, hysteresis loops are observed at low temperature of 5 K. Such a feature is usual in an antiferromagnetic system. Due to a possible canting effect, the net magnetic moment of MnO nanoparticles trend to align along the magnetic field. The systems are not saturated even at an applied field of 5 T or 6 T. At high temperatures, the field dependences of magnetization show a linear behavior for 6 nm and 12 nm MnO nanoparticles as expected for an antiferromagnetic system. The hysteresis loop for

19 nm MnO nanoparticles gets narrow near zero magnetic field, which is usual for antiferromagnetic materials. At high temperatures at 100 K and 150 K, the MnO nanoparticles show paramagnetic behavior. This indicates, that the phase transition take places already below the Néel temperature of MnO at 120 K. This could agree with the peak temperatures measured in the ZFC magnetization curves.

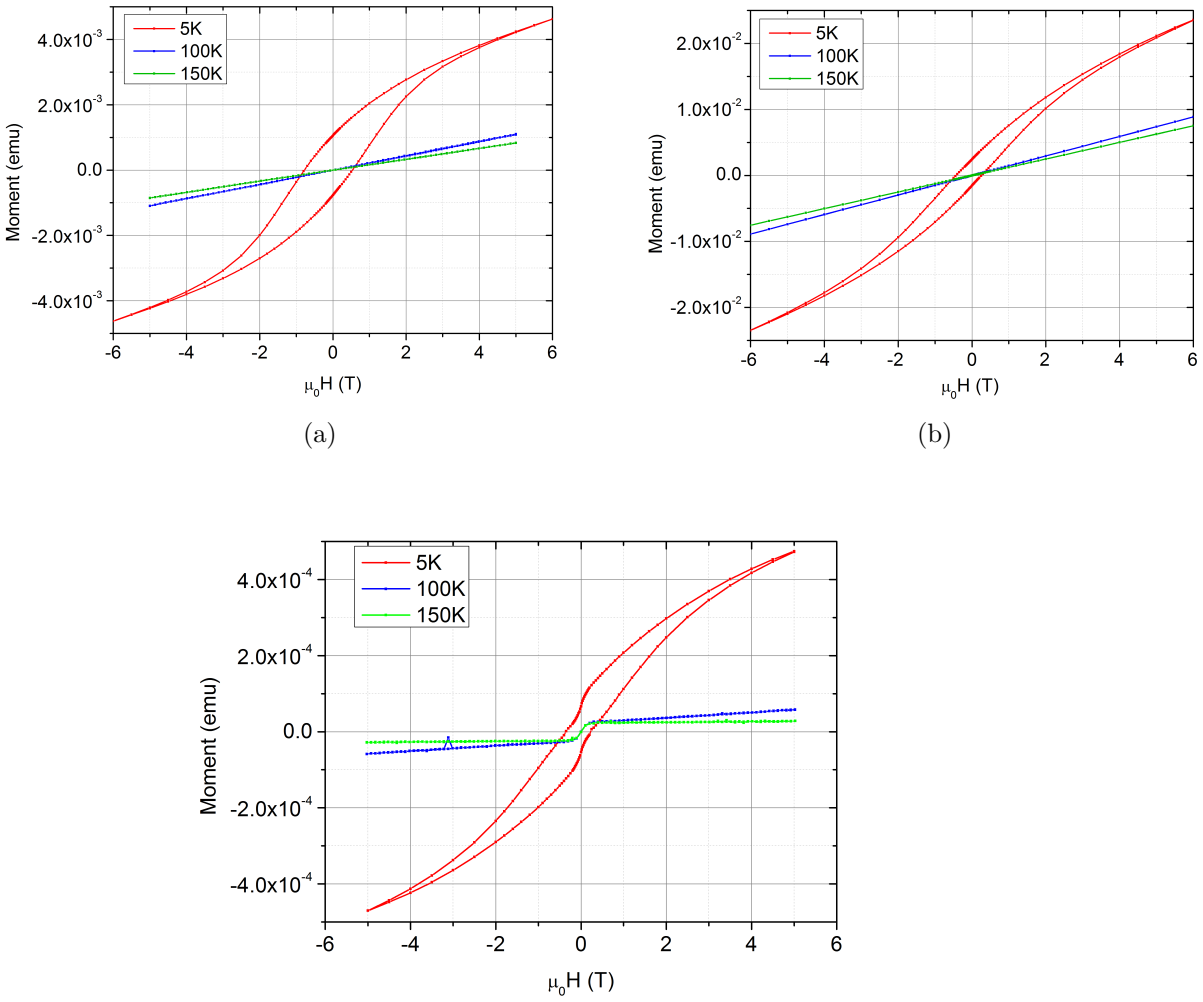

Figure 28: Hysteresis loops of MnO nanoparticles with (a) 6nm, (b) 12nm, and (c) 19nm diameter.

The exchange bias value of the system can be obtained by measuring the horizontal shift of the hysteresis loop from the origin, i.e. $H_{ex} = -\frac{1}{2}(|H_{c1}| - |H_{c2}|)$, where H_{c1} and H_{c2} are the positive and negative coercive fields obtained from the hysteresis loop, respectively. Figure 29 shows the hysteresis loops of 12 nm MnO nanoparticles at low temperatures. As the temperature increases, the hysteresis

loops become narrow because lower fields are needed to switch the magnetic moments. As can be seen in the inset, the centers of the hysteresis loops are shifted towards negative direction at low temperatures. This shift in the hysteresis loops of the MnO nanoparticles indicates an exchange bias effect.

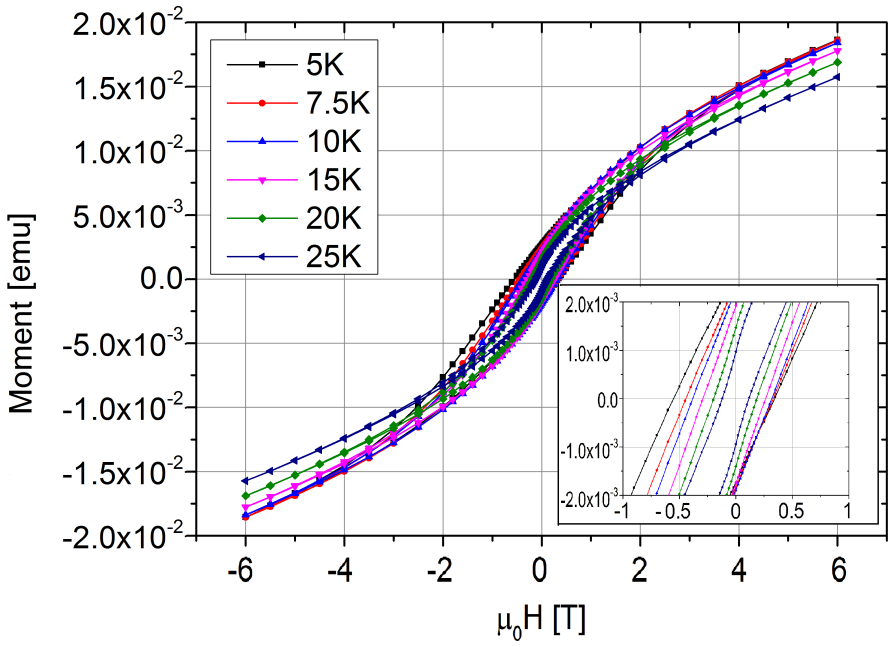

Figure 29: Hysteresis loops of 12 nm MnO nanoparticles measured at different temperatures. The inset shows an enlarged view of the hysteresis loops.

For a pure antiferromagnetic nanoparticle, exchange bias is not expected. The exchange bias effect measured in the MnO nanoparticles might be caused by the oxidation on the surface of the MnO nanoparticles. Due to the interaction between an antiferromagnetic MnO core and a ferrimagnetic Mn_3O_4 shell, an exchange bias effect is supposed to be found.

The positive and negative coercive fields H_{c1} and H_{c2} of 6 nm and 12 nm MnO nanoparticles are obtained from the hysteresis loops measured at different temperatures. The exchange bias fields H_{ex} as function of temperature are plotted in figure 30. For different sizes of MnO nanoparticles, exchange bias effect is observed. The $|H_{ex}|$ drops quickly from 5 K to 10 K, and decreases to zero around 20 K to 30 K. These temperatures match the peak temperatures measured in the ZFC magnetization curves. This fact might be fortuitous or specifically due to the magnetism in these systems, which is discussed below in section 6.

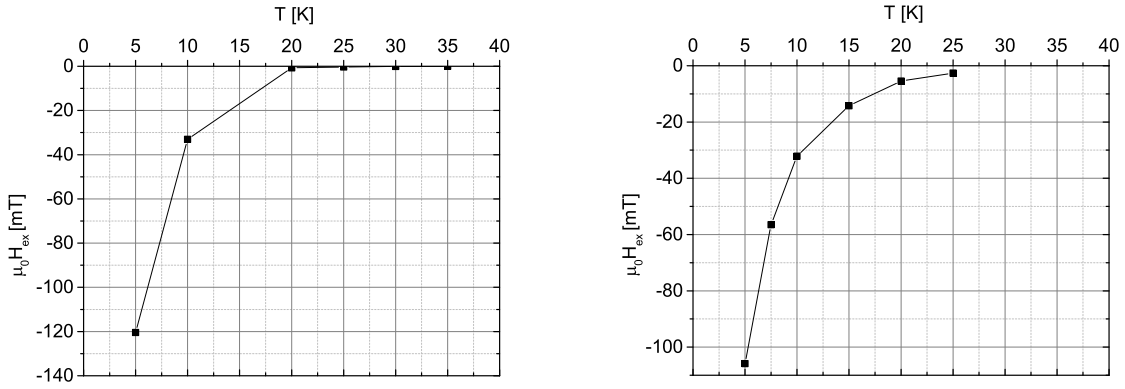

(a) (b)

Figure 30: Exchange bias field measured on MnO nanoparticles with (a) 6nm, (b) 12nm diameter.

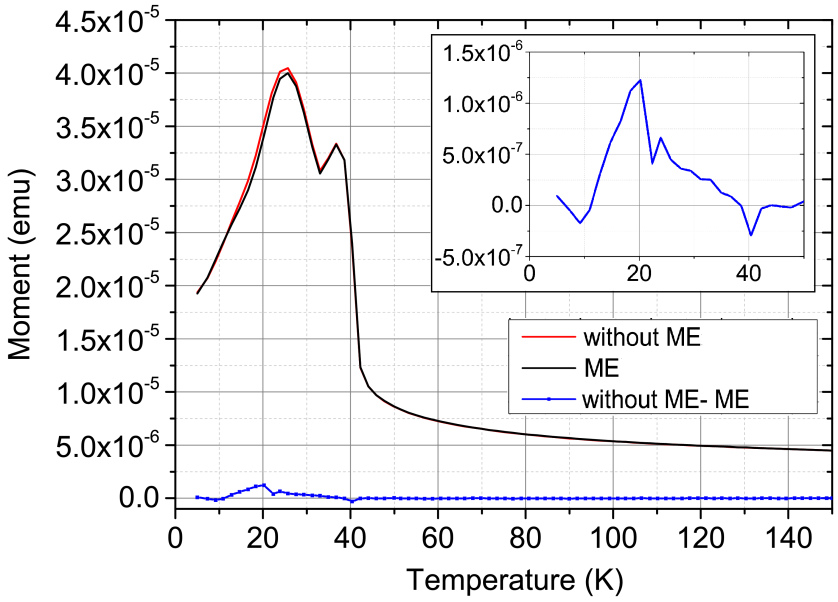

Figure 31: Memory effect of 12nm MnO nanoparticles. The red curve is a regular ZFC magnetization curve without stop, the black curve is the magnetization curve after a stop at 19K during cooling in zero field, the blue curve results from the subtraction of the red curve from the black curve. The inset shows an enlarged view near the stop temperature.

At a small magnetic field (5 mT), the magnetic memory effect of the MnO nanoparticles is measured. The sample is cooled in zero field to a certain temperature $T_{stop} < T_p$. After stopping the cooling procedure at T_{stop} for 10000 seconds, the sample continues being cooled to 5K. A magnetic field of 5mT is applied and the

magnetization is measured during heating up. A difference at T_{stop} between the ZFC curve with and without waiting at T_{stop} indicates a memory effect. The magnetic memory effect is only observed in spin glasses and superspin glasses [38]. Figure 31 shows the memory effect measured with 12 nm diameter MnO nanoparticles. It can be clearly seen, that a peak in the difference between the magnetization curves with and without memory effect appears at ca. 20 K. This peak agrees to the stop temperature of 19 K. For antiferromagnetic MnO nanoparticles, memory effect is not expected. The memory effect measured in the MnO nanoparticles is possibly caused by either a spin glass shell around the MnO core or collective superspin glass ordering between the close-packed MnO-nanoparticles on the substrate.

Since MnO is a complex system, Thermo Remanent Magnetization (TRM) and Isothermal Remanent Magnetization (IRM) are measured to be compared with different systems and to find a best model to describe its magnetic behaviors. In a TRM measurement, the system is cooled from a high temperature above the N*é*el temperature of MnO to 5 K in the presence of a magnetic field H. The magnetic field is turned off and the remanent magnetization of the sample is measured. The TRM magnetization is measured as a function of magnetic field H by cooling the sample at different magnetic fields.

In an IRM measurement the system is cooled from a high temperature above the N*é*el temperature of MnO to 5 K in the absence of a magnetic field. At 5 K, a magnetic field H is turned on and then turned off. The remanent magnetization of the system is measured. This procedure is repeated by turning on different magnetic fields after cooling in zero field every time. The remanent magnetization as a function of H is measured.

Figure 32 shows the TRM and IRM magnetizations of the various MnO nanoparticles. For a perfect antiferromagnet, both TRM and IRM magnetizations stays at zero. Unlike perfect antiferromagnets, MnO nanoparticles exhibit an increase in the magnetization in both TRM and IRM with the raise of the magnetic field. The magnetic moments in the TRM saturates at 3 T to 5 T, the IRM does not reach the maximum even at 5 T. This behavior cannot be explained by superparamagnetism. For a superparamagnetic system, TRM and IRM curves meet and reach the saturation already at several hundreds of millitesla [39]. For a spin glass, a peak in the TRM magnetization before the saturation is expected. This cannot be observed for the MnO nanoparticles, which is in conflict with the spin glass explanation. The TRM and IRM magnetizations measured for MnO nanoparticles have similar behavior with a DAFF (diluted antiferromagnet in a field) system [39].

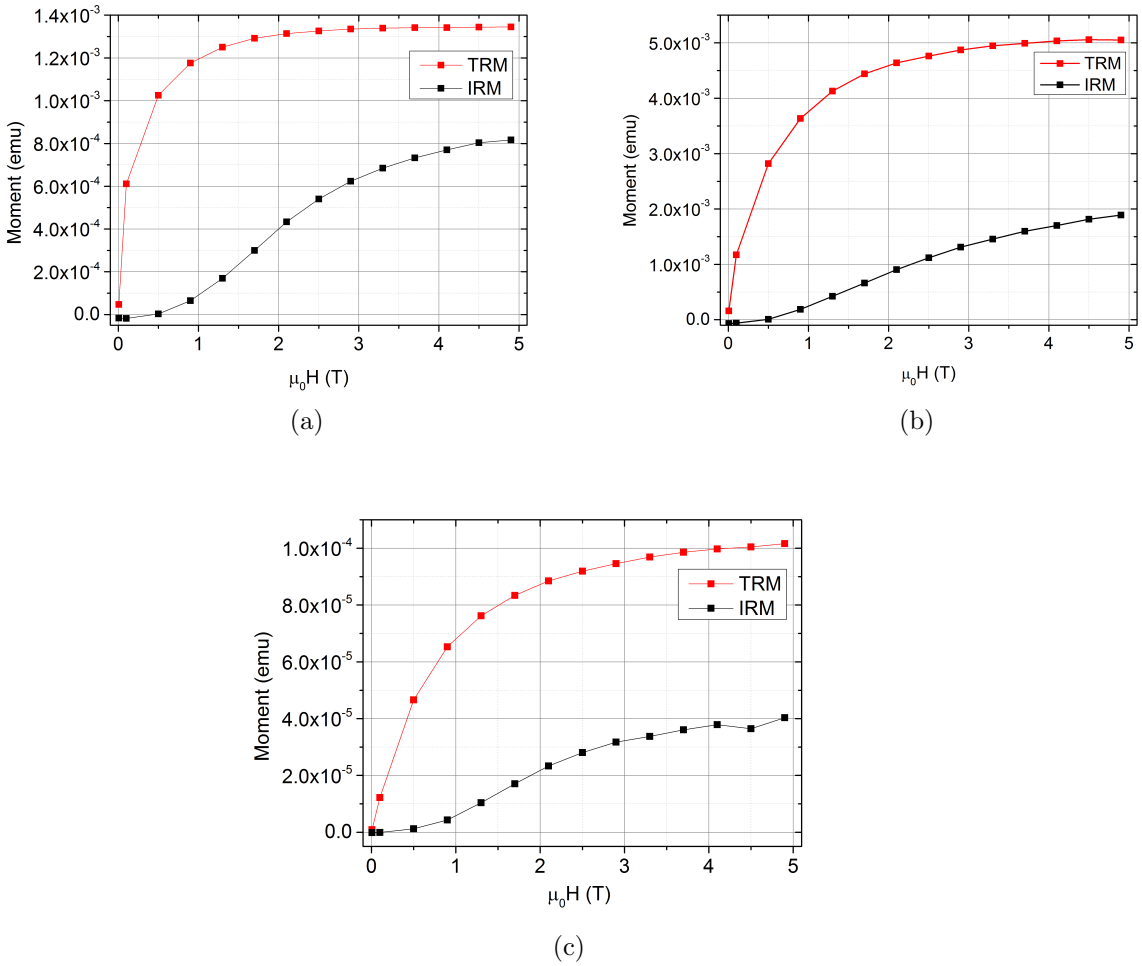

Figure 32: TRM and IRM magnetization curves measured on MnO nanoparticles with (a) 6nm, (b) 12nm and (c) 19nm diameter.

The second type of nanomaterial, i.e. FePt@MnO heterodimer nanoparticles were also investigated. The results are compared with the single MnO nanoparticles. Temperature and field dependent magnetization curves of FePt@MnO heterodimer nanoparticles as well as the exchange bias on the interface between the antiferromagnetic MnO nanoparticles and the ferromagnetic FePt nanoparticles are measured.

In figure 33, ZFC magnetization curves of two samples of FePt@MnO nanoparticles are displayed. The FePt nanoparticles in both heterodimer samples have the same size. The N*é*el temperature of MnO at 120 K cannot be observed in the ZFC curves of both FePt@MnO nanoparticles. At low temperatures, a peak can be observed in each ZFC magnetization curve of FePt@MnO heterodimer nanoparticles. This kind of peaks at low temperatures have also been observed in single MnO nanoparticles.

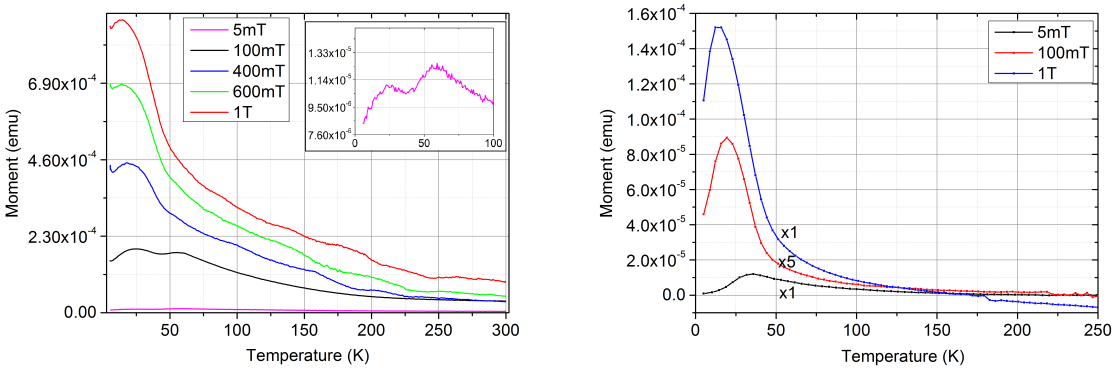

(a) (b)

Figure 33: ZFC magnetization curves of FePt@MnO heterodimer nanoparticles of (a) 5nm@10nm, (b) 5nm@14nm at various field. The inset in (a) shows an enlarged view of the ZFC magnetization curve of 5 mT at low temperatures.

As the magnetic field increases, the magnetic moments increases. For 5nm@10 nm FePt@MnO nanoparticles, two peaks can be observed at 5 mT and 100 mT. The second peak disappears above 400 mT. One of these peaks is likely to be caused by the single FePt nanoparticles. This is plausible, because in a synthesized FePt@MnO dispersion always a certain number of single FePt nanoparticles can be found according to TEM images from the collaborating group.

Figure 34 shows the ZFC and FC magnetization curves of FePt@MnO nanoparticles of various sizes. ZFC and FC curves of FePt@MnO nanoparticles show similar behavior with the single MnO nanoparticles. In all FePt@MnO samples, the ZFC magnetization curves show no feature at 120 K. At low temperatures, peaks are measured as expected from the MnO subunit of the FePt@MnO nanoparticles. ZFC and FC curves split at temperatures slightly higher than the peak temperatures. The peak temperature dependent on the magnetic field is as stable as before, which agrees with the results on single MnO nanoparticles. The peak temperatures of various sizes of FePt@MnO nanoparticles are listed in table 2. Two peaks in the ZFC magnetization curves of 5nm@14nm and 6nm@11nm FePt@MnO nanoparticles can be seen at 5 mT. At 1 T only one peak remains. The second peak is possibly due to single FePt nanoparticles. The peak temperatures of FePt@MnO nanoparticles are higher than single MnO nanoparticles with a similar size. This is possibly due to the exchange bias effect at the interface between the MnO nanoparticles and FePt nanoparticles. However, this effect is difficult to be distinguished from the exchange

bias effect *inside* each MnO subunit.

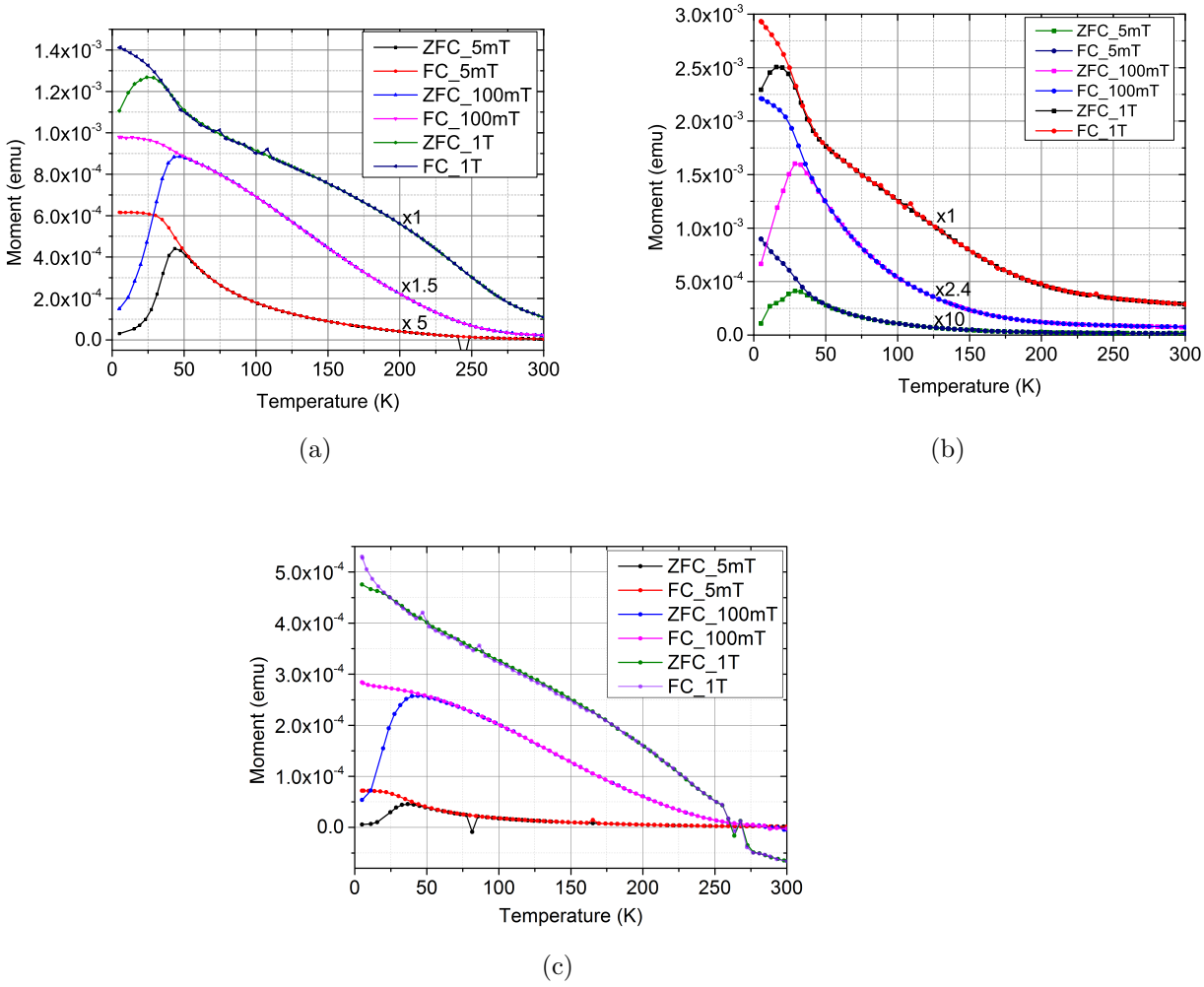

Figure 34: Temperature dependent magnetization curves of FePt@MnO nanoparticles with sizes (a) 5nm@12nm, (b) 6nm@11nm, (c)6nm@8-11nm.

FePt@MnO size \ Magnetic field	5mT	100mT	1T
5nm@10nm	37.1K	14.3K	19.4K
5nm@12nm	44K	46K	26K
5nm@14nm	26.7K/59.6K	25.6K/54.5K	15.0K
6nm@8-11nm	35K	40K	20K
6nm@11nm	12K/30K	29.8K	17.9K

Table 2: List of the peak temperatures for various sizes of FePt@MnO heterodimer nanoparticles measured at different magnetic fields.

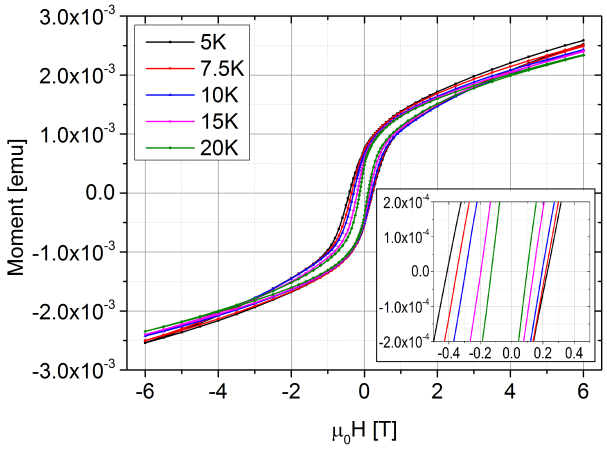

(a)

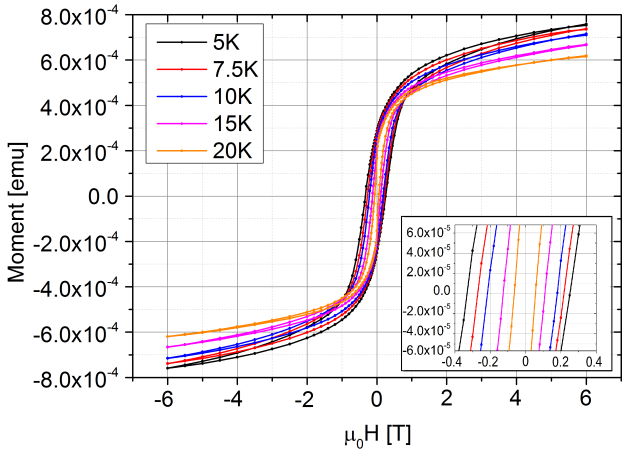

(b)

Figure 35: Hysteresis loops of FePt@MnO heterodimer nanoparticles with sizes (a) 5nm@12nm, (b) 6nm@8-11nm. Insets show enlarged views of the hysteresis loops around the origin.

Hysteresis loops of FePt@MnO nanoparticles are measured at different temperatures. Figure 35 exhibits hysteresis loops measured on various sizes of FePt@MnO nanoparticles. With the increase of the temperature the hysteresis loops become increasingly narrow. This is due to thermal fluctuations. A lower field is needed to switch the magnetic moments over the energy barriers. The hysteresis loops are slightly shifted from the origin. This indicates an exchange bias effect. At the interface between an antiferromagnet MnO nanoparticle and a ferromagnet nanoparticle, the exchange bias effect is in fact expected. For single MnO nanoparticles, the exchange bias effect has been measured as well. The exchange bias effect measured in the FePt@MnO nanoparticles is therefore due to an exchange bias effect inside

single MnO nanoparticles and the magnetic exchange interaction between the MnO and the FePt nanoparticles.

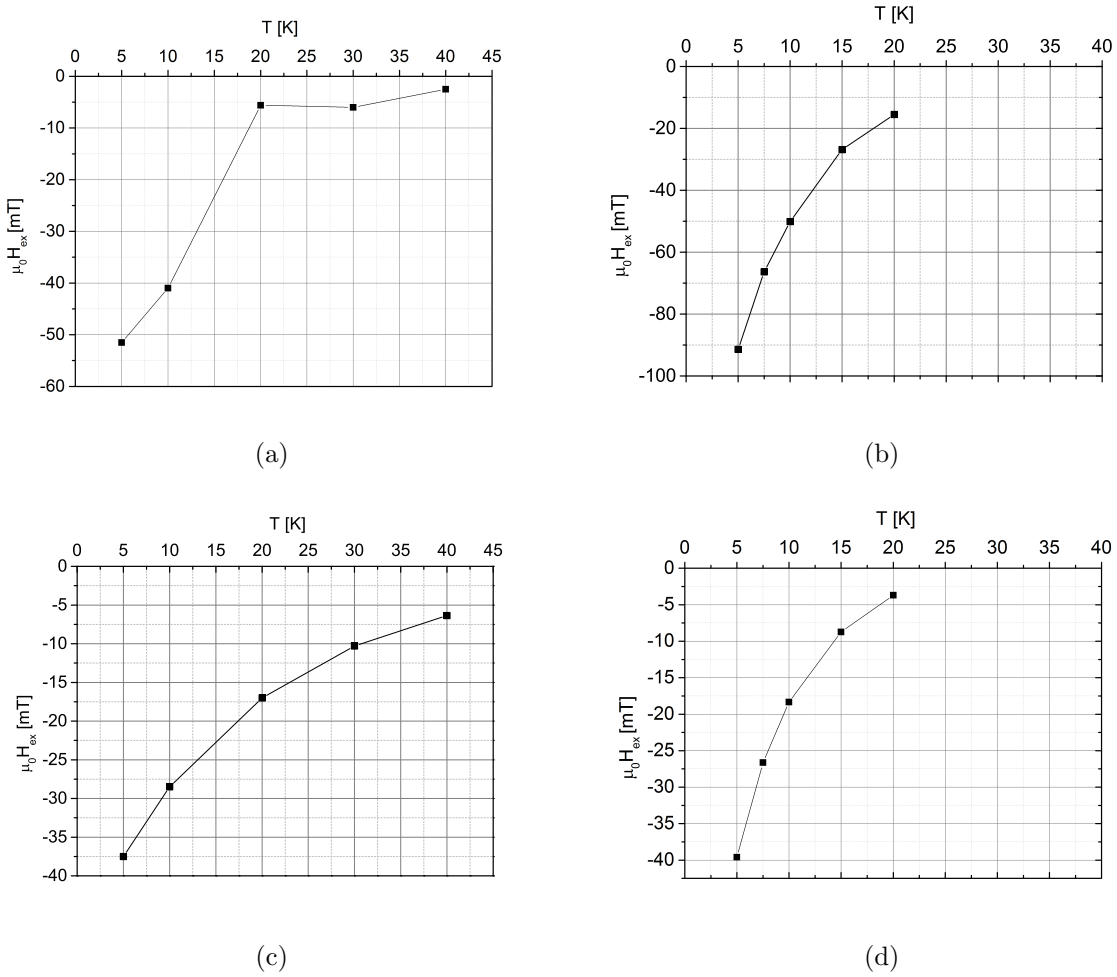

Figure 36: Exchange bias effect measured on FePt@MnO nanoparticles with sizes (a) 5nm@10nm, (b) 5nm@12nm, (c) 5nm@14nm, (d) 6nm@8-11nm.

The exchange bias fields dependent on the temperature are plotted in figure 36 for different sizes of FePt@MnO nanoparticles. The temperature dependence of the exchange bias field show similar behavior with the results of single MnO nanoparticles. The exchange bias fields decreases fast from 5 K to 20 K for the most samples. For 5nm@10nm FePt@MnO nanoparticles, the exchange bias field decreases to zero at 20 K - 30 K. The exchange bias effect measured for 5nm@14nm FePt@MnO has a weaker temperature dependence and persist until ca. 50 K. The FePt@MnO nanoparticles with 5nm@12nm and 6nm@8-11nm sizes show similar behavior.

This effect could correlate with the peaks in the ZFC curves, which show a maximum at very similar temperatures.

The exchange bias fields in FePt@MnO nanoparticles persist to higher temperatures compared to single MnO nanoparticles possibly due to the exchange interaction on the interface between the FePt and the MnO nanoparticles. Consequently, we can observe an exchange bias effect between the FePt and MnO subunits.

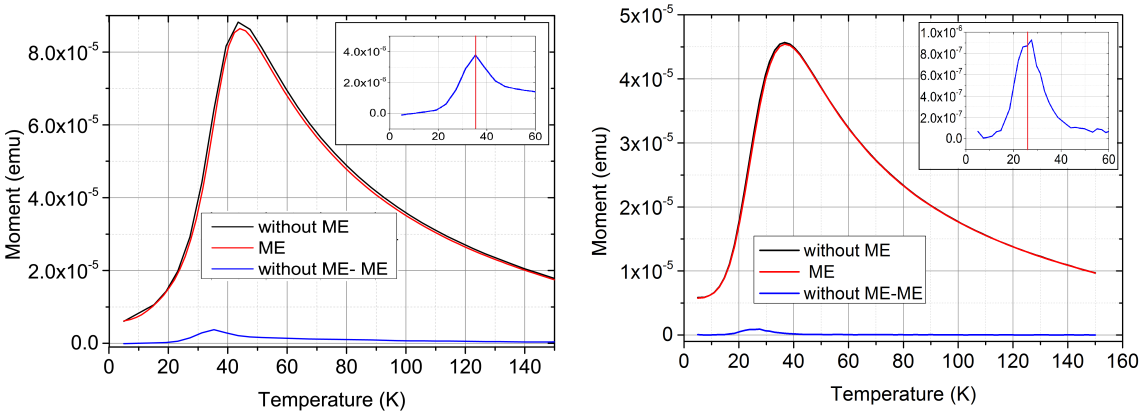

Figure 37: Memory effect of FePt@MnO nanoparticles with (a) 5nm@12nm, and (b) 6nm@8-11nm size. The red curve is the ZFC magnetization curve measured without stop, the black curve is the magnetization curve with a stop at (a) 36 K and (b) 25 K, the blue curve shows the difference between the red curve and the black curve. Inset shows an enlarged view of the difference near the stop temperature.

In FePt@MnO nanoparticles, also a memory effect is observed. Figure 37 displays the result of memory effect measurements on FePt@MnO nanoparticles with 5nm@12nm and 6nm@8-11nm size. Clear peaks can be seen near the stop temperatures in the difference between the ZFC curves and the magnetization curves with a stop at T_p. This peaks indicate the memory effect of the FePt@MnO nanoparticles. In single MnO nanoparticles, the memory effect has also been measured.

The TRM and IRM magnetizations are measured for different sizes of FePt@MnO nanoparticles. As can be seen in figure 38, the TRM and IRM magnetization curves of FePt@MnO nanoparticles show a similar behavior to the single MnO nanoparticles. They exhibit a structure between that of an antiferromagnet and a superparamagnet. As the size of the MnO nanoparticles in the heterodimer nanoparticles increased, the system is saturated at higher magnetic fields.

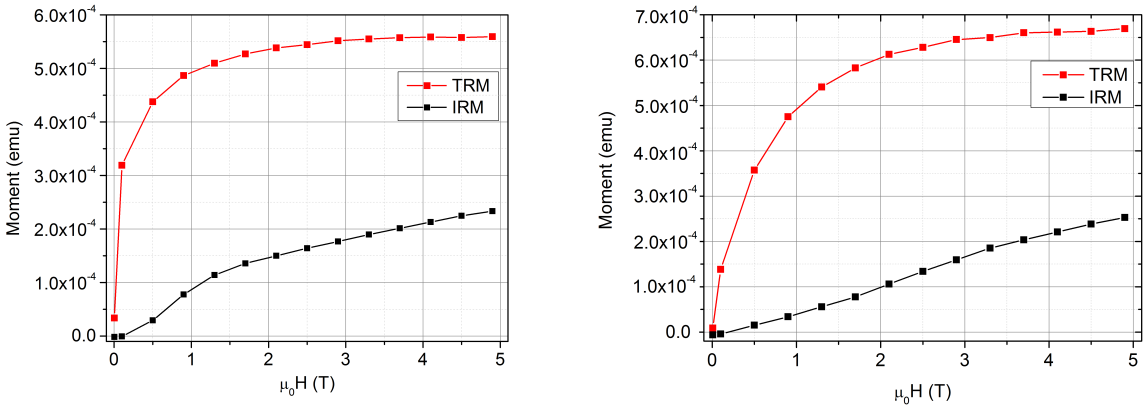

(a) (b)

Figure 38: TRM and IRM magnetizations curves measured on FePt@MnO nanoparticles with sizes (a) 5nm@10nm, (b) 5nm@14nm.

5.1.2 Neutron Scattering

Powder diffractions on 50 mg of single MnO nanoparticles of 12 nm size and 11 mg of FePt@MnO dimer nanoparticles with 6nm@8-11nm are performed using the DNS instrument with a neutron wavelength of 4.2 Å. Powder samples are wrapped in aluminum foil and placed in a cylindric sample holder. The intensity of the magnetic $(\frac{1}{2}\frac{1}{2}\frac{1}{2})$ Bragg peak and the nuclear (111) Bragg peak are measured above/below the peak temperature from the magnetomery measurements and above/below the Néel temperature of MnO. The temperature dependence of the magnetic Bragg peak reflects the antiferromagnetic order parameter of the MnO nanoparticles.

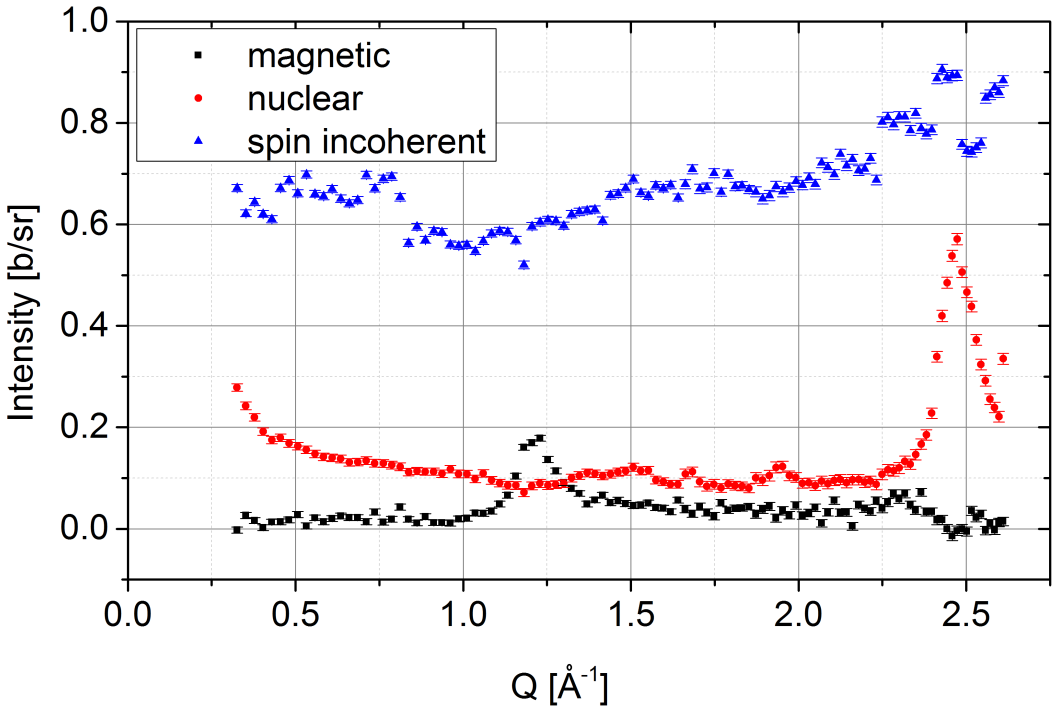

Figure 39: Nuclear coherent (red circles), spin-incoherent (blue triangles) and magnetic (black squares) components of the MnO nanoparticles at 4K.

Figure 39 shows the separated polarized neutron scattering of MnO nanoparticles with 12 nm diameter performed at the DNS-instrument. The blue triangles indicate the spin incoherent scattering, the red circles indicate the nuclear and isotope incoherent scattering, and the black squares indicate the magnetic scattering. The spin incoherent scattering can be seen as an almost flat line. As discussed in section 3, oleic acid is covered around the nanoparticles to avoid them to agglomerate. Oleic acid contains hydrogen, which produces spin incoherent scattering. Due to this, the spin incoherent scattering in the samples is high compared to the magnetic and

nuclear scattering. In the magnetic scattering, a peak is observed at Q = 1.2 Å^{-1}. This peak matches the magnetic $(\frac{1}{2}\frac{1}{2}\frac{1}{2})$ Bragg peak of MnO. The (111) nuclear Bragg peak of MnO can be seen at Q = 2.5 Å^{-1} as expected. Figure 40 shows the magnetic $(\frac{1}{2}\frac{1}{2}\frac{1}{2})$ Bragg peak of 12 nm MnO nanoparticles measured at different temperatures.

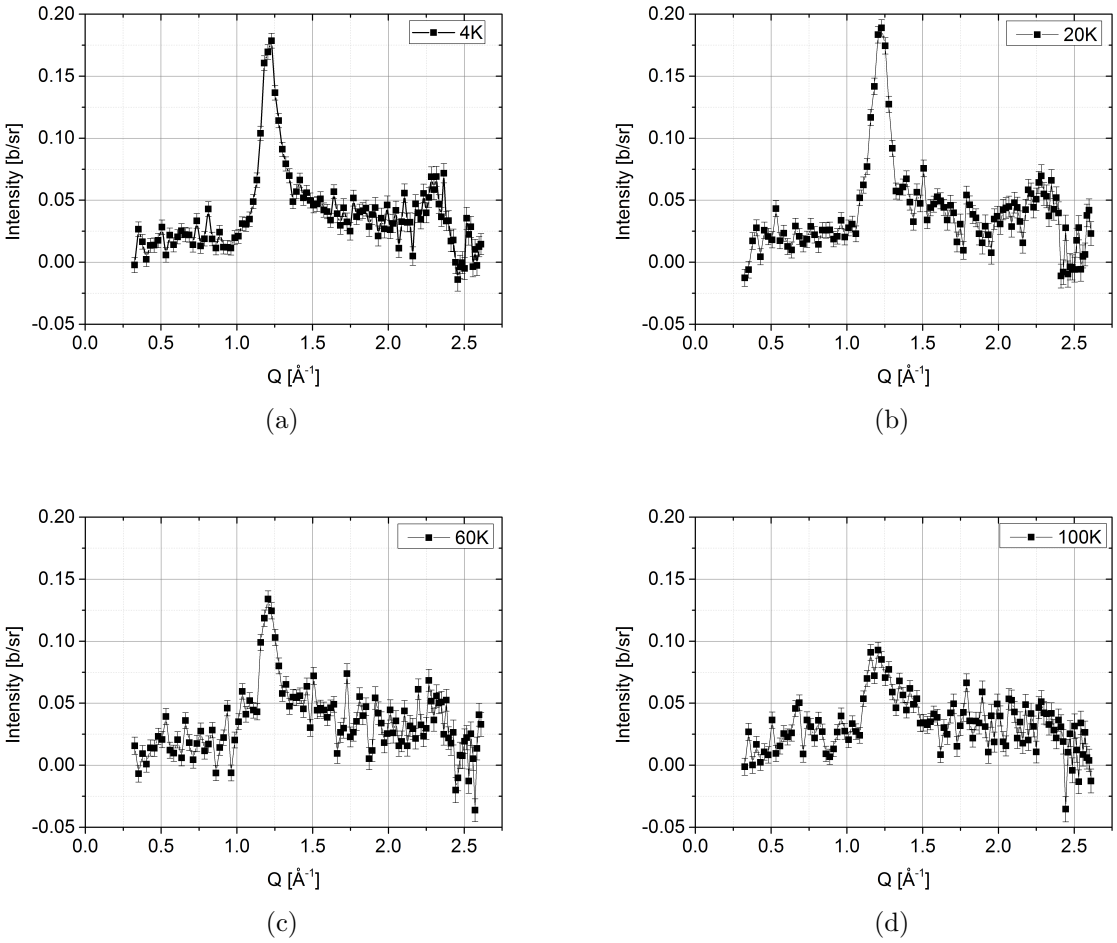

Figure 40: Magnetic scattering of 12nm MnO nanoparticles at (a) 4K, (b) 20K, (c) 60K, (d) 100K.

It can be seen, that the intensity of the magnetic peak stays unchanged within error bars below the peak temperature (ca. 23 K) as obtained from magnetometry. At 60 K, the intensity of the magnetic peak decreases. At 100 K, a weak and broad peak can be observed. Above the N*é*el temperature of MnO at 120 K, no magnetic peak can be seen (not shown). The magnetic peaks of the MnO nanoparticles are fitted with the pseudo Voigt function. The Full Width at Half Maximum (FWHM) of the Gauss fit for the bulk MnO is regarded as the instrumental resolution of the DNS instrument. It is inserted in a pseudo Voigt function as the Gauss width. The broadening of the magnetic peak due to the nanosize is described by the Lorentz

part of the pseudo Voigt function. The FWHM of the Lorentz part in the pseudo Voigt fits at various temperatures are recorded.

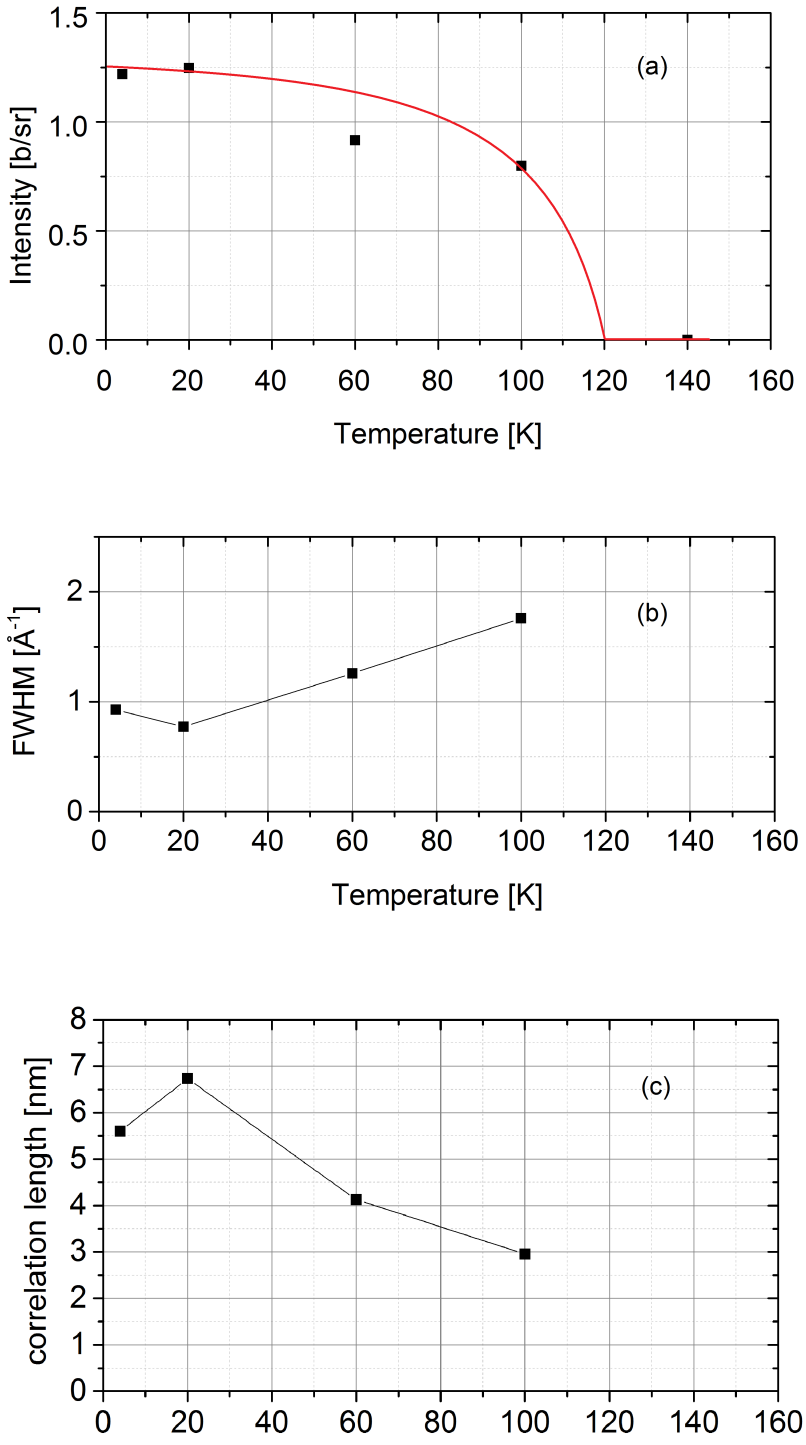

Figure 41: (a) The intensity of the magnetic scattering and (b) the Lorentz FWHM as function of temperature. (c) The correlation length as function of temperature. The black squares are the calculated data, the red curve is a guide line.

The intensity of the magnetic $(\frac{1}{2}\frac{1}{2}\frac{1}{2})$ Bragg peak (a) as well as the Lorentz FWHM (b) as function of the temperature are plotted in figure 41. The intensity of the magnetic peak decreases as the temperature is increased. The magnetic peak is expected to vanish near the N*é*el temperature at 120 K. This is confirmed by the DNS data. The correlation length ξ of the MnO nanoparticles is calculated with the Scherrer formula [40]:

$$\xi = \frac{K\lambda}{\beta cos\theta} \tag{5.1.1}$$

where K is the dimensionless shape factor, for spherical MnO nanoparticles with cubic symmetry, 0.94 is choosen as the K value, λ is the neutron wavelength, β is the broadening at the FWHM, θ is the Bragg angle. The correlation length dependent on the temperature is shown in figure 41(c). The correlation length of the nanoparticles decreases as expected with the increase of the temperature due to thermal fluctuations.

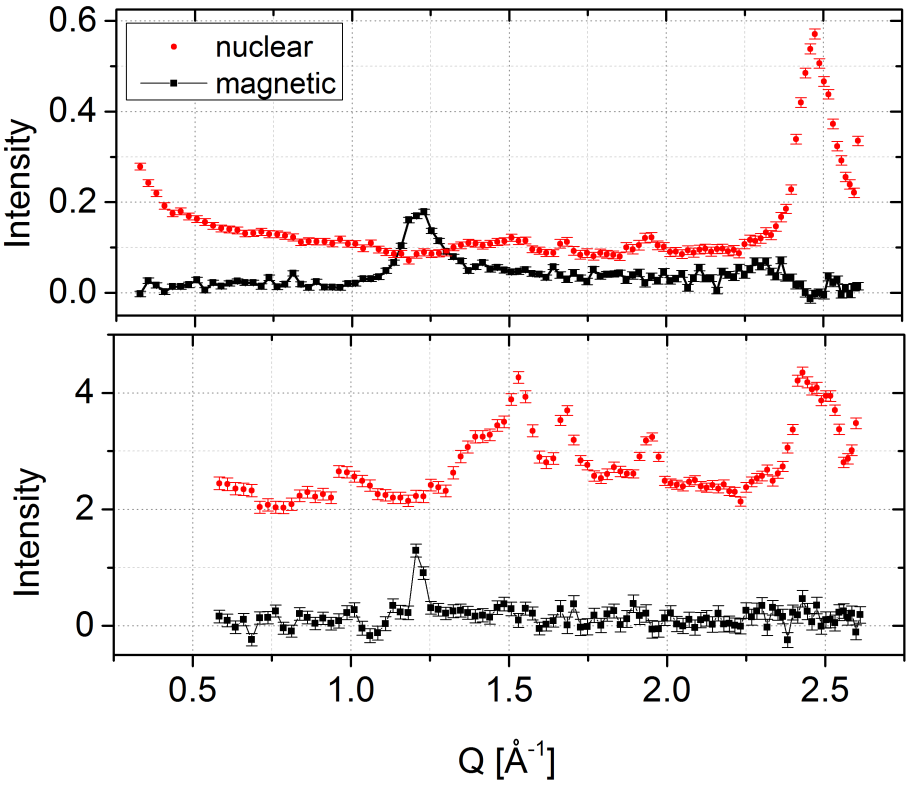

Figure 42: Comparison of the magnetic and nuclear scattering of 12nm MnO nanoparticles and 6nm@8-11nm FePt@MnO nanoparticles measured at 4K. The upper figure shows the polarized neutron scattering of MnO nanoparticles measured at DNS. The lower figure shows the separated scattering of FePt@MnO heterodimer nanoparticles measured at DNS.

The polarized neutron scattering of 11mg FePt@MnO heterodimer nanoparticles with 6nm@8-11nm size are measured at the DNS instrument. The saparated magnetic and nuclear scattering are compared with the data of the MnO nanoparticles in figure 42. A peak in the magnetic scattering of the FePt@MnO nanoparticles (lower figure) can be seen at Q = 1.24 $Å^{-1}$. This peak matches the magnetic $(\frac{1}{2}\frac{1}{2}\frac{1}{2})$ Bragg peak of MnO nanoparticles (upper figure). At the same Q value of the nuclear (111) peak of the MnO nanoparticles, a broad peak in the nuclear scattering of FePt@MnO is observed.

The peaks in the Q range from 1.5 $Å^{-1}$ to 2.0 $Å^{-1}$ in the nuclear scattering of FePt@MnO nanoparticles could match the nuclear data of the MnO nanoparticles. Due to the small amount of the sample, the magnetic scattering of the FePt@MnO nanoparticles is weak compared to the background. This make it difficult to make the correct separation in the polarization analysis. In the separated scattering of the FePt@MnO nanoparticles, only two data points at the magnetic peak are observed. The correct correlation length of the FePt@MnO nanoparticles is not possible to be calculated from the FWHM of a magnetic peak with two data points.

Also at the D7 instrument in ILL, four FePt@MnO dimer nanoparticle samples with ca. 10mg each sample are measured to investigate the spin structure in the FePt@MnO dimer nanoparticles and to be compared with single MnO nanoparticles. The FePt nanoparticles are 5-6nm, and the sizes of MnO nanoparticles vary from 8nm to 16nm. The four samples were dried separately on Aluminum foil. The Aluminum foils are folded like a ring of 2cm diameter and 1.0 - 1.5cm height. The samples are marked and put into the sample holder at different height. The FePt@MnO dimer nanoparticles were measured at 4K, 20K, 60K, 100K and 140K. Polarized cold neutrons with a wavelength of 4.86 Å are used for the measurements. The data analysis of D7 is done by software LAMP (Large Array Manipulation Package) written at the ILL.

Figure 43 shows the separated neutron scattering measured at D7. The error bars are relatively large because of the small amount of the sample. The spin incoherent scattering exhibits a nearly straight line, which indicates the successful separation of different components. At Q = 1.2 $Å^{-1}$ and in the Q range from 1.5 $Å^{-1}$ to 2.0 $Å^{-1}$, several narrow peaks can be seen in the spin incoherent scattering, and at the corresponding Q, dips are observed in the magnetic scattering. They are due to the error calculations in the polarization analysis and are not considered to be from the sample. At Q = 1.25 $Å^{-1}$, a weak magnetic Bragg peak can be observed. This magnetic peak matches the magnetic $(\frac{1}{2}\frac{1}{2}\frac{1}{2})$ Bragg peak of the MnO nanoparticles. The

nuclear (111) peak of MnO is expected at Q = 2.5 Å^{-1}. Because of the limitation of the Q range, only an increase at Q = 2.5 Å^{-1} is observed in the nuclear scattering of FePt@MnO nanoparticles.

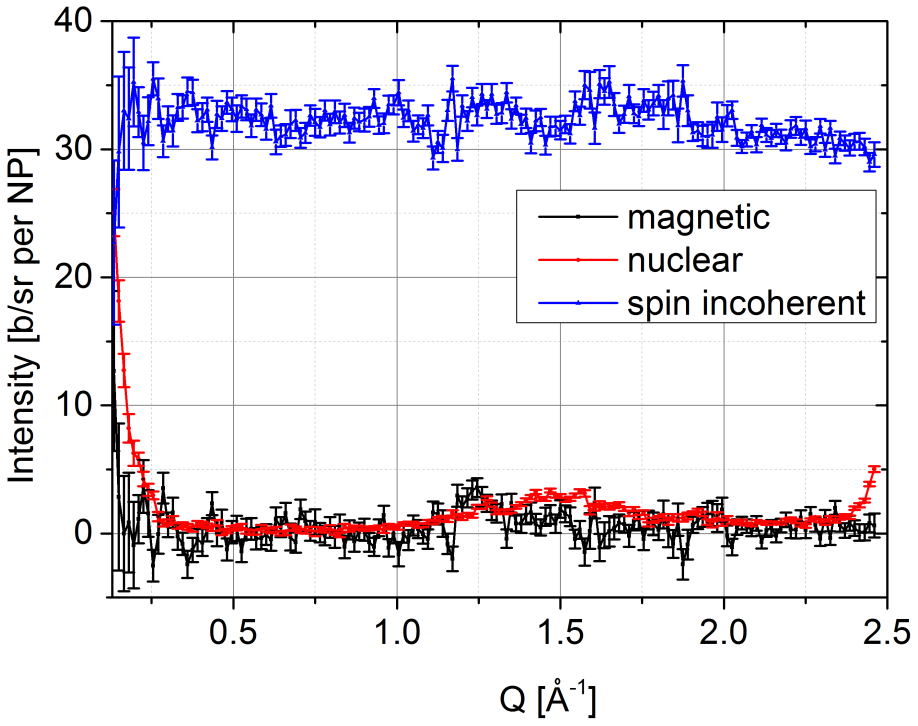

Figure 43: Nuclear coherent (red), spin-incoherent (blue) and magnetic (black) components of the D7 polarized neutron scattering for FePt@MnO heterodimer nanoparticles at 4K.

In figure 44, the magnetic and nuclear scattering of the FePt@MnO heterodimer nanoparticles measured at D7 are compared with the results of the MnO nanoparticles at DNS. As can be seen in both magnetic scattering of MnO nanoparticles (upper) and FePt@MnO nanoparticles (lower), a clear peak appears at Q = 1.24 Å^{-1}. This magnetic $(\frac{1}{2}\frac{1}{2}\frac{1}{2})$ Bragg peak confirms the significant influence of the MnO nanoparticles on the magnetic properties FePt@MnO nanoparticles. At Q = 2.5 Å^{-1}, the increase in the nuclear scattering of FePt@MnO matches the nuclear (111) peak of the MnO nanoparticles. In the Q range of 1.4 Å^{-1} -2.0 Å^{-1}, several peaks in the nuclear scattering of FePt@MnO nanoparticles can be observed. They are probably a result from the MnO nanoparticles, which can also be found in the nuclear scattering of single MnO nanoparticles. This result indicates, that the antiferromagnetic ordering of MnO nanoparticles is not destroyed by the FePt nanoparticles.

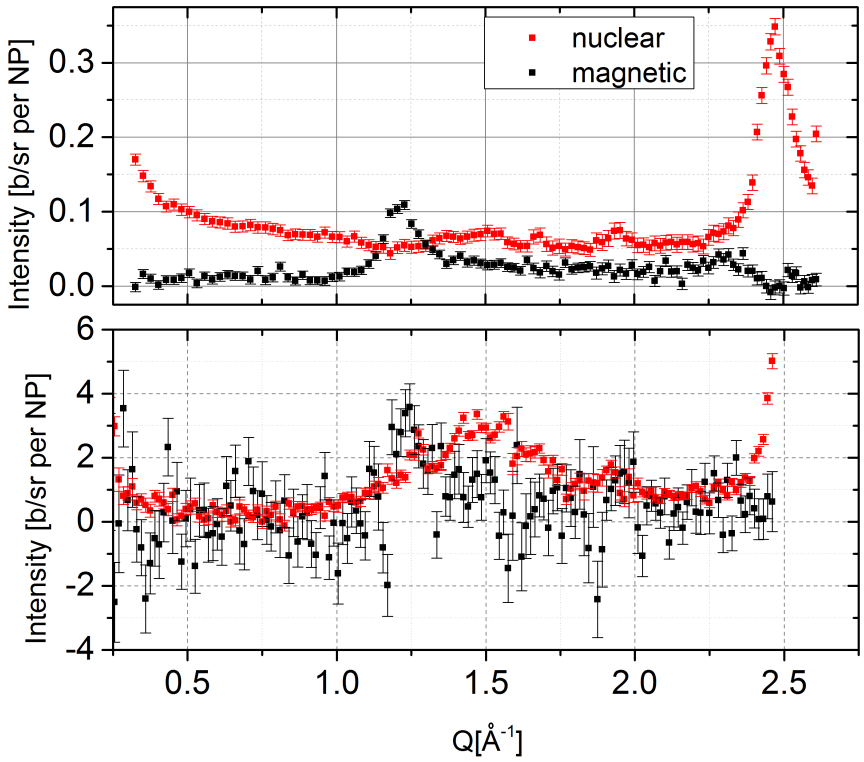

Figure 44: Comparison of the separated neutron scattering of MnO nanoparticles and the FePt@MnO nanoparticles at 4K. The upper figure shows the polarized neutron scattering of MnO nanoparticles measured at DNS. The lower figure shows the separated scattering of FePt@MnO heterodimer nanoparticles measured at D7.

Figure 45 shows the magnetic $(\frac{1}{2}\frac{1}{2}\frac{1}{2})$ Bragg peak of FePt@MnO nanoparticles measured at different temperatures. The black squares with error bars are the experimental data, the red curves are the Gauss fits for the $(\frac{1}{2}\frac{1}{2}\frac{1}{2})$ Bragg peaks. The intensity of the magnetic Bragg peaks have about the same amplitude from 4 K to 60 K. At 100 K, the intensity is obviously decreased. Above the Néel temperature of MnO at 120 K, no magnetic peak can be observed (data not shown). The temperature dependence of the peak intensity indicates the order parameter of the FePt@MnO nanoparticles. Because of the resolution of the D7 instrument, the correlation length of FePt@MnO nanoparticles cannot be calculated using the FWHM of the Gauss fits.

The intensity of the magnetic $(\frac{1}{2}\frac{1}{2}\frac{1}{2})$ Bragg peak for the FePt@MnO nanoparticles dependent on the temperature is shown in figure 46. As can be seen, the magnetic $(\frac{1}{2}\frac{1}{2}\frac{1}{2})$ Bragg peak vanishes between 100 K and 140 K. This result is similar to the order parameter curve measured for single MnO nanoparticles at the DNS instrument. The FePt subunit in the FePt@MnO heterodimers has no obvious influence onto the antiferromagnetic order parameter of MnO nanoparticles.

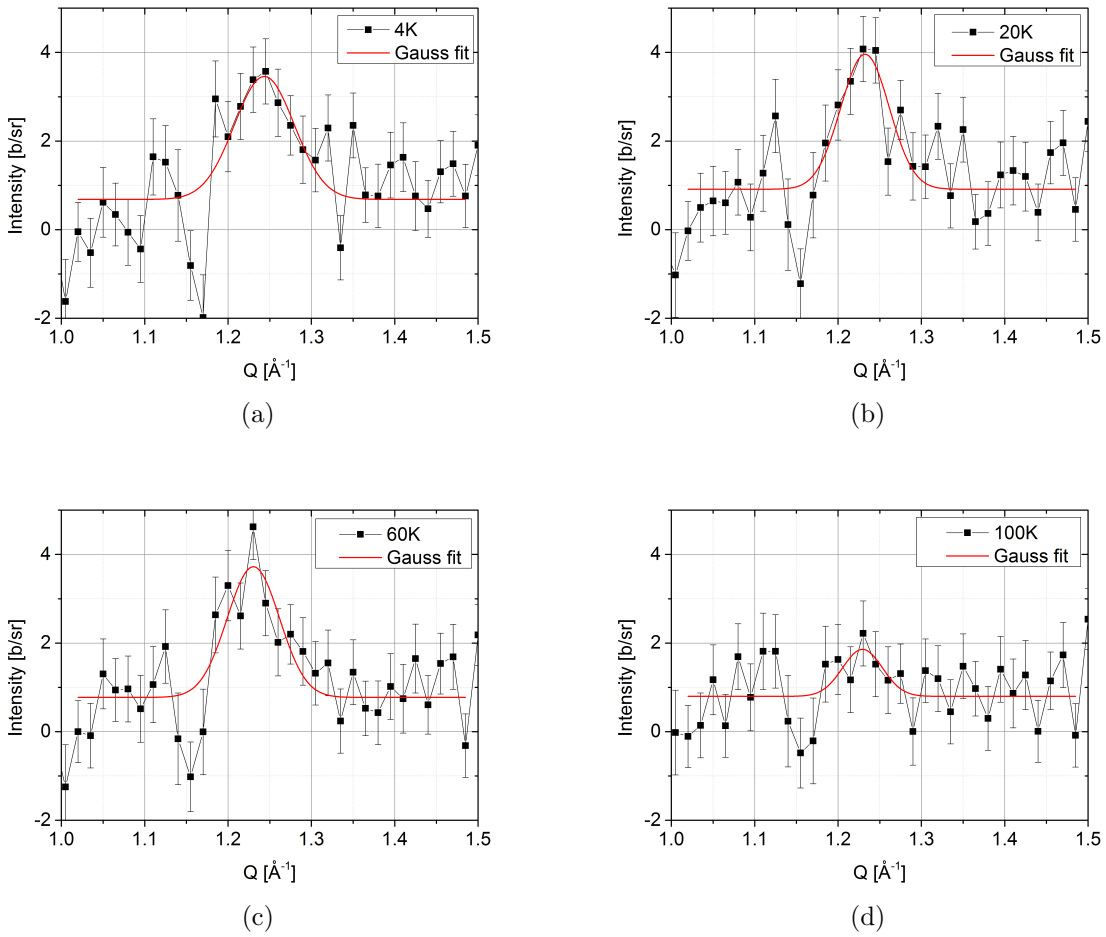

Figure 45: Magnetic scattering around the $(\frac{1}{2}\frac{1}{2}\frac{1}{2})$ Bragg position of FePt@MnO nanoparticles at (a) 4K, (b) 20K, (c) 60K, (d) 100K measured at the D7 instrument.

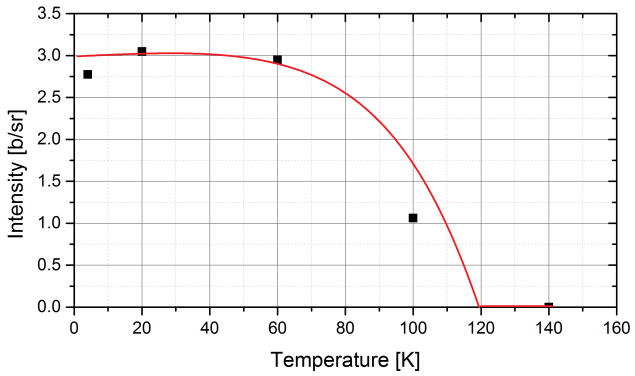

Figure 46: The intensity of magnetic scattering of FePt@MnO nanoparticles as function of temperature. The black squares represent the amplitude of the intensity obtained from the Gauss fit, the red curve is only a guide to the eye.

5.2 Simulations

With the Monte-Carlo method, two sizes of nanoparticles composed of 10×10×10 and 20×20×20 unit cells of MnO are simulated. The nanoparticles are modeled in cubic and spherical form. In order to compare with the well-known results of bulk MnO, simulations of the MnO nanoparticles with periodic boundary condition are performed.

ZFC and FC magnetization curves of MnO nanoarticles are simulated and compared with the experimental data. Figure 47 shows the ZFC and FC magnetization curves for a cubic 10×10×10 MnO nanoparticle simulated at different magnetic fields.

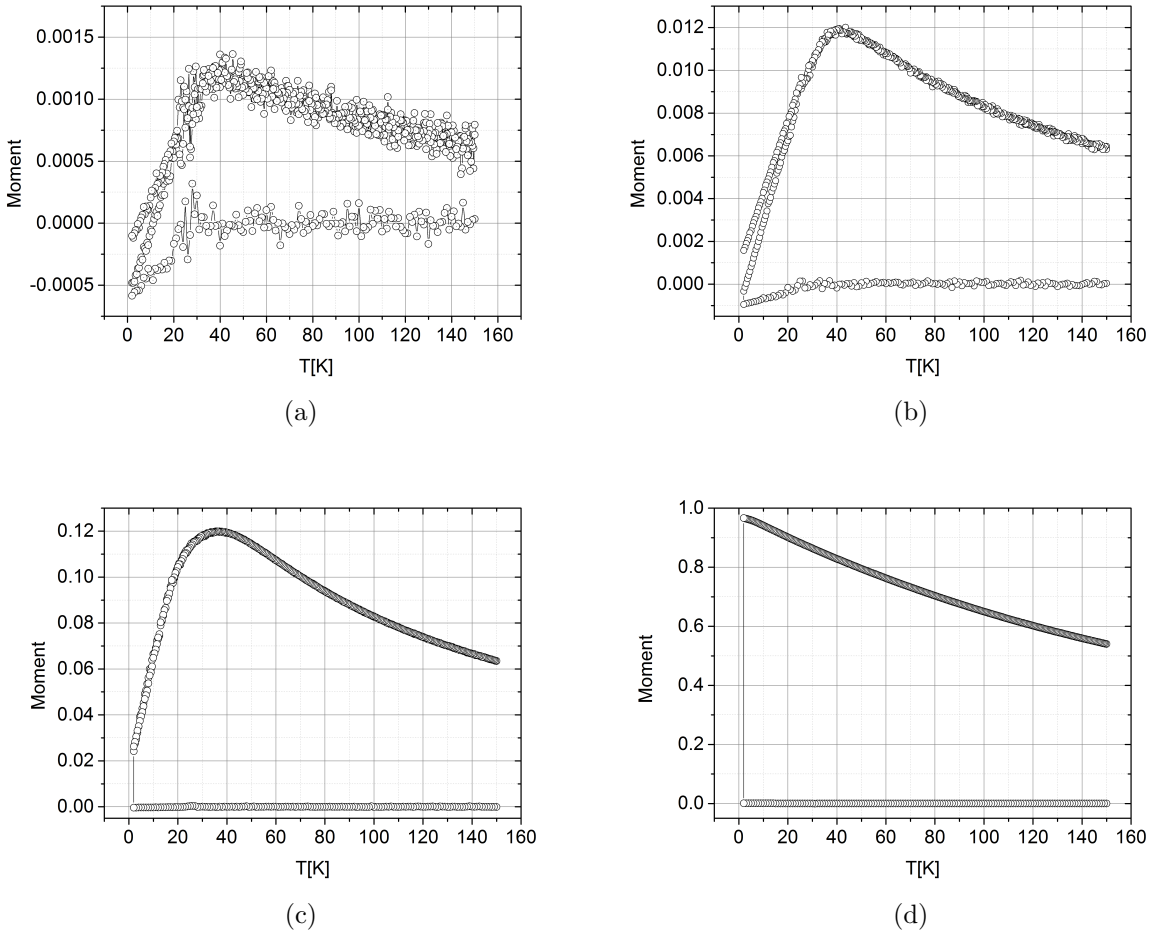

Figure 47: Monte Carlo simulations of the ZFC and FC curves for 10×10×10 MnO nanoparticles at (a) 100 mT, (b) 1 T, (c) 10 T, (d) 100 T with cubic shape.

Each magnetization curve represents three procedures. The system is first cooled in zero magnetic field. During this procedure, the magnetic moments in the nanoparticle are frozen in random states, and a straight line in the total magnetization at zero can be observed. The magnetic moments simulated are normalized to the saturation magnetic moments. At 5 K, a magnetic field is applied, the ZFC magnetization curve for the system is simulated. At the same magnetic field, the FC procedure is simulated. In the simulations with the magnetic field until 10 T, both ZFC and FC curves show a broad peak at 30 K - 40 K. At 100 T, the peak cannot be observed. The magnetic ordering is not completely destroyed at 150 K. Near the MnO N*é*el temperature at 120 K, no information can be found in all magnetization curves. The peak temperature shifts slightly towards low temperature with the increase of the magnetic field. At 10 T and 100 T, no splitting can be seen between the ZFC and FC curves as expected for an antiferromagnet. At 100 mT and 1 T, the ZFC and FC magnetization curves are slightly splitted below the peak temperatures. This split has also been observed in the experimental results, which might be caused by the presence of antiferromagnetic domain walls. As can be seen in figure 47, the total magnetic moment of the system increases as the magnetic field increases. At 5 mT, the magnetic moment is too small to be separated from the noise.

In the simulatins of the field dependence of the magnetizations, no hysteresis loops can be observed as one expects for an antiferromagnet (figure 48). At 5 K, the field dependent magnetization exhibits a slight bending. At 100 K and 150 K, the magnetizations as function of magnetic field show straight lines with positive slopes as expected for an antiferromagnetic system. As the temperature increases, the slope of the line decreases. The total magnetic moment at 5 K is smaller than at higher temperatures, because the magnetic moments are frozen in random states during the zero field cooled procedure. The field dependent magnetization curve simulated at 5 K is shifted upwards. This is probably due to the net magnetic moment inside antiferromagnetic domain walls, which has also caused the splitting between the ZFC and FC magnetization curves.

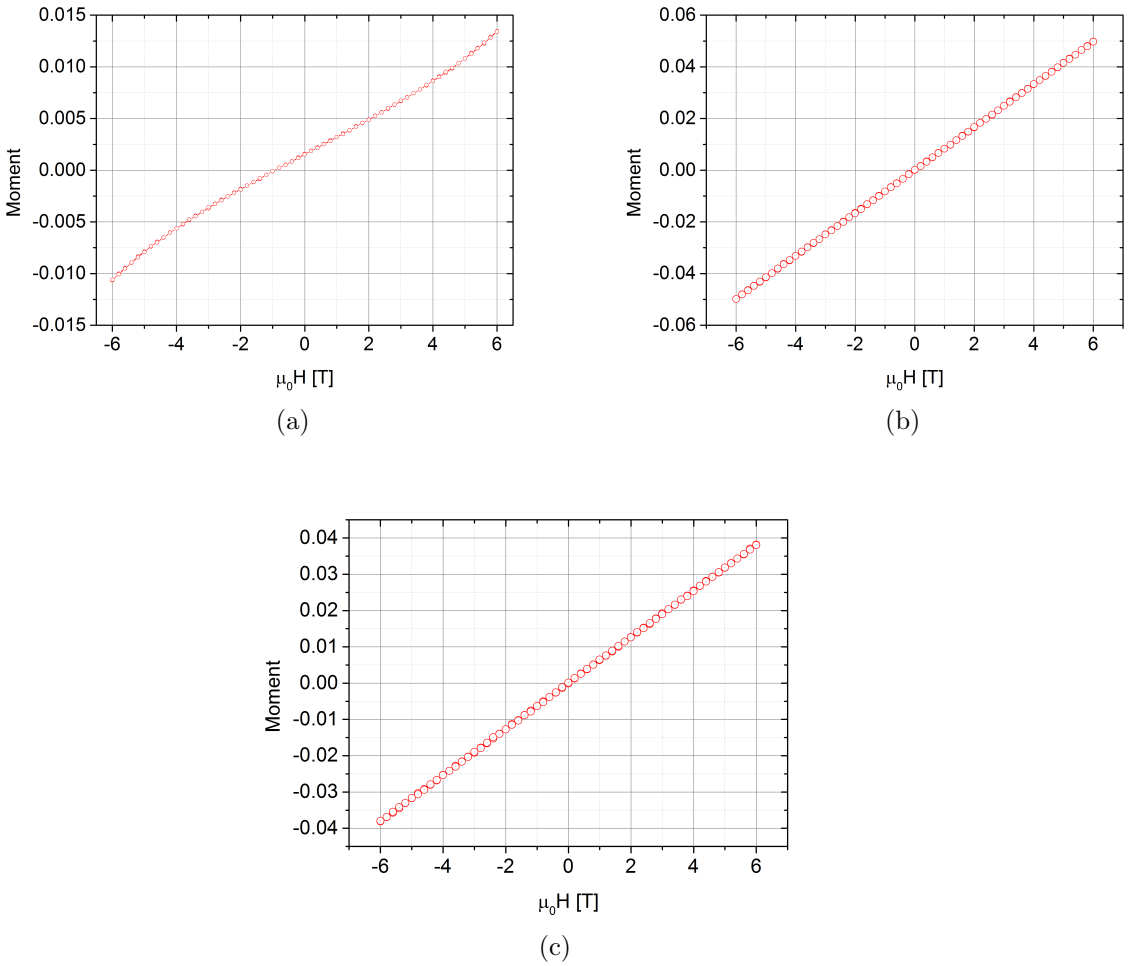

Figure 48: Monte Carlo simulations of the field dependence of the magnetic moment for 10×10×10 MnO nanoparticles at (a) 5 K, (b) 100 K, (c) 150 K with cubic shape.

Cubic nanoparticles containing 20×20×20 MnO are simulated to study the temperature and field dependence of the magnetization. In figure 49, ZFC and FC magnetization curves of 20×20×20 MnO nanoparticles simulated at various fields are illustrated. Below 10 T, clear peaks are observed in the ZFC and FC magnetization curves. The peak temperature stays at ca. 55 K until 10 T. At 100 T, a hump near 20 K can be seen. This is supposed to be the previous peak with a large decrease in the peak temperature.

The peak temperatures for the 20×20×20 MnO nanoparticle are higher than that of the 10×10×10 MnO nanoparticle. This phenomenon is as one would expect for a regular antiferromagnet showing a finite size effect, however opposite to the magnetometry results. Compared to the 10×10×10 MnO nanoparticle, the peaks in the ZFC and FC magnetization curves are sharper for the 20×20×20 MnO nanopar-

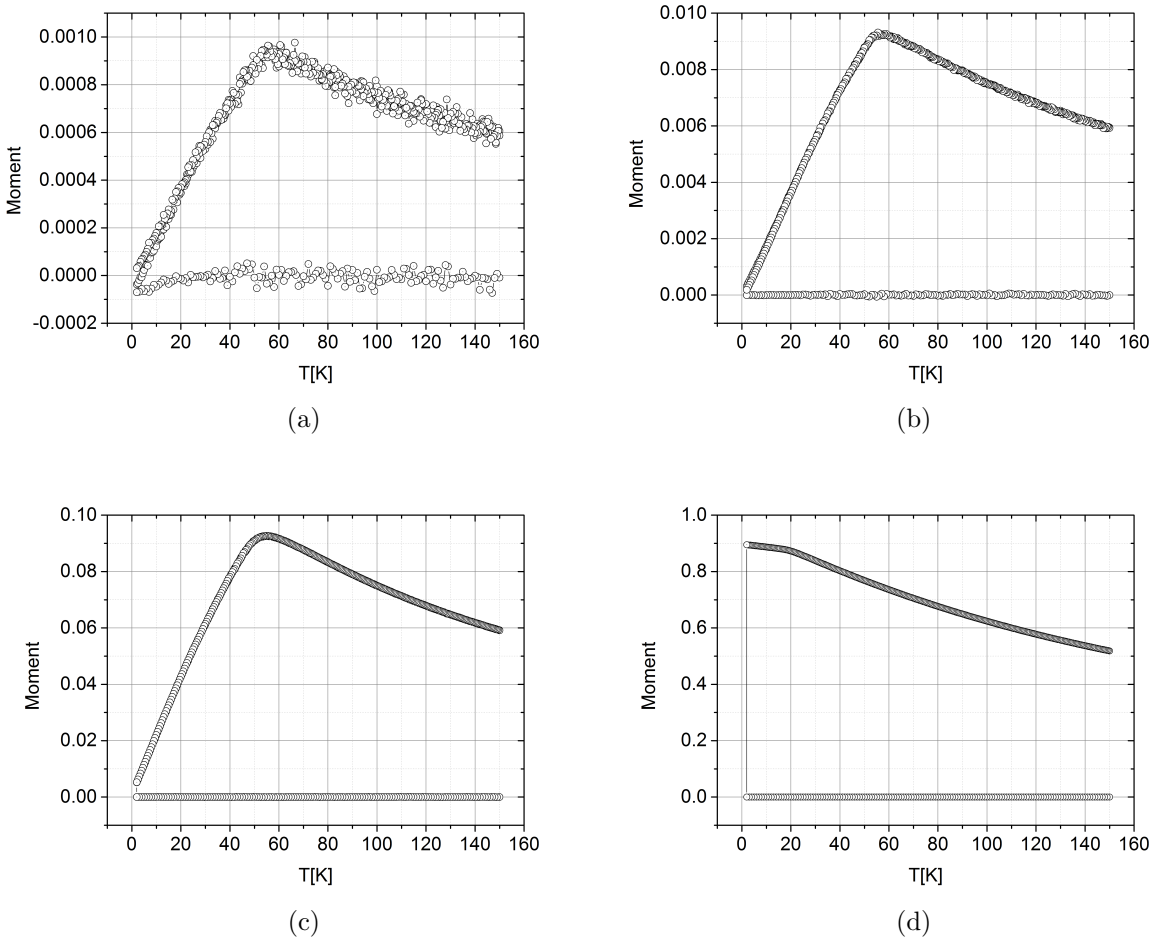

Figure 49: Monte Carlo simulations of the ZFC and FC curves for 20×20×20 MnO nanoparticles at (a) 100 mT, (b) 1 T, (c) 10 T, (d) 100 T in cubic shape.

ticle. At 100 mT, a slight splitting between the ZFC and FC curves can be seen. Above 1 T, the ZFC and FC curves show no splitting. This can again be explained by the presence of antiferromagnetic domain walls, which is weak compared to the magnetic moments of MnO nanoparticles at high fields.

The field dependence of the magnetic moment for a 20×20×20 MnO nanoparticle have a similar behavior to the 10×10×10 MnO nanoparticle. The field dependent magnetization shows a slight deviation from linearity at 5 K. At higher temperatures of 100 K and 150 K, the magnetic moment increases proportionally to the applied magnetic field. This behavior is usual for an antiferromagnetic system. The slope of the magnetization curve decreases with an increase in the temperature. The total magnetic moment at 5 K is much smaller than that at 100 K and 150 K, which can also be seen in the ZFC and FC magnetization curves. For a 20×20×20 MnO

nanoparticle, no obvious shift of the magnetization curve is found as has been seen in the simulation of 10×10×10 MnO nanoparticle at 5 K. The net magnetic moment due to the domain walls has less influence in a larger system.

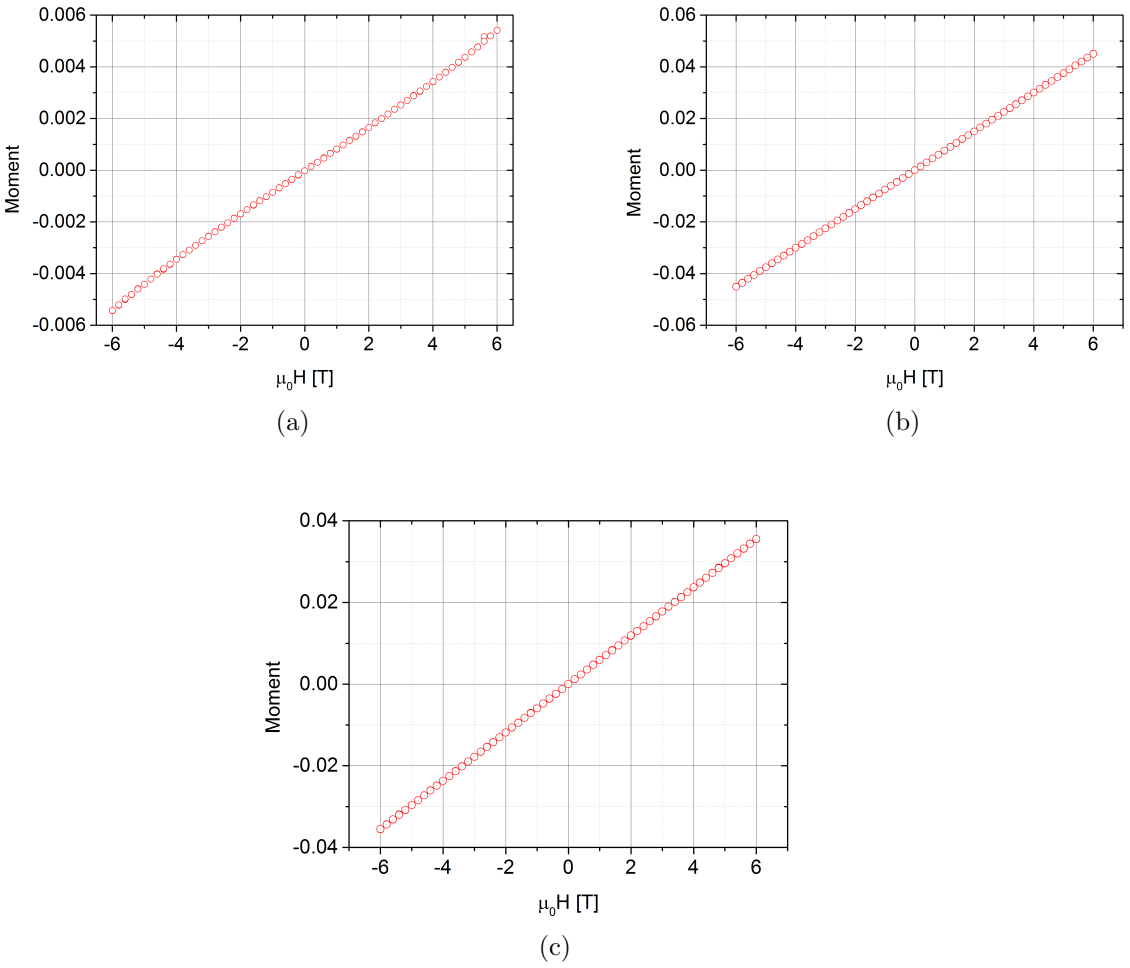

Figure 50: Monte Carlo simulations of the field dependence of the magnetic moment for 20×20×20 MnO nanoparticles at (a) 5 K, (b) 100 K, (c) 150 K in cubic shape.

In order to compare the simulation results better with the experimental data, spherical nanoparticles are modeled. Figure 51 shows several ZFC and FC magnetization curves for different sizes of spherical MnO nanoparticles. It can be seen, the peak temperatures in the magnetic curves of spherical nanoparticles stay unchanged compared with the cubic nanoparticles of the same size at the same field. The magnetic moment at the peak temperature and the behavior of the magnetization curves above the peak temperatures are identical for cubic and spherical nanoparticles. The splitting between the FC and ZFC magnetization curves are slightly different between cubic and spherical nanoparticles. This might be caused

by the net magnetic moments due to the uncompensated surface spins.

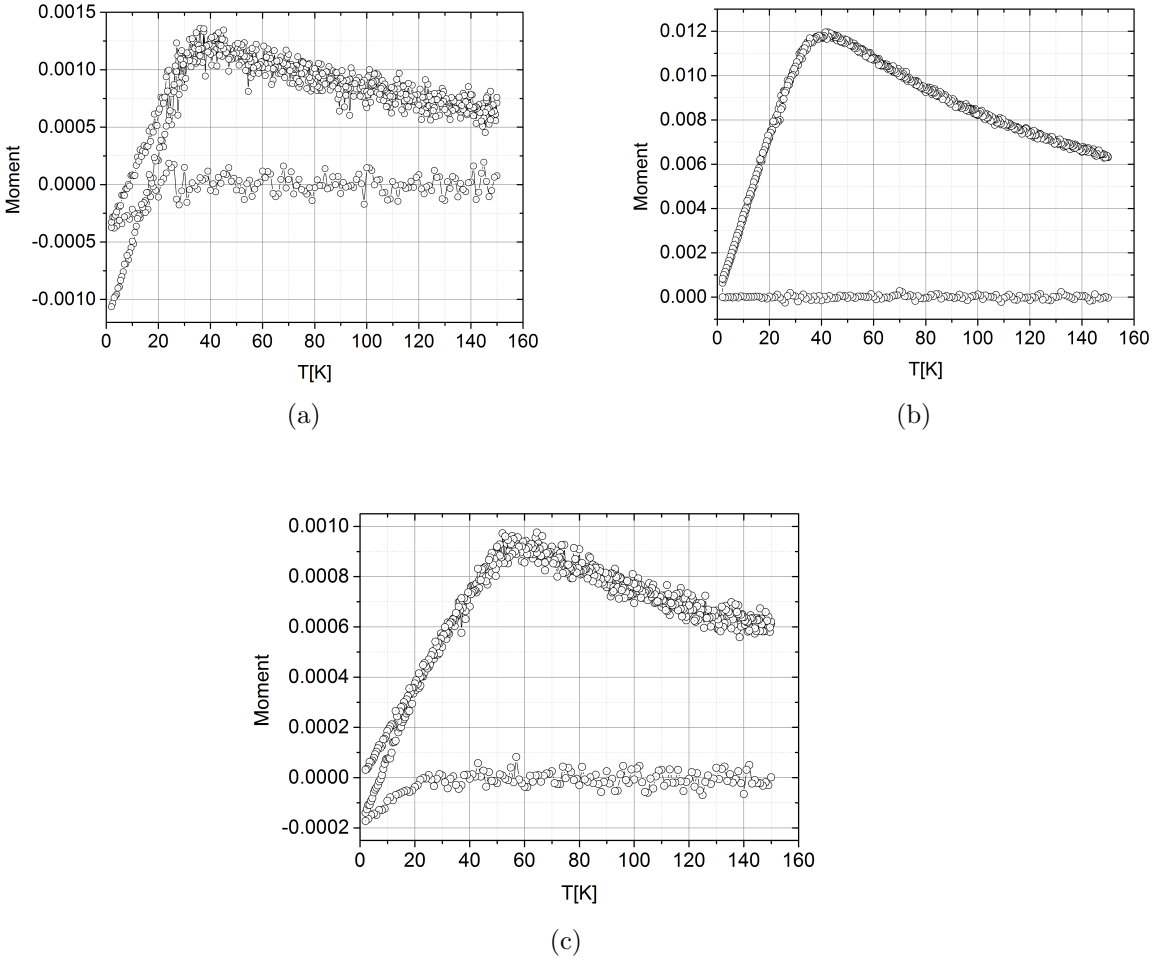

Figure 51: Monte Carlo simulations of the ZFC and FC curves for (a) 10×10×10 MnO nanoparticles at 100 mT, (b) 10×10×10 MnO nanoparticles at 1 T, (c) 20×20×20 MnO nanoparticles at 100 mT in spherical shape.

Bulk MnO are simulated to be compared with the well known experimental results from literatures. Different sizes of MnO nanoparticles are simulated with periodic boundary conditions to make them behave like bulk materials. Figure 52 displays the ZFC and FC magnetizations simulated for bulk MnO using two sizes of MnO nanoparticles with periodic boundary conditions. As can be seen in both figures, peaks at around 70 K can be observed.

For a bulk MnO, the N*éel* temperature at 120 K is expected. This is probably due to the parameters chosen in the Hamiltonian. At the peak temperature, the magnetic moments for both systems reach the same value. The bulk MnO magne-

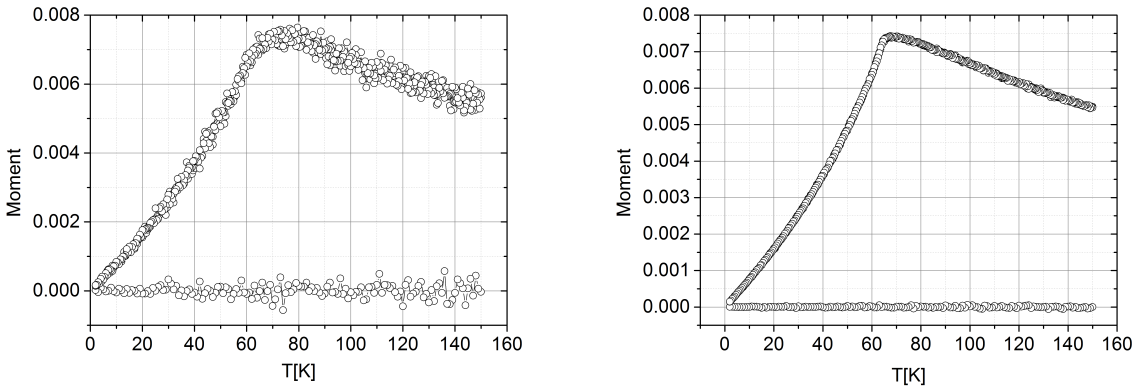

(a) (b)

Figure 52: Monte Carlo simulations of the ZFC and FC curves for (a) 10×10×10, (b) 20×20×20 MnO nanoparticles with periodic boundary conditions at 1 T.

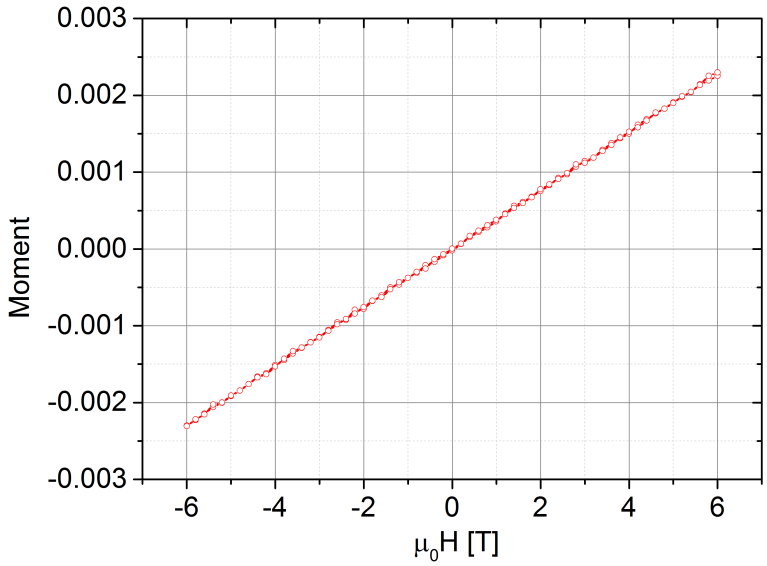

Figure 53: Monte Carlo simulations of the field dependent magnetic moment for 10×10×10 MnO nanoparticles at 5 K with periodic boundary conditions.

tization curves simulated with the 20×20×20 MnO nanoparticle have lower noise than the results with the 10×10×10 MnO nanoparticle.

The peak in the ZFC and FC magnetization curves of the 20×20×20 MnO nanoparticle with periodic boundary conditions exhibits a shape more similar to a bulk material, while a round peak can be seen in figure 52(a). A field dependence of the magnetization is simulated for a 10×10×10 MnO nanoparticle with the peri-

odic boundary conditions. As can be seen in figure 53, a straight line with a positive slope is observed at 5K.

Magnetic field / MnO nanoparticle	100mT	1T	10T	100T
10×10×10 cubic	40 K	40 K	35 K	0
20×20×20 cubic	57 K	57 K	55 K	20 K
10×10×10 spherical	38 K	40 K	-	-
20×20×20 spherical	59 K	-	-	-
10×10×10 bulk	-	71 K	-	-
20×20×20 bulk	-	68 K	-	-

Table 3: List of the peak temperatures for different sizes and shapes of MnO nanoparticles simulated with Monte Carlo methods.

In table 3, the peak temperatures in the ZFC magnetization curves obtained from the Monte Carlo simulations are listed. The peak temperature increases with the increase in the nanoparticle size. The bulk MnO simulated with the 10×10×10 and 20×20×20 MnO nanoparticles have obviously higher peak temperatures compared with the nanoparticles. For both bulk MnO simulated with different sizes of nanoparticles using the boundary conditions, the peak temperatures are almost the same. Until an applied field of 10 T, the peak temperature is almost unchanged. At 100 T, the peak temperature is strongly reduced to 20 K for a 20×20×20 MnO nanoparticle, and no peak can be observed for a 10×10×10 MnO nanoparticle. The MnO nanoparticles with spherical shape show peaks at the same temperatures as the cubic nanoparticles. The surface spins in the MnO nanoparticles do not influence the peak temperature. It can be seen that even with periodic boundary condition, the peak appears at a temperature lower than the MnO N*é*el temperature at 120 K.

According to other preliminary simulations (not shown here), the peak temperature is shifted towards higher temperature as the exchange constants J_1 and J_2 increase. With the choice of the proper constants in the Hamiltonian, the N*é*el temperature of MnO at 120 K should be observed in the ZFC magnetization simulations with periodic boundary conditions.

One should note that the exchange constants used here are taken from experimental results, viz, they are extracted from inelastic neutron scattering data. Consequently, these values do not correspond to real microscopic exchange constants but rather constitute effective macroscopic values being obtained from the neutron scattering data, which is then fitted to a model Hamiltonian. Therefore, a mismatch between experimental and simulational N*é*el temperatures is expected.

6 Summary and Discussion

Using magnetometry, neutron scattering and Monte-Carlo simulations we have elucidated the specific magnetic properties of nanosized MnO. Instead of the N*é*el temperature of MnO at 120 K, a broad peak at low temperature can be observed in the ZFC magnetization curve of MnO nanoparticles in both magnetometry results and the Monte Carlo simulations. However, in the polarized neutron scattering measurements, the expected antiferromagnetic order parameter behavior of MnO is confirmed with the regular N*é*el temperature of ca. 120 K. This seems to contradict to the absence of a peak at T_N in the magnetometry data.

Furthermore, MnO particles show a non-zero memory effect indicating either spin glass behavior of a shell or superspin glass behavior of interacting MnO particles. In addition, an exchange bias effect is observed for MnO nanoparticles without FePt attached. Lastly, TRM and IRM curves have been measured, which show a behavior intermediate between a pure antiferromagnet and a superparamagnet. In the following several potentially possible models for MnO nanoparticles are discussed in order to find the most suitable description.

(a) A Diluted AntiFerromagnet in a Field (DAFF) system is a type of antiferromagnetic domain state model. It has the same universality class like random field ferromagnet [41]. Due to the domain state, the correlation length in the nanoparticles is smaller than the nanoparticle size. The correlation length of 12 nm MnO nanoparticles measured with the neutron scattering at the DNS instrument is 6 - 7 nm at low temperatures. The N*é*el temperature of MnO would be reduced in a DAFF system. This could explain the peaks at low temperatures in the ZFC magnetization curves of MnO nanoparticles. However, the N*é*el temperature of MnO at 120 K is observed in the neutron scattering. This is in conflict with the expected critical temperature reduced by the random fields. However, the TRM and IRM measurements of MnO nanoparticles show similar behavior with a DAFF system.

(b) Another antiferromagnetic domain state model is due to the degeneracy of multiple domains. The magnetic moments of MnO are in perfect ferromagnetic ordering within a single [111] plane, and the neighbouring [111] planes are in antiferromagnetic ordering. This perfect order is surprising considering the highly frustrated configuration of the nearest and next-nearest neighbour interactions (see figure 25). From such a configuration one would rather expect a glassy frustrated behavior. We assume that the antiferromagnetic order in MnO is a highly unstable state subject to frustration-induced fluctuations and reconfigurations.

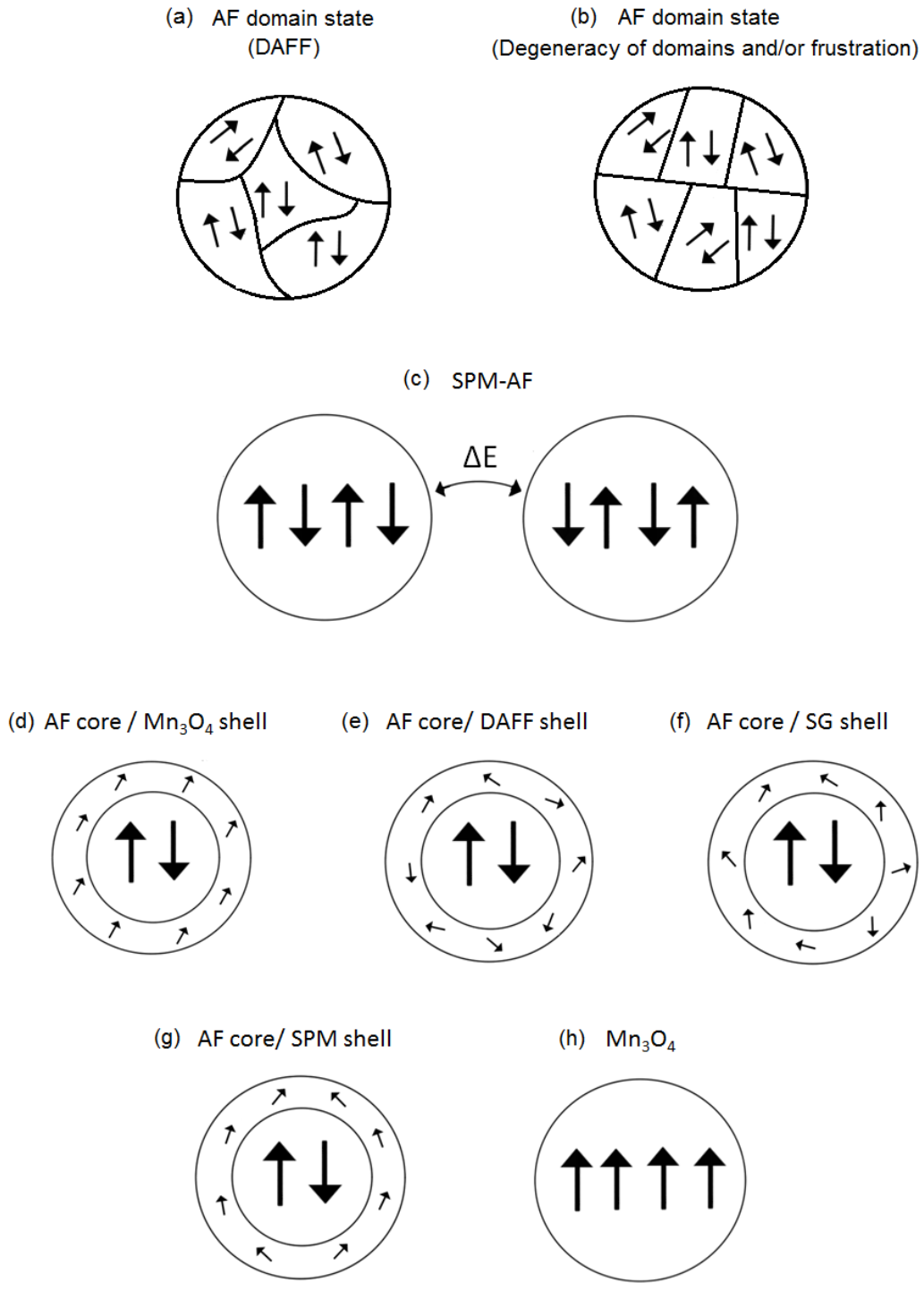

Figure 54: Different models for MnO nanoparticle.

Such a system would display many degenerate coexisting domains and continuous reconfigurations of this state. This can explain the missing feature at the Néel temperature of MnO measured by the magnetometry. Due to the domains, the magnetic moments are in short-range ordering. The correlation length is reduced compared to the nanoparticle size, which could explain the neutron data. The magnetic domain walls may behave like a superparamagnet or a spin glass. This could explain the peaks measured at low temperatures in the ZFC curves and the splitting between the ZFC and FC curves. For spin-glass-like domain walls, a magnetic memory effect might be expected.

(c) A Superpara-Antiferromagnet is a type of antiferromagnetic system. The magnetic moments in the nanoparticles can flip correlated. They stay in antiferromagnetic ordering during flipping. Above the Néel temperature of MnO at 120 K, the magnetic moments are randomly ordered due to the thermal fluctuation. Between the ZFC peak temperature at ca. 20 K and the Néel temperature at 120 K, the magnetic moments are in antiferromagnetic ordering but flipping statistically.

The antiferromagnetic ordering can be measured in the neutron scattering, which has a measurement time in the order of nanoseconds. However, the magnetometer has a typical measurement time of a few seconds. This would explain why in magnetometry such a system shows superparamagnetic (unblocked) behavior.

Below the ZFC peak temperature, the magnetic moments are blocked in antiferromagnetic state. The antiferromagnetic ordering at these temperatures can be measured both in the magnetometry and the neutron scattering. The field dependence of the peak temperature measured in the ZFC magnetization curves would also be stable. This phenomenon is usually observed in an antiferromagnetic system. The peak temperature for a superpara-antiferromagnetic system is expected to increase as the particles size increases. This is opposite to the magnetometry result of the MnO nanoparticles. In a superpara-antiferromagnetic system, the exchange bias and the memory effect cannot be measured. Hence, this contradicts the experimental results.

(d) The surface of the MnO nanoparticles might be oxidized to a ferrimagnetic Mn_2O_3 or Mn_3O_4 shell. Due to the oxidation, the size of the antiferromagnetic core is reduced. This agrees to the correlation length of the MnO nanoparticles measured by the DNS instrument, which is smaller than the nanoparticle size. During zero field cooling, the magnetic moments in a superparamagnet are randomly frozen at low temperature. As the temperature increases in the presence of a magnetic field, the magnetic moments trend to align along the magnetic field. At the same time,

the thermal fluctuations start to destroy the magnetic order. As a result, the magnetization reaches a maximum at a critical temperature in the ZFC curve. With an applied field, the magnetic moments can be ordered during the cooling procedure and frozen in the ordered states at low temperature.

The splitting between the ZFC and FC can be explained by freezing of the magnetic moments in a superparamagnetic shell. The peak at low temperature is possible to be measured due to the Mn_3O_4 shell. For a superparamagnet, the blocking temperature should have obvious decrease with an increase of the magnetic field. This is in conflict with the magnetometry results of the MnO nanoparticles.

Moreover, the antiferromagnetic MnO core should exhibit some feature at the N*é*el temperature, which is not observed in the ZFC magnetization curves.

(e) The MnO nanoparticles can be described by an antiferromagnetic core with a DAFF shell [42]. As been discussed in model (a), the peaks appearing in the ZFC magnetization curves can be explained by the DAFF shell. The correlation length is reduced due to the DAFF shell. However, the antiferromagnetic MnO core should show some feature at the N*é*el temperature 120 K. This cannot be seen in the magnetometry results of MnO nanoparticles.

(f) The antiferromagnetic MnO core is possibly covered by a spin glass shell. The peaks at low temperatures in the ZFC magnetization curves can be caused by the spin glass shell. The memory effect is observed in the MnO nanoparticles, which matches the results of a spin glass. The reduced correlation length measured by the polarized neutron scattering can also be explained by such a core-shell system. However, the smooth curve in the ZFC magnetization near the N*é*el temperature as well as the field dependence of the peak temperature are in conflict with this model.

(g) Similar to the core-shell systems discussed above, the antiferromagnetic MnO core can be covered by a superparamagnetic shell with other manganese oxides or canted antiferromagnetic spins. The superparamagnetic shell can cause a peak at the blocking temperature. The field dependence of the peak temperature for a superparamagnetic system should have a strong decrease as the magnet field increases. The feature at the MnO N*é*el temperature in the ZFC magnetization curves is missing. The magnetic memory effect and exchange bias effect cannot be measured in this model.

(h) The MnO nanoparticle could be almost completely oxidized to ferrimagnetic Mn_2O_3 or Mn_3O_4. Mn_2O_3 or Mn_3O_4 shows superparamagnetic behavior in nanoparticle size. The N*é*el temperature of residual MnO is reduced to low temperature due

to the finite size. However, the field dependence of the peak temperature measured by the MnO nanoparticles is in conflict with this model. In the polarized neutron scattering at the DNS instrument, the N*é*el temperature of MnO at 120 K is observed. This cannot be measured in complete Mn_3O_4 nanoparticles. The magnetic memory effect and exchange bias effect are not expected in such a system as well.

Besides the single particle models, the MnO nanoparticles with a superspin could show features of a collective system. As can be seen in the TEM images in section 3, the nanoparticles are close packed. The distance between the nanoparticles are small, so they might interact with each other. A non-interacting superparamagnetic system is thus excluded. The superspins of the MnO nanoparticles could form a superspin glass system. The magnetic memory effect measured in the MnO nanoparticles could be explained.

In summary, the magnetic order parameter measured by the polarized neutron scattering at the DNS instrument shows the N*é*el temperature of MnO at ca. 120 K. This result confirms the existence of the antiferromagnetic ordered MnO. The model (h) of a complete ferrimagnetic Mn_2O_3 or Mn_3O_4 with a critical temperature of ca. 40 K is therefore less possible. The order parameter measured at 120 K are in conflict with the expected results of AF domain state models (a). The order parameter found in model (b) can be explained by the antiferromagnetically ordered MnO domains in the nanoparticles. The antiferromagnetically ordered MnO can exist in the form of domains, superpara-antiferromagnetic system, or antiferromagnetic cores.

In a superpara-antiferromagnetic model, the N*é*el temperature of MnO is possible to be observed at 120 K in the polarized neutron scattering and at low temperature in the magnetometry. The size dependence of the peak temperature is opposite to the expected results, which cannot be explained so far.

The ferrimagnetic Mn_3O_4 shell model or a other type of shell model is probably strongly coupled to the antiferromagnetic MnO core. The core and shell are so strongly coupled that only one peak in the ZFC curves can be observed. This could explain the behavior of the peak temperature dependence on the magnetic field. In the case of a relatively small antiferromagnetic MnO core, the feature at the N*é*el temperature of MnO would not occur in this model, because of the strong coupling to the shell so that only a coupled or joint feature "core + shell" is found in the ZFC curve.

However, in the Small Angle Neutron Scattering (SANS) measurements per-

formed by Alice Klapper, no shell in the MnO nanoparticles can be detected. The resolution of the instrument might not be good enough to observe the shell. Or the shell is strongly coupled to the core, so that it cannot be detected. The exchange bias effect measured in MnO nanoparticles can be explained by a AF-FM core shell system, or a AF domain state with ferromagnetic domain walls. The magnetic memory effect is observed in MnO nanoparticles. This is possible to be measured in a spin glass shell, spin-glass-like domain walls or a collective superspin glass system formed by the superspins of MnO nanoparticles. Neither of the above discussed model can completely describe the present results. Summarizing this discussion, one comes to the conclusion that no model can perfectly explain *all* experimental findings. It seems to us, that from all potential models the partially oxidized MnO-core/Mn_2O_3 or Mn_3O_4 -shell model suites best, because shell-oxidation in MnO particles was found before in other studies [36]. Definitely, further measurements are necessary to shed light onto this question. The model of an antiferromagnetic MnO core with a strongly coupled shell and the superpara-antiferromagnetic model are favored according to the existing results.

The novel type of FePt@MnO heterodimer nanoparticles are measured with magnetometry and the polarized neutron scattering. The magnetic moments in the FePt nanoparticles are pinned to the magnetic moments on the surface of the MnO nanoparticles due to the exchange bias effect. The magnetometry measurements of the FePt@MnO nanoparticles show similar results to single MnO nanoparticles. The peak temperatures in the ZFC magnetization curves are slightly higher compared to single MnO nanoparticles due to exchange bias. The memory effect is measured in various sizes of the FePt@MnO nanoparticles. The TRM and IRM magnetization curves exhibit the behavior of a system between an antiferromagnet and a superparamagnet. Compared to the neutron scattering data of single MnO nanoparticles, the antiferromagnetic order parameter of MnO is not significantly influenced by the FePt subunits inside the FePt@MnO nanoparticles. About a microscopic influence at the interface, no conclusion can be drawn from this data and should be investigated in future.

7 Outlook

According to the present results, the MnO nanoparticles cannot be fully described by the models discussed in section 6. More measuring methods such as susceptibility measurements can be employed to study the MnO nanoparticles. The visualization of the spin structures of the MnO nanoparticles in the Monte Carlo simulations is necessary due to the abnormal magnetic properties of the MnO nanoparticles measured in the magnetometry. This will possibly help to understand the macroscopic magnetic behavior.

In the Monte Carlo simulation of a bulk MnO, the Néel temperature at 120 K is not achieved in this work. The proper parameters in the Hamiltonian of the MnO have to be investigated in the future work, so that the peak temperatures in the ZFC magnetization curves can be better compared with the simulations. In order to compare with the experimental results, the Monte Carlo simulations of the FePt@MnO heterodimer nanoparticles are interesting. The spin structure inside the FePt nanoparticles and the influence of the FePt nanoparticles onto the spin structure in the MnO nanoparticles should be visualized with the simulation results.

Magnetic nanoparticles have attractive advantages in spintronic devices. The heterodimer nanoparticles composed of a ferromagnetic nanoparticle exchange biased by an antiferromagnetic nanoparticle could have potential use in GMR-spin-valve devices as sketched in figure 55. Using the nanoparticles, the GMR-spin-valve devices with an decreased volume can be achieved. It is also insteresting to study other exchange biased AF-FM heterodimer nanoparticles.

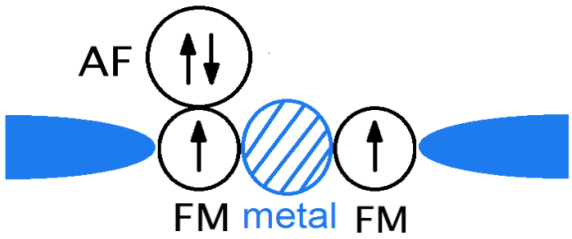

Figure 55: Schematical illustration of a nanoparticle GMR-spin-valve device.

8 References

[1] C. G. Shull, W. A. Strauser, and E. O. Wollan, "Neutron Diffraction by Paramagnetic and Antiferromagnetic Substances," vol. 1572, p. 1949, 1951.

[2] T. Chatterji, Y. Su, G. N. Iles, Y. Lee, A. P. Khandhar, and K. M. Krishnan, "Antiferromagnetic spin correlations in MnO nanoparticles," *Journal of Magnetism and Magnetic Materials*, vol. 322, p. 3333, 2010.

[3] M. Feygenson, W. Schweika, A. Ioffe, S. B. Vakhrushev, and T. Brückel, "Magnetic phase transition in confined MnO nanoparticles studied by polarized neutron scattering," *Physical Review B*, vol. 81, p. 1, 2010.

[4] C. Wang, S. Baker, M. Lumsden, S. Nagler, W. Heller, G. Baker, P. Deen, L. Cranswick, Y. Su, and A. Christianson, "Antiferromagnetic order in MnO spherical nanoparticles," *Physical Review B*, vol. 83, p. 1, 2011.

[5] A. Klapper, "Einfluss äusserer Felder auf das Wachstum von Mesokristallen aus FePt@MnO-Nanodimeren. Diplomarbeit, RWTH Aachen University," January, 2012.

[6] C. Schulze and T. U. Chemnitz, "Magnetic recording on nanostructures," 2011.

[7] S. Blundell, "Magnetism in Condensed Matter," *Oxford University Press, Oxford*, 2001.

[8] S. Blügel, C. M. Schneider, and T. Brückel, "Magnetism goes Nano," *Lecture Manuscripts of the 36th Spring School of the Institute of Solid State Research, Forschungszentrum Jülich.*, 2005.

[9] F. Wiekhorst, E. Shevchenko, H. Weller, and J. Kötzler, "Anisotropic superparamagnetism of monodispersive cobalt-platinum nanocrystals.," *Physical Review B*, vol. 67, p. 224416, 2003.

[10] S. Mørup, M. F. Hansen, and C. Frandsen, "Magnetic interactions between nanoparticles.," *Beilstein journal of nanotechnology*, vol. 1, p. 182, 2010.

[11] S. Bedanta, "Supermagnetism in magnetic nanoparticle systems," *Dissertation, University Duisburg-Essen*, 2006.

[12] O. Petracic, "Superparamagnetic nanoparticle ensembles," *Superlattices and Microstructures*, vol. 47, p. 569, 2010.

[13] A. Ebbing, L. Agudo, G. Eggeler, and O. Petracic, "Tuning the magnetic properties of Co particles by Pt capping," *Phys. Rev. B.*, vol. 84, p. 012405, 2011.

[14] J. A. Mydosh, *Spin Glasses: An experimental introduction.* CRC Press, 1993.

[15] L. N*é*el *C. R. Acad. Sci., Paris*, vol. 252, p. 4075, 1961.

[16] M. A. Morales, R. Skomski, S. Fritz, G. Shelburne, J. E. Shield, M. Yin, S. O'Brien, and D. L. Leslie-Pelecky *Physical Review B*, vol. 75, p. 134423, 2007.

[17] J. Nogués and I. K. Schuller, "Exchange bias," *Journal of Magnetism and Magnetic Materials*, vol. 192, p. 203, 1999.

[18] W. H. Meiklejohn and C. P. Bean, "New magnetic anisotropy," *Phys. Rev.*, vol. 105, p. 904, 1957.

[19] M. Kiwi, "Exchange bias theory," *Journal of Magnetism and Magnetic Materials*, vol. 234, p. 584, 2001.

[20] J. Binney, N. Dowrick, A. Fisher, and M. Newman, "The theory of critical phenomena, Oxford University Press, Oxford," 1992.

[21] D. S. Greving, "Structural Investigations on Systems of Self-Organized Nanoparticles.," *Master thesis, Ruhr University Bochum*, 2013.

[22] K. Trohidou and M. Vasilakaki, "Monte Carlo Studies of Magnetic Nanoparticles," *Applications of Monte Carlo Method in Science and Engineering, Prof. Shaul Mordechai (Ed.), ISBN: 978-953-307-691-1, InTech,Available from:http://www.intechopen.com/books/applications-of-monte-carlo-method-in-science-andengineering/monte-carlo-studies-of-magnetic-nanoparticles*, 2011.

[23] T. D. Schladt, T. Graf, O. Köhler, H. Bauer, M. Dietzsch, J. Mertins, R. Branscheid, and W. Kolb, U.and Tremel, "Synthesis and Magnetic Properties of FePt@MnO Nano-heteroparticles," *Chemistry of Materials*, vol. 24, p. 525, 2012.

[24] T. D. Schladt, K. Schneider, M. I. Shukoor, F. Natalio, H. Bauer, M. N. Tahir, S. Weber, L. M. Schreiber, H. C. Schröder, W. E. G. Müller, and W. Tremel, "Highly soluble multifunctional MnO nanoparticles for simultaneous optical and MRI imaging and cancer treatment using photodynamic therapy," *Journal of Materials Chemistry*, vol. 20, p. 8297, 2010.

[25] Quantum Design, "Magnetic Property Measurement System MPMS XL Reference Manual," 2005.

[26] Quantum Design, "Physical Property Measurement System PPMS User's Manual," 2004.

[27] The Heinz Maier-Leibnitz Zentrum, "http://www.mlz-garching.de/dns," 2013.

[28] R. Schedler, U. Witte, M. Loewenhaupt, and J. Kulda, "Coupling between crystal field transitions and phonons in the 4f-electron system $CeCu_2$," *Physica B: Condensed Matter*, vol. 335, p. 41, 2003.

[29] Institut Laue Langevin, "D7 Diffuse Scattering Spectrometer," *http://www.ill.eu/*, 2013.

[30] J. R. Stewart, P. P. Deen, K. H. Andersen, H. Schober, J.-F. Barthélémy, J. M. Hillier, A. P. Murani, T. Hayes, and B. Lindenau, "Disordered materials studied using neutron polarization analysis on the multi-detector spectrometer, D7," *Journal of Applied Crystallography*, vol. 42, p. 69, 2008.

[31] T. M. Harders, T. J. Hicks, and P. Wells, "Multiple scattering in neutron polarization analysis experiments," *Journal of Applied Crystallography*, vol. 18, p. 131, 1985.

[32] P. Wells and R. Cywinski, "Multiple Scattering in neutron polarization analysis," *Australian Journal of Physics*, vol. 34, p. 193, 1981.

[33] J. Mayers and R. Cywinski, "A Monte-Carlo evaluation of analytical multiple scattering corrections for unpolarised neutron scattering and polarisation analysis data," *Nuclear Instruments and Methods in Physics Research Section A*, vol. 241, p. 519, 1985.

[34] O. Schärpf and H. Capellmann, "Structural and magnetic investigations of a La_2CuO_4 single crystal with polarization analysis," *Zeitschrift für Physik B-Condensed Matter*, vol. 80, p. 253, 1990.

[35] M. E. Lines and E. D. Jones, "Antiferromagnetism in the face-centered cubic lattice. II. Magnetic properties of MnO," *Phys. Rev*, vol. 139, p. 1313, 1965.

[36] A. Berkowitz, G. Rodriguez, J. Hong, K. An, T. Hyeon, N. Agarwal, D. Smith, and E. Fullerton, "Antiferromagnetic MnO nanoparticles with ferrimagnetic Mn_3O_4 shells: Doubly inverted core-shell system," *Physical Review B*, vol. 77, p. 1, 2008.

[37] S. Mukherjee, A. K. Pal, S. Bhattacharya, and J. Raittila, "Magnetism of Mn_2O_3 nanocrystals dispersed in a silica matrix: Size effects and phase transformations," *Physical Review B*, vol. 74, p. 104413, 2006.

[38] O. Petracic, X. Chen, S. Bedanta, W. Kleemann, S. Sahoo, S. Cardoso, and P. Freitas, "Collective states of interacting ferromagnetic nanoparticles," *Journal of Magnetism and Magnetic Materials*, vol. 300, p. 192, May 2006.

[39] M. Benitez, O. Petracic, H. Tüysüz, F. Schüth, and H. Zabel, "Fingerprinting the magnetic behavior of antiferromagnetic nanostructures using remanent magnetization curves," *Physical Review B*, vol. 83, p. 1, 2011.

[40] A. L. Patterson, "The scherrer formula for x-ray particle size determination," *Physical Review B*, vol. 56, p. 978, 1939.

[41] S. Fishman and A. Aharony, "Random field effects in disordered anisotropic antiferromagnets," *Journal of Physics C: Solid State Physics*, vol. 12, p. L729, 1979.

[42] M. Benitez, O. Petracic, E. Salabas, F. Radu, H. Tüysüz, F. Schüth, and H. Zabel, "Evidence for Core-Shell Magnetic Behavior in Antiferromagnetic Co_3O_4 Nanowires," *Physical Review Letters*, vol. 101, p. 50, 2008.